

UNCLASSIFIED

AD NUMBER
AD869250
NEW LIMITATION CHANGE
TO Approved for public release, distribution unlimited
FROM Distribution: Further dissemination only as directed by Space and Missile Systems Organization, Norton, AFB, CA, DEC 1969, or higher DoD authority.
AUTHORITY
SAMSO ltr, 5 Dec 1975

THIS PAGE IS UNCLASSIFIED

THIS REPORT HAS BEEN DELIMITED
AND CLEARED FOR PUBLIC RELEASE
UNDER DOD DIRECTIVE 5200.20 AND
NO RESTRICTIONS ARE IMPOSED UPON
ITS USE AND DISCLOSURE.

DISTRIBUTION STATEMENT A

APPROVED FOR PUBLIC RELEASE;
DISTRIBUTION UNLIMITED.

V

AD869250

ATHENA H
AERODYNAMIC DATA SUMMARY

01-EN-004

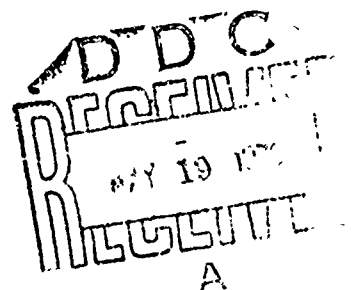
V. J. Balpsys

STATEMENT #01-EN-004

This document may be further distributed by any holder only with
specific prior approval of Prepared For

Headquarters
Space and Missile Systems Organization
Air Force Systems Command
Norton Air Force Base, California

attn: smyBA

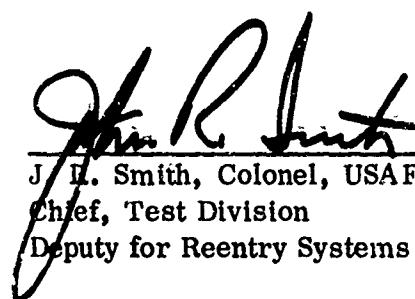


NOTICE

When Government drawings, specifications, or other data are used for any purpose other than in connection with a definitely related Government procurement operation, the United States Government thereby incurs no responsibility nor any obligation whatsoever; and the fact that the Government may have formulated, furnished, or in any way supplied the said drawings, specifications, or other data, is not to be regarded by implication or otherwise as in any manner licensing the holder or any other person or corporation or conveying any rights or permission to manufacture, use, or sell any patented invention that may in any way be related thereto.

ATHENA H AERODYNAMIC DATA SUMMARY

V. J. Baipsys


J. R. Smith, Colonel, USAF
Chief, Test Division
Deputy for Reentry Systems

FOREWORD

This report was prepared for the United States Air Force by Atlantic Research Corporation, A Division of The Susquehanna Corporation, 3333 Harbor Boulevard, Costa Mesa, California, in partial fulfillment of Contract F04701-68-C-0046, CDRL Sequence No. 21, for ATHENA/627A.

The program was performed by the Missile Systems Division of Atlantic Research, under the direction of the Space and Missile Systems Organization, Norton Air Force Base, California. The program monitor was Colonel J. R. Smith.

The work reported in this document represents the efforts of V. J. Baipsys, R. L. Benton, R. J. Hauser, J. W. McClymonds and G. M. Petak who are members of the Systems Engineering Group of the Missile Systems Division of Atlantic Research.

The number assigned to this document by Atlantic Research Corporation is 01-EN-004

This report was submitted by the author in December 1969. The report represents work conducted between December 1967 and August 1969.

This technical report has been reviewed and is approved.

J. R. Smith, Colonel, USAF
Chief, Test Division
Deputy for Reentry Systems

ABSTRACT

This document presents aerodynamic characteristics for the ATHENA H reentry research vehicle. Data presented herein include longitudinal, lateral and directional stability characteristics and normal, side, and axial force characteristics as a function of Mach number, for the complete vehicle and expended stages. Also presented herein are aerodynamic loads on the vehicle appendage and external pressures on the major and minor vehicle components. This information is presented in tabular and graphical form throughout the range of vehicle flight attitude and trajectories to be experienced by ATHENA H.

TABLE OF CONTENTS

<u>Section</u>		<u>Page</u>
	LIST OF ABBREVIATIONS AND SYMBOLS	viii
I	INTRODUCTION	1-1
II	VEHICLE DESCRIPTION	2-1
III	TOTAL VEHICLE AERODYNAMIC CHARACTERISTICS	3-1
	3.1 General	3-1
	3.2 Boost Phase Aerodynamic Data	3-1
	3.2.1 Longitudinal Stability Characteristics	3-1
	3.2.2 Lateral Stability Characteristics	3-2
	3.2.3 Directional Stability Characteristics	3-2
	3.2.4 Static Stability Margin Requirements	3-2
	3.2.5 Axial Force Characteristics	3-2
	3.2.6 Spin Profiles	3-3
	3.2.7 Velocity Package Aerodynamic Data	3-4
	3.3 Reentry Aerodynamics	3-4
	3.4 Non-Linear Longitudinal Stability Characteristics	3-4
IV	AERODYNAMIC LOAD DISTRIBUTIONS	4-1
	4.1 General	4-1
	4.2 Component Normal Force Slope and Center of Pressure	4-1
	4.3 Appendage Aerodynamic Loads.	4-1
V	EXTERNAL PRESSURE DISTRIBUTION	5-1
	5.1 General	5-1
	5.2 Vehicle Pressure Distribution	5-1
	5.3 Component Pressure Distribution	5-2
	5.3.1 Raceway	5-2
	5.3.2 Recruit Nose	5-2
	5.3.3 Aft Recruit Fairing	5-2
	5.3.4 Shroud and Pylons	5-3

TABLE OF CONTENTS (CONTINUED)

<u>Section</u>		<u>Page</u>
	5.3.5 Booster Shroud Aft Seal	5-3
	5.3.6 Minimum Pressure on Booster Shroud Structure	5-4
	5.3.7 Fin	5-4
VI	CONCLUSIONS	6-1
VII	REFERENCES	7-1

LIST OF ILLUSTRATIONS

<u>Figure</u>		<u>Page</u>
2-1	ATHENA H Profile	2-2
2-2	ATHENA H Fin Geometry	2-3
2-3	ATHENA H Roll Tab Geometry	2-4
3-1	Normal Force Coefficient Slope	3-7
3-2	Pitching Moment Coefficient Slope	3-8
3-3	Normal Force Due to Pitching Rate	3-9
3-4	Pitch Damping Coefficient	3-10
3-5	Fin Effectiveness in Roll	3-11
3-6	Damping in Roll Derivative	3-12
3-7	Roll Tab Effectiveness in Roll	3-13
3-8	Vehicle Stability versus Mach Numbers	3-14
3-9	Zero Lift Drag Coefficient.	3-15
3-10	Zero Lift Drag Coefficient ("Specification" Drag)	3-16
3-11	Zero Lift Drag Coefficient ("Best Estimate" Drag)	3-17
3-12	Spin Profile, 3-Stage Vehicle (Algol II-B).	3-18
3-13	Spin Profile, 3-Stage Vehicle (Castor IV).	3-19
3-14	Velocity Package Drag	3-20
3-15	Booster Reentry Axial Force Characteristics	3-21
3-16	Upper Stage Reentry Drag Characterisitics	3-22
3-17	Velocity Package Reentry Drag Characteristics	3-23
3-18	Interstage Adapter Reentry Drag Characterisitics	3-24
3-19	Heat Shield Half Reentry Drag Characteristics	3-25
3-20	Heat Shield Half Reentry Drag Characteristics, $\alpha = 0^\circ$	3-26
3-21	Yo-Yo Weights Reentry Drag Characteristics	3-27
3-22	Component Reentry Drag Characteristics	3-28
3-23	Booster Reentry Normal Force Coefficient Slope	3-29
3-24	Booster Reentry Pitching Moment Coefficient Slope	3-30
3-25	Normal Force Parameter versus Mach Number, Non-Linear Aerodynamic Inputs to ASO-5D	3-31
3-26	Center of Pressure versus Mach Number, Non-Linear Aerodynamic Inputs to ASO-5D	3-32
4-1	Component Normal Force Coefficient Slope	4-4
4-2	Fin Normal Force Coefficient Slope	4-5
4-3	Component Center of Pressure Location in Station Numbers	4-6
4-4	Fin Center of Pressure Location in Station Numbers	4-7
4-5	Fin Spanwise Load Distribution	4-8

LIST OF ILLUSTRATIONS (Continued)

<u>Figure</u>		<u>Page</u>
4-6	Axial Force Per Unit Dynamic Pressure, One Fin Without Tab	4-9
4-7	Axial and Normal Force on Each Tab Based on PWT Test	4-10
4-8	Fin Chord-Wise Loading	4-11
4-9	Ratio of Span-Wise to Root Loading on Vehicle Fin	4-12
5-1	External Pressure Coefficient Distribution, $M_{\infty} = 0.169 \alpha = 0$	5-5
5-2	External Pressure Coefficient Distribution, $M_{\infty} = 0.79 \alpha = 0$	5-6
5-3	External Pressure Coefficient Distribution, $M_{\infty} = 0.89 \alpha = 0$	5-7
5-4	External Pressure Coefficient Distribution, $M_{\infty} = 1.0 \alpha = 0$	5-8
5-5	External Pressure Coefficient Distribution, $M_{\infty} = 1.083 \alpha = 0$	5-9
5-6	External Pressure Coefficient Distribution, $M_{\infty} = 1.57 \alpha = 0$	5-10
5-7	External Pressure Coefficient Distribution, $M_{\infty} = 1.39 \alpha = 0$	5-11
5-8	External Pressure Coefficient Distribution, $M_{\infty} = 1.6 \alpha = 0$	5-12
5-9	External Pressure Coefficient Distribution, $M_{\infty} = 1.79 \alpha = 0$	5-13
5-10	External Pressure Coefficient Distribution, $M_{\infty} = 2.0 \alpha = 0$	5-14
5-11	External Pressure Coefficient Distribution, $M_{\infty} = 3.0 \alpha = 0$	5-15
5-12	External Pressure Coefficient Distribution, $M_{\infty} = 3.465 \alpha = 0$	5-16
5-13	External Pressure Coefficient Distribution, $M_{\infty} = 4.0 \alpha = 0$	5-17
5-14	External Pressure Coefficient Distribution, $M_{\infty} = 6.0 \alpha = 0$	5-18
5-15	External Pressure on Raceway Nose, Castor IV Low ϕ Trajectory	5-19
5-16	External Pressure on Raceway Mid-Section, Castor IV	5-20
5-17	External Pressure on Last Six Inches of Raceway in Separated Region Ahead of 2nd Stage Shroud, Castor IV, Low Trajectory	5-21
5-18	External Pressure on Recruit Nose, Castor IV	5-22
5-19	External Pressure on Recruit Fairing Circular Segment, Castor IV	5-23
5-20	External Pressure on Aft Fairing Excluding Circular Segment, Castor IV	5-24
5-21	External Pressure on Payloads and 1st Stage Shroud, Castor IV	5-25
5-22	External Pressure on 1st Stage Shroud, Castor IV	5-26
5-23	Plume Boundary - Free Stream Interaction Pressure as a Function of Initial Turning Angle, Castor IV	5-27
5-24	External Pressure on Payloads, Aft Recruit Fairing and Shroud	5-28

LIST OF ILLUSTRATIONS (Continued)

<u>Figure</u>		<u>Page</u>
5-25	Fin Leading Edge External Pressure, Castor IV	5-29
5-26	Fin Side Panel External Pressure, Auxiliary Payload Pod on, Castor IV	5-30
5-27	Fin Side Panel External Pressure, Launch Lugs on, Castor IV . .	5-31

LIST OF TABLES

<u>Table</u>		<u>Page</u>
3-1	ATHENA H Zero-Lift Drag Increment	3-6
3-2	ATHENA H Velocity Package Aero Data	3-6
4-1	Appendages and Component Lift and Drag Characteristics	4-3
5-1	Castor IV Trajectories	5-32

LIST OF ABBREVIATIONS AND SYMBOLS

AR	Aspect Ratio, $\frac{b^2}{S}$
b	Effective Span Length, 5.555 Feet
C_A	Axial Force Coefficient, $\frac{F_A}{qS}$
C_D	Drag Force Coefficient, $\frac{F_D}{qS}$ (equal to C_A at $\alpha = 0^\circ$)
C_l	Roll Moment Coefficient, $\frac{L}{qSd}$
C_{l_p}	Roll Damping Coefficient, $\frac{\partial C_l}{\partial \left(\frac{\dot{\phi} d}{2V} \right)}$, Per Radian
C_{l_δ}	Roll Forcing Coefficient, $\frac{\partial C_l}{\partial \delta}$, Per Degree
C_m	Pitch Moment Coefficient, $\frac{M}{qSd}$
C_{m_α}	Pitch Moment Coefficient Slope, $\frac{dC_m}{d\alpha}$, Per Degree
C_{m_q}	Pitch Damping Coefficient, $\frac{\partial C_m}{\partial \left(\frac{\dot{\theta} d}{2V} \right)}$, Per Radian
C_n	Yaw Moment Coefficient, $\frac{N}{qSd}$

$C_{\dot{n}\beta}$ Yaw Moment Coefficient Slope, $\frac{dC_n}{d\beta}$, Per Degree

C_N Normal Force Coefficient, $\frac{F_N}{qS}$

$C_{N\alpha}$ Normal Force Coefficient Slope, $\frac{dC_N}{d\alpha}$, Per Degree

$C_{N\dot{q}}$ Normal Force Due to Pitch Rate, $\frac{\partial C_N}{\partial \left(\frac{\dot{\theta} d}{2V} \right)}$, Per Radian

C_{n_r} Yaw Damping Coefficient, $\frac{\partial C_n}{\partial \left(\frac{\dot{\psi} d}{2V} \right)}$, Per Radian

C_Y Yaw Force Coefficient, $\frac{Y}{qS}$

$C_{Y\beta}$ Yaw Force Coefficient Slope, $\frac{dC_Y}{d\beta}$, Per Degree

C_{Y_r} Yaw Force Due to Yaw Rate, $\frac{\partial C_Y}{\partial \left(\frac{\dot{\psi} d}{2V} \right)}$

cg Center of Gravity Location, Station Number

C.P. Center of Pressure Location, Station Number

C_p Pressure Coefficient, $\frac{P_e - P_\infty}{q_\infty}$

d Reference Diameter, 3.33 Feet

F_A Axial Force, Pounds

L Roll Moment, Foot-Pounds

N Yaw Moment, Foot-Pounds

M Pitch Moment, Foot-Pounds

P Pressure, Pounds per Square Inch

ΔP	Pressure Difference, Pounds per Square Foot
q	Dynamic Pressure, Pounds per Square Foot
S	Effective Fin Panel Area, Square Feet
S_R	Reference Area, 8.727 Square Feet
ω_n	Natural Pitching Frequency, Cycles Per Second
α	Angle of Attack, Degrees
β	Angle of Yaw, Degrees
γ	Ratio of Specific Heats, 1.4 for Air
λ	Fin Panel Taper Ratio
δ	Fin Incidence Angle, Degrees
Λ	Fin Sweep Angle, Degrees
ϕ	Roll Angle, Degrees
θ	Pitch Angle, Degrees
ψ	Yaw Angle, Degrees

Subscripts

R	Reference
∞	Free Stream
e	External Conditions

Note: A dot above a symbol denotes differentiation with respect to time.

I

INTRODUCTION

This document is a compilation of the ATHENA II aerodynamic data which were used for flight simulation and structural design. The data presented herein describe total vehicle aerodynamic characteristics, component aerodynamic loads, and external pressure distributions.

Total vehicle data are presented in tabular and graphical form for the Mach number range from zero to ten within the linear angle of attack region. Reentry drag force data for the expended stages are presented as average drag forces for the individual stages. These vehicle data as well as booster reentry data apply to both the Algol II-B and Castor IV flight configurations since they are identical aerodynamically. External pressures are presented for all compartments which will be vented during flight. These pressures are presented for the Castor IV (TD 115 Motor data) trajectories since they are slightly more severe than the pressures for the Algol II-B trajectories. Subsequent analyses based upon trajectories using TD 123 motor data showed slightly differing external pressure histories. However, as explained in Section V, these differing external pressures had no significant effect upon the ATHENA H venting analysis. Since the venting analysis is the only analysis affected by the external pressure histories, the external pressures presented herein may be considered applicable to the trajectories based upon TD 123 motor data.

The information presented herein is based on theoretical estimates, supported and refined by subsonic, transonic, supersonic and hypersonic wind tunnel tests. These were conducted with scaled total configuration models for verification of total aerodynamic characteristics, and will full scale aft section for verification of tab effectiveness in roll.

II

VEHICLE DESCRIPTION

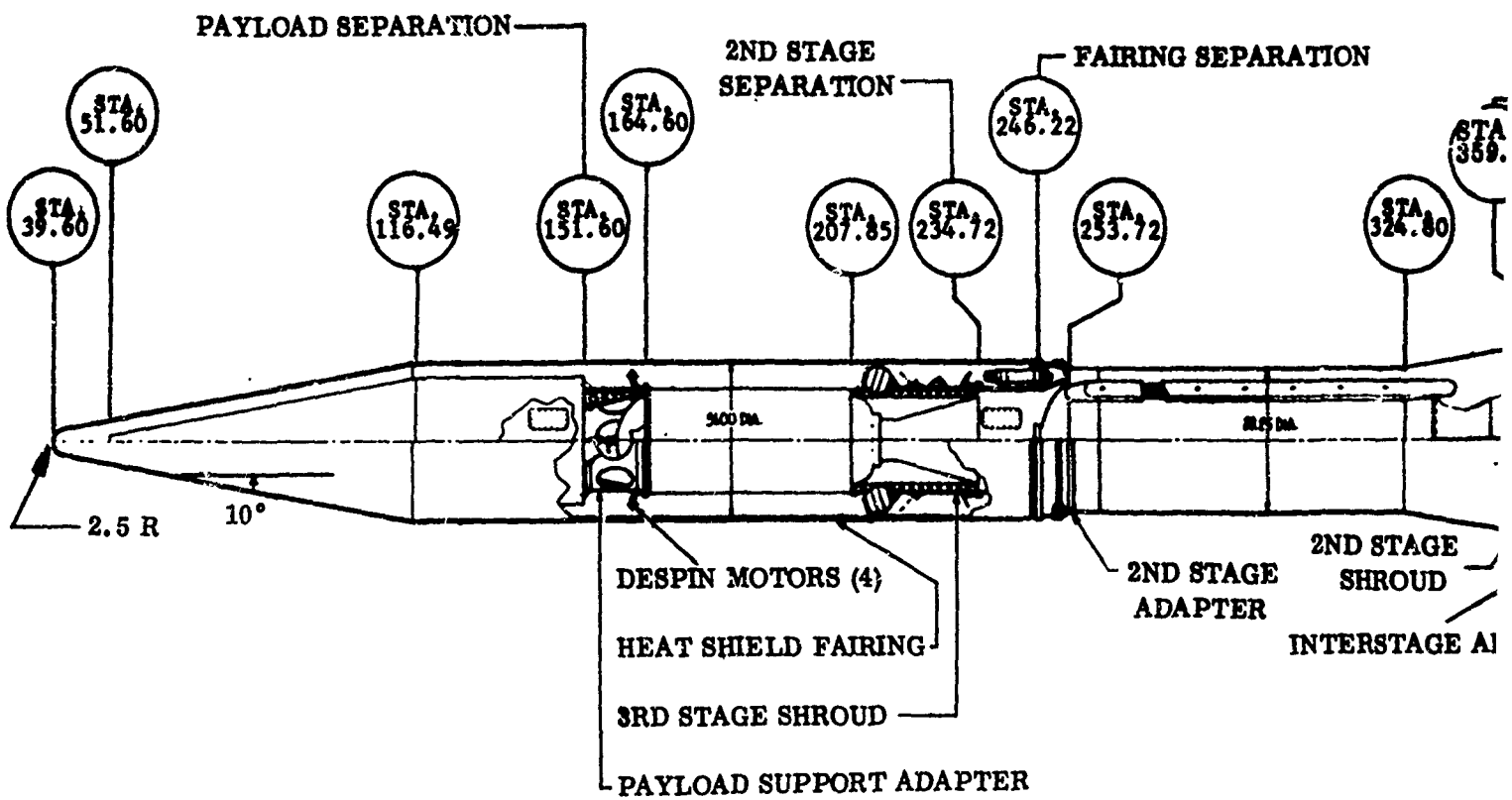
The ATHENA H vehicle defined by Atlantic Research Corporation/Missile Systems Division for the Air Force Space and Missile Systems Organization in support of the ABRES test program is shown in Figure 2-1.

The first stage booster consists of an Algol II-B or Castor IV solid propellant motor. It is augmented by four Recruit solid propellant motors which are retained during the boost flight. Atop each of the Recruit motors is placed a modified single wedge fin. These fins are designed to give minimum dispersion, adequate stability, and minimum roll damping at lift-off. A complete analysis of the fin selection study is given in Reference 1. Each fin has a wedge-shaped roll tab for roll augmentation. The fin and tab geometries appear in Figures 2-2 and 2-3, respectively.

Vehicle spin is achieved by means of two spin motors, canted fins, and roll tabs. The two spin motors are attached at approximately station 395. After spin motor burn-out, the motors are ejected to reduce vehicle drag. The spin profile is then controlled by the canted fins and roll tabs. The roll tabs are most effective at transonic speeds and reduce in effectiveness at increasing supersonic speeds. The fins are canted by 0.15 degrees and each tab has a wedge angle of twenty-five degrees relative to the fin surface. Tab size and fin cant angle has been selected such that a roll-yaw coupling possibility is minimized during the minimum spin rate at transonic speeds and also to provide a nominal steady state roll rate of 2.8 cycles per second at first stage burnout.

After first stage burnout, the velocity package is separated and despun before the heat shield is released. The second stage will include either a Hercules X-259 or Thiokol TX-261 solid propellant motor. This stage is attached to the first stage through an adapter section which contains the attitude controller. The attitude controller is released before second stage ignition.

The third stage includes a 23KS11,000 motor. Fitted to the third stage shroud are eight retrograde motors. After the third stage is despun and the payload ejected, the retro motors are used to ensure the maximum separation distance between the terminal stage and reentering payload.



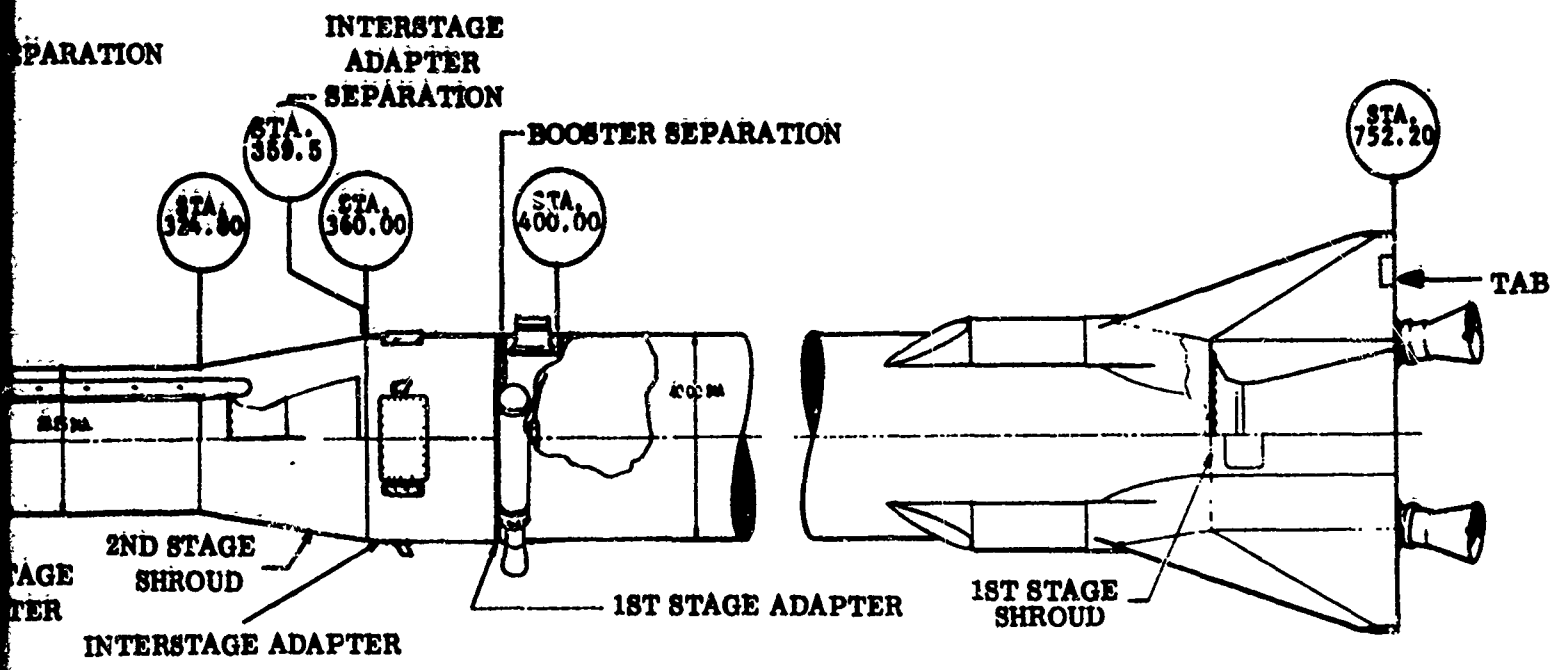
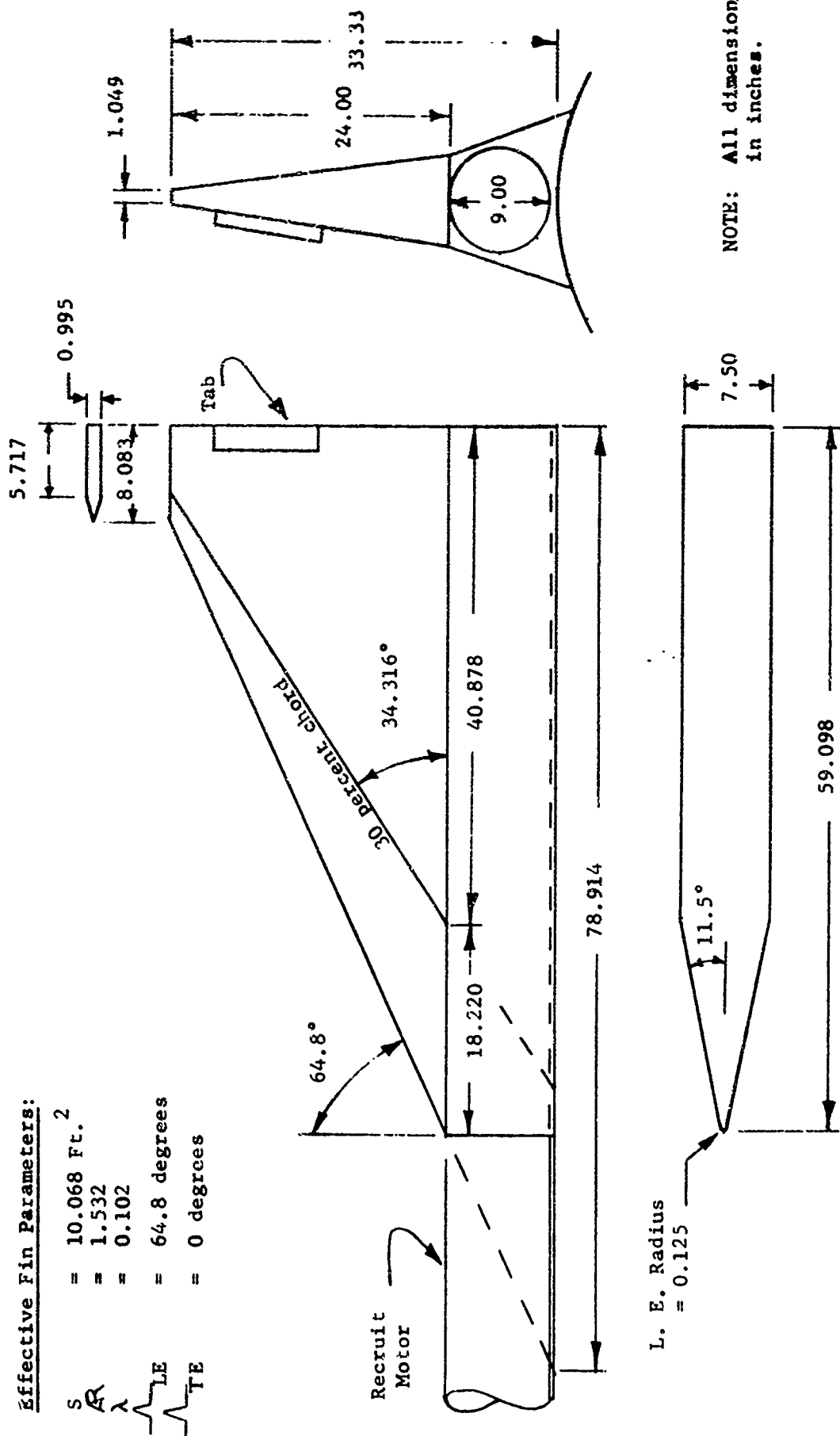


Figure 2-1. ATHENA H Profile

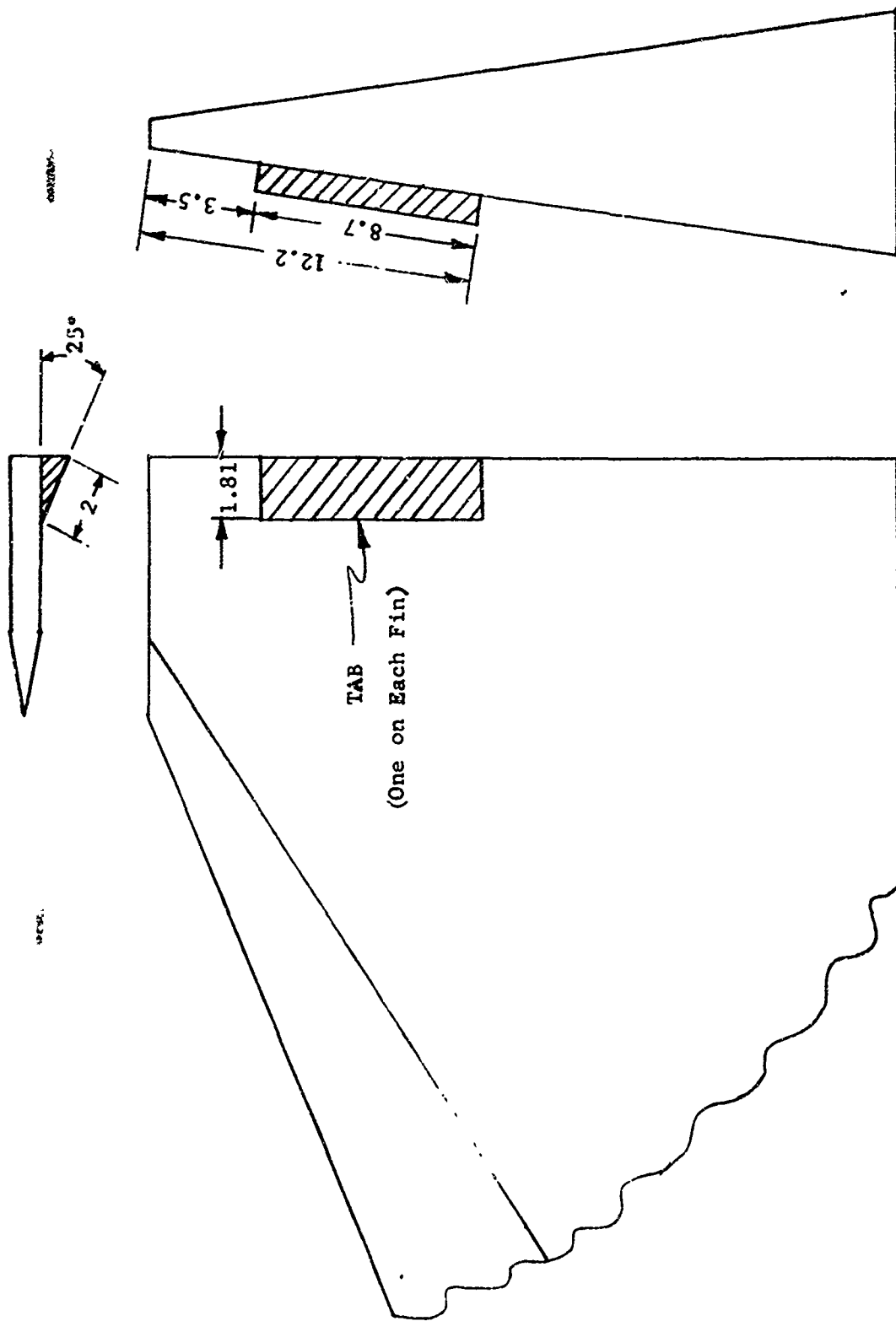
Effective Fin Parameters:

S = 10.068 Ft.²
 R = 1.532
 λ = 0.102
 α_{LE} = 64.8 degrees
 α_{TE} = 0 degrees



NOTE: All dimensions in inches.

Figure 2-2. ATHENA H Fin Geometry



NOTE: All dimensions in inches

Figure 2-3. ATHENA H Roll Tab Geometry

III

TOTAL VEHICLE AERODYNAMIC CHARACTERISTICS

3.1 GENERAL

Figures 3-1 through 3-15 and Tables 3-1 and 3-2 of this section present the boost phase aerodynamic characteristics for both the full configuration and for the velocity package. Figures 3-16 through 3-24 present axial force, normal force and pitching moment coefficients for the stable reentering first stage and average drag force coefficients for other tumbling ejected reentering stages and components. Figures 3-25 and 3-26 show the normal force parameter and center of pressure due to aerodynamic non-linearity. These non-linear coefficients will be used to simulate flights with real time winds to establish launcher settings. All the coefficients are based upon a reference area of 8.727 square feet and a reference length of 3.333 feet (the cross-sectional area and diameter of the first stage motor). These total vehicle aerodynamic characteristics were generated in support trajectory analyses.

Differences between the TX-261 and X-259 were assumed to be negligible when accounting for total vehicle aerodynamics. The coefficients presented herein are to be used for flight simulation.

3.2 BOOST PHASE AERODYNAMIC DATA

3.2.1 Longitudinal Stability Characteristics

Normal force slope and pitching moment slope are presented as a function of Mach number in Figures 3-1 and 3-2. These derivatives are shown in the Mach number range from 0 to 10.

To develop the total vehicle longitudinal aerodynamics, analytical methods were used. The analytical results were refined by numerous wind tunnel tests for the ATHENA H configuration. A variety of wind tunnel tests were conducted at subsonic, transonic, supersonic and hypersonic speeds. These tests and their results are described in Reference 1.

The effect upon normal force due to pitching rate is shown in coefficient form in Figure 3-3. This coefficient accounts for additional sources of normal force due to transient pitching rates during flight. The pitch damping coefficient is shown as a function of Mach number in Figure 3-4. The coefficients in Figures 3-3 and 3-4 reflect the wind tunnel test results provided in Reference 1.

3.2.2 Lateral Stability Characteristics

Figures 3-5 and 3-6 show the total vehicle roll forcing and roll damping coefficients versus Mach number, respectively. These coefficients reflect the wind tunnel results of Reference 1. Figure 3-7 depicts the tab effectiveness by presenting the tab roll forcing coefficients versus Mach number. These coefficients were based on wind tunnel results of the full size aft section of the ATHENA II configuration. The test results are presented in Reference 2.

3.2.3 Directional Stability Characteristics

The side force coefficient slope, the yawing moment coefficient slope and the side force due to yaw rate are considered to be equal and opposite in sign to the normal force coefficient slope of Figure 3-1, the pitching moment coefficient slope of Figure 3-2 and the normal force due to pitching rate coefficient of Figure 3-3. The yaw damping coefficient is considered to be equal to the pitch damping coefficient as presented in Figure 3-4.

3.2.4 Static Stability Margin Requirements

Figure 3-8 describes the basis for establishing the specification that the vehicle cg will not be aft of Station 490 at Mach number = 5.0. At that Mach number the static margin is minimum and the center of pressure is at Station 510. A static margin requirement of twenty (20) inches was selected and this restricted the aft-most cg portion of station 490 at Mach number = 5.0. Figure 3-8 shows that such a static margin requirement is met by comparing the co and a worst case cg history corresponding to a two-stage configuration with 0.0 pounds payload weight and 0.0 pounds ballast weight. Other configurations will have cg locations forward of those corresponding to this critical configuration.

3.2.5 Axial Force Characteristics

Total vehicle zero angle of attack drag coefficients are presented as functions of Mach number in Figures 3-9, 3-10, and 3-11 for Mach numbers from 0 to 10.

Figure 3-9 shows the CIS phase theoretical drag estimate which was used in defining specification performance and the specification weight of the vehicle. Upon completion of wind tunnel tests conducted after the CIS phase, this drag estimate was updated in order to incorporate the wind tunnel test results. The original drag update was based upon the preliminary wind tunnel test results and was adjusted for effects of the discontinuities and protuberances which existed on the prototype vehicle, but were not present on the wind tunnel model.

The specification weight was then revised to be consistent with the new drag estimate. Subsequently, it was found that due to incorrect data reduction, the original supersonic wind tunnel drag coefficients were too high. The drag estimate was then adjusted to incorporate the corrected test data and also to include the effects of the addition of fin tabs for improved roll control. To this new drag was added a conservative estimate for protuberance drag to allow for future additions of discontinuities and protuberances. This drag was then used as a basis for revising the specification weight. This drag estimate is presented in Figure 3-10 and is identified as "specification" drag. Figure 3-11 shows a "best estimate" drag which represents the revised wind tunnel data combined with a realistic estimate of current protuberance drag. The "best estimate" drag was used for shaping the design trajectories. The drag in both Figures 3-10 and 3-11 are presented during four phases of flight:

- (1) Launch until Recruit burnout.
- (2) Recruit burnout until spin motor ejection.
- (3) Spin motor ejection until booster burnout.
- (4) Booster burnout until first stage separation.

In the past, for booster dispersion analysis, a flight-to-flight variation of vehicle drag coefficient of 10 per cent had been assumed in order to provide a budget for drag variation. In view of the present estimates of flight-to-flight variation in drag coefficients, 10 per cent uncertainty appears to be unrealistically high. Table 3-1 tabulates the incremental drag at Mach number = 3.0 due to all of the various discontinuities, band protrusions, access door gaps, and various other crevices and protrusions. It is reasonable to expect that the variation in drag from flight-to-flight will not exceed the total incremental drag presented in Table 3-1. Since the total incremental drag amounts to only 2.4 per cent of the total vehicle drag at Mach number = 3.0, it is reasonable to assume that the variations in drag from flight-to-flight will also remain below 2.4 per cent of the total vehicle drag.

3.2.6 Spin Profiles

Based upon the ATHENA H aerodynamic characteristics presented herein and nominal three-stage vehicle design trajectories, time histories of the aerodynamic spin profiles supplemented by two (2) Thiokol TX-55-4 spin motors were established. Typical spin profiles for both high and low reentry angle trajectories are shown for the Algol II-B and the Castor IV boosted trajectories in Figures 3-12 and 3-13, respectively. As mentioned in Section 2, the combination of fin cant angle and tab size was selected to both preclude roll-yaw coupling tendencies at transonic speeds and also to preclude excessive steady state spin rate at booster burnout.

Also, included in each figure is a time history of the maximum natural pitch frequency of the vehicle to show the relative margin between the spin rate and natural pitch frequency.

3.2.7 Velocity Package Aerodynamic Data

The velocity package is the remaining portion of the vehicle forward of station 390.75, after the first stage is ejected. Figure 3-14 presents axial force coefficient versus Mach number. This curve was based on body-alone wind tunnel tests for the wind tunnel model and flight data of the Standard ATHENA second stage. Table 3-2 tabulates the static and dynamic longitudinal and directional stability derivatives for several Mach numbers. These were computed for Mach number of 6 using body-alone wind tunnel results of Reference 1, and data for Standard ATHENA second stage coast. It was assumed that beyond Mach 6 the coefficients would be very slightly reduced, and that it would be conservative to use the results corresponding to Mach 5.

3.3 REENTRY AERODYNAMICS

Figures 3-15 through 3-24 describe the aerodynamics for the ATHENA H components during reentry. With the exception of the first stage booster, the yo-yo weights-with-trailing-tapes and the heat shield halves, all components were assumed to be tumbling. This assumption is supported by analysis as well as Standard ATHENA flight data. Each heat shield half was determined by analysis to reenter spinning about its longitudinal axis with the longitudinal axis oriented almost normal to its relative velocity vector (Figure 3-19). For reference, Figure 3-20 shows zero-angle-of-attack drag area for the heat shield half. Drag area of the complete reentering velocity package, (without heat shield) is presented in Figure 3-17. The other components for which reentry drag areas are presented are the upper stages, interstage adapter, spin motors, and the various V-bands and flat-bands. The drag data for components of the reentering booster were obtained from References 1 and 4. The drag for the tumbling components represents an average of the integrated drag during any one cycle of the tumbling motion. For each component such integration was performed for a curve-fitted variation of drag versus attitude. Drag data for specific attitudes were obtained for each component for Reference 4. Figures 3-23 and 3-24 show the booster reentry normal force coefficient slope and pitch moment coefficient slope, respectively, both as functions of Mach number.

3.4 NON-LINEAR LONGITUDINAL STABILITY CHARACTERISTICS

Prior to each ATHENA H launch, the Atmospheric Sciences Laboratory's Digital Computer Program for Five-Degree-of-Freedom Trajectory, (ASO-5D) of Reference 3, will be used in order to establish the launch setting to compensate for

booster dispersion resulting from winds aloft. At launch when the vehicle velocity is relatively low, a high wind velocity may cause angles of attack which exceed the value for which linear aerodynamic data are applicable. Therefore, for realistic wind compensation during boost flight, non-linear aerodynamics are useful. Figures 3-25 and 3-26 present the normal force and center of pressure beyond the linear angle of attack range. The data was based on wind tunnel tests of Reference 1. To comply with the program inputs formats, the normal force is shown as a derivative with respect to $\sin \alpha$ versus Mach number, for a family of angles of attack in Figure 3-25. Figure 3-26 illustrates the variation of center of pressure, as a function of Mach number, for a range of angles of attack. The other aerodynamic coefficients used by the ASO-5D program are the pitch damping coefficients, C_{m_q} , and axial force coefficients. The pitch damping coefficient is independent of angle of attack and the axial force coefficient is affected only by a negligible amount within the expected angle of attack range. Therefore, the pitch damping coefficient of Figure 3-4 and axial force coefficient of Figure 3-11 is to be used for the ASO-5D.

TABLE 3-1

ATHENA H ZERO-LIFT DRAG INCREMENT

$$S_{\text{ref}} = 8.727 \text{ Ft.}^2$$

CONTRIBUTOR	$C_D @ M = 3.0$
1. Discontinuities	0.0087
2. Flat & V-Bands	0.0029
3. Access Doors	0.0006
4. Turnbuckle Openings	<u>0.0010</u>
TOTAL	0.0132

TABLE 3-2

ATHENA H VELOCITY PACKAGE AERO DATA

$$S_{\text{ref}} = 8.727 \text{ Ft.}^2$$

$$d_{\text{ref}} = 3.33 \text{ Ft.}^2$$

MACH	C_{N_α} (1) Per Deg.	C. P. STA	C_{m_α} (2) Per Deg.	C_{N_q} (3) Per Rad.	C_{m_q} (4) Per Rad.
6	0.0589	219.89	-0.324	-6.78	-60.72
7	0.0589	219.89	-0.324	-6.78	-60.72
8	0.0589	219.89	-0.324	-6.78	-60.72

$$(1) \quad C_{Y_\beta} = -C_{N_\alpha}$$

$$(2) \quad C_{n_\beta} = -C_{m_\alpha} \text{ (w.r.t. Sta. 0.0)}$$

$$(3) \quad C_{Y_r} = C_{N_q}$$

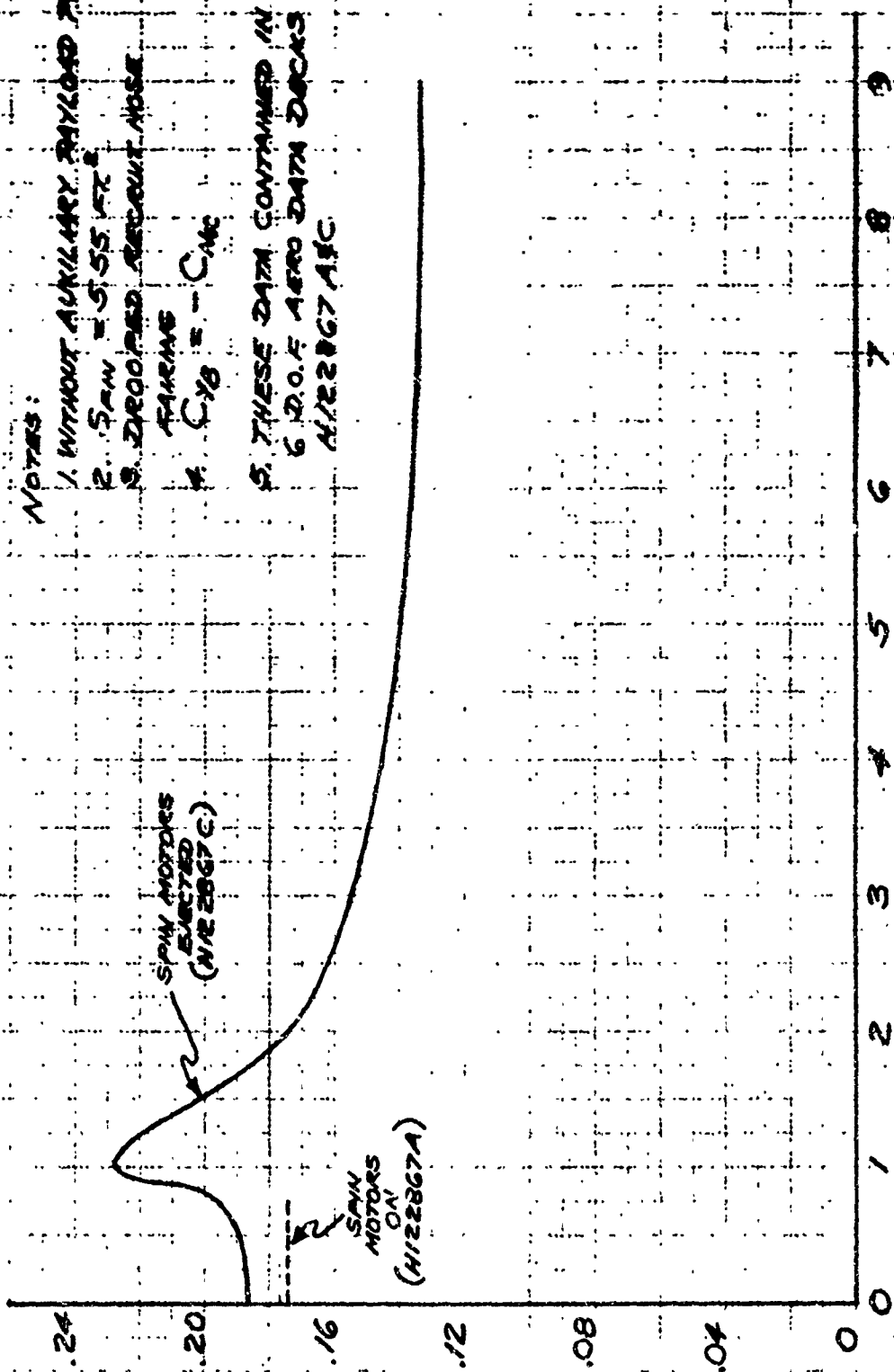
$$(4) \quad C_{n_r} = C_{m_q}$$

ATHENA H

NORMAL FORCE COEFFICIENT

$S_{REF} = 8.727 \text{ FT}^2$

$C_{N\alpha} \sim \text{NORMAL FORCE COEFF. SLOPE} \sim \text{PER DEG.}$



NOTES:

1. WITHOUT AUXILIARY PAYLOAD PODS
2. $S_{AW} = 5.55 \text{ FT}^2$
3. DROOPED REAROUT NOSE FAIRING
4. $C_{YB} = -C_{N\alpha}$
5. THESE DATA CONTAINED IN 6 D.O.F. AERO DATA DECKS N122867 A1C

MACH NUMBER

Figure 3-1. Normal Force Coefficient Slope

ATHENA H

PITCHING MOMENT COEFFICIENT

$S_{REF} = 8.727 \text{ FT}^2$

$C_{REF} = 3.333 \text{ FT}$

NOTES:

1. WITHOUT AUX. PAYLOAD PODS
2. $S_{FW} = 5.55 \text{ FT}^2$
3. DROOPED REARUP NOSE FAIRING
4. $C_{MG} = -0.006$
5. THESE DATA CONTAINED IN G.D.O.F. AERO DATA DECKS H/2286741C

PITCHING MOMENT COEFF. SLOPE ~ C_{MAC} @ STATION ZERO ~ PER DEGREE

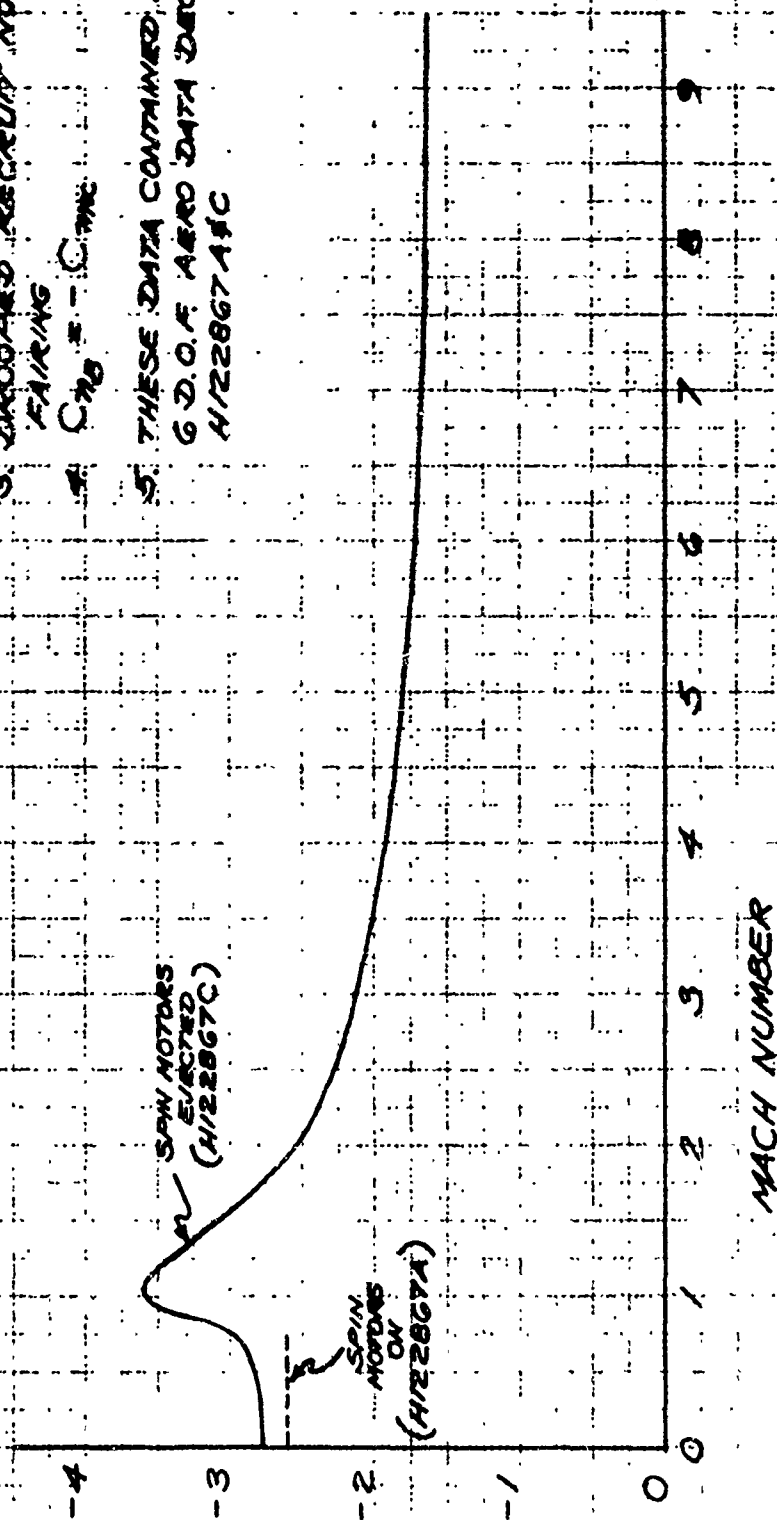


Figure 3-2. Pitching Moment Coefficient Slope

ATHENA H NORMAL FORCE DUE TO PITCHING RATE

$$S_{REF} = 8.727 \text{ FT}^2$$

$$L = 3.33 \text{ FT}^2$$

NORMAL FORCE DUE TO PITCHING, $C_{N\dot{\alpha}}$ (PER RADIAN)

8153-II

NOTES:

- ① FIN SIZE = 5.55 FT²
- ② NO AUXILIARY PL RODS
- ③ DROOPED RECRUIT NOSE FAIRING
- ④ THESE DATA CONTAINED IN 6 D.O.F. AERD DATA DECKS H122867A & C
- ⑤ $C_{N\dot{\alpha}} = 2C_m / \dot{\alpha} \left(\frac{\dot{\alpha} d}{2V} \right)$
 $C_m = \frac{\text{NORMAL FORCE}}{\frac{1}{2} \rho V^2 S_{REF}}$
 $V = \text{FREE STREAM VEL. (FT/SEC)}$
 $\dot{\alpha} = \text{PITCH RATE (RAD/SEC)}$

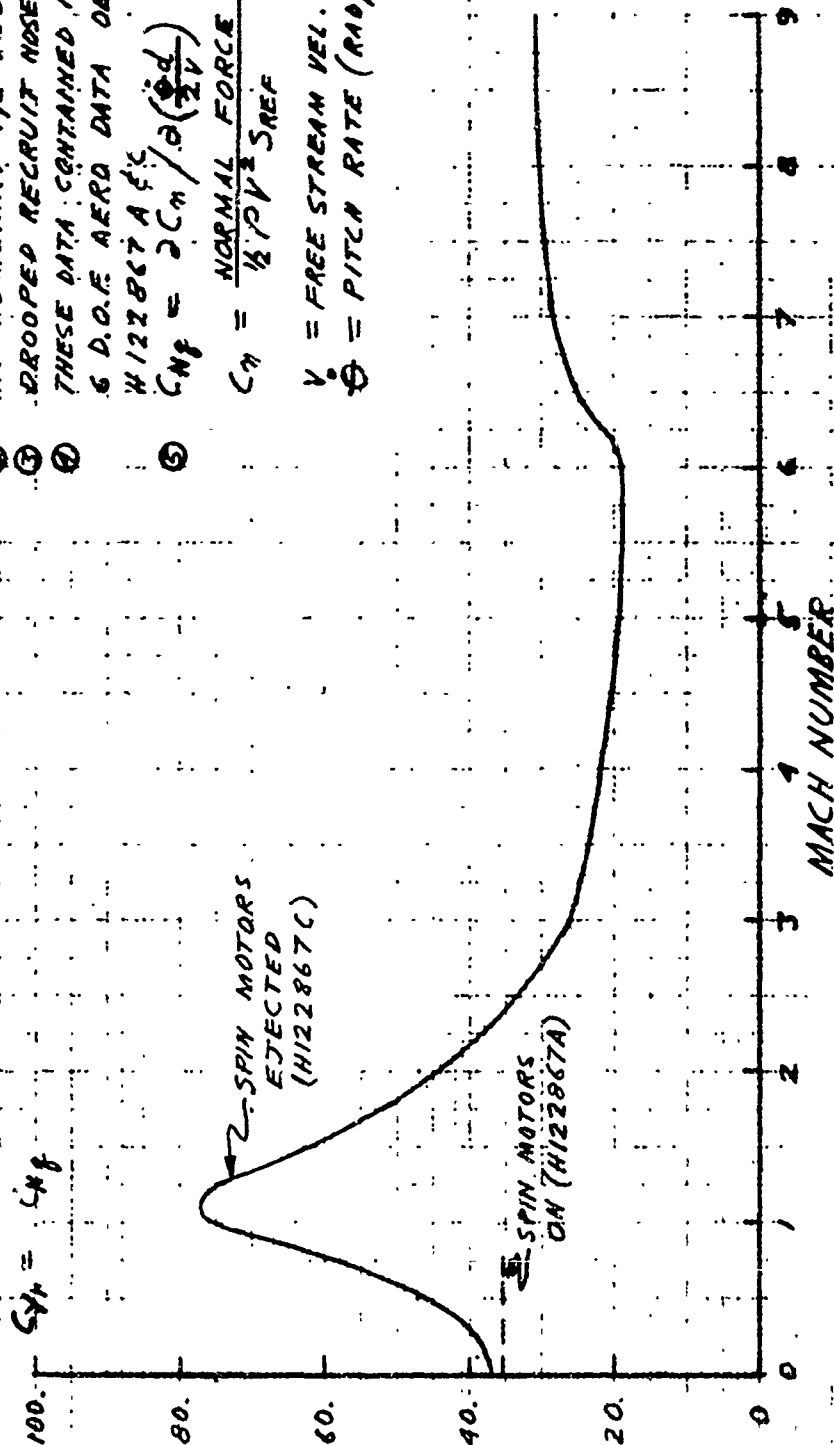
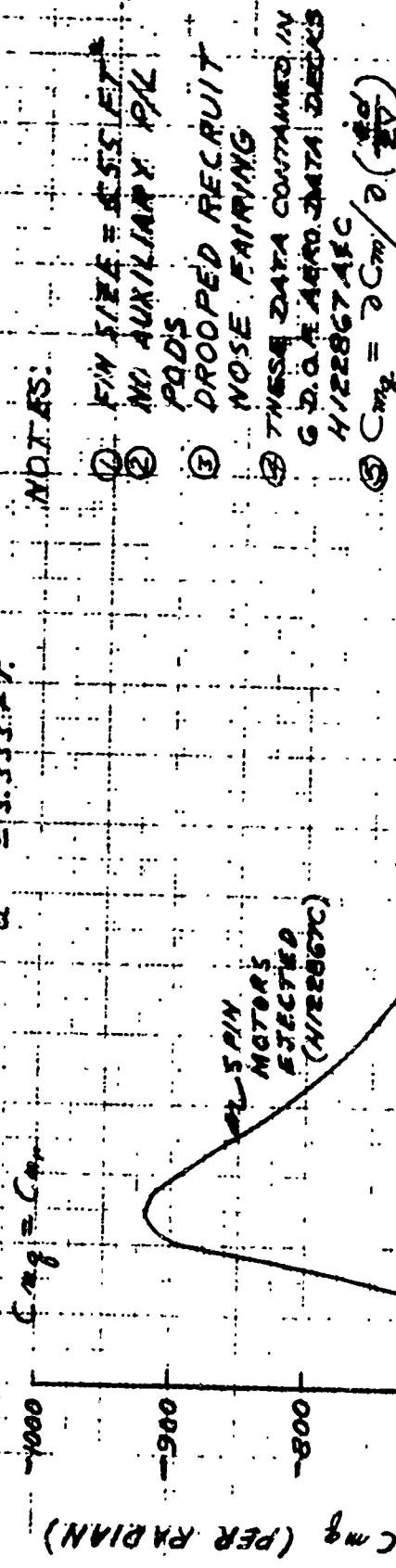


Figure 3-3. Normal Force Due to Pitching Rate

ATHENA H

PITCH DAMPING COEFFICIENT VS MACH NO.

$S_{REF} = 8.727 \text{ FT}^2$
 $d = 3.333 \text{ FT}$



NOTES:

- ① FIN SIZE = 455 FT²
- ② NO AUXILIARY PKL PODS
- ③ DROOPED RECRUIT NOSE FAIRING
- ④ THESE DATA CONTAINED IN G.D.O. AIRFO. DATA DECKS H122867A & C
- ⑤ $C_{mq} = \frac{\partial C_m}{\partial \dot{\alpha}} \left(\frac{d}{V} \right)$

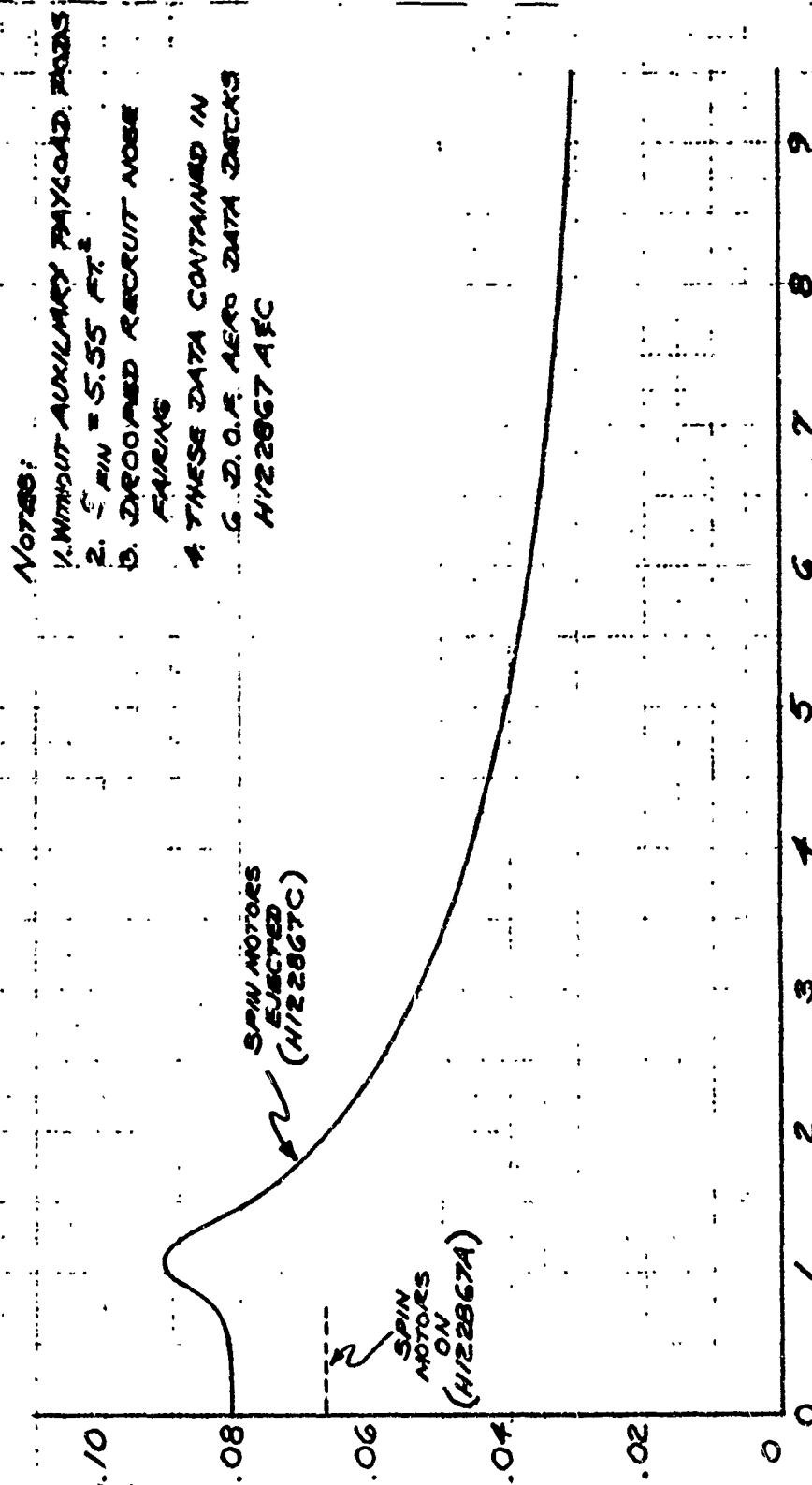
$$C_m = \frac{\text{PITCHING MOM. ABOUT C.G.}}{\frac{1}{2} \rho V^2 S_{REF} d}$$

V = FREE STREAM VEL. (FT/SEC)
 $\dot{\alpha}$ = PITCH RATE (RAD/SEC)

Figure 3-4. Pitch Damping Coefficient

ATHENA H
FIN EFFECTIVENESS IN ROLL
WITHOUT ROLL TABS
SREF = 8.727 FT.²
CREF = 3.333 FT.

$C_{L_s} \sim$ ROLL FORCING COEFFICIENT ~ PER DEG.



MACH NUMBER

Figure 3-5. Fin Effectiveness in Roll

ATHENA H
DAMPING IN ROLL DERIVATIVE
INDEPENDENT OF TAB PRESENCE
 $S_{RP} = 8.727 \text{ FT.}^2$
 $C_{RP} = 3.333 \text{ FT.}^2$

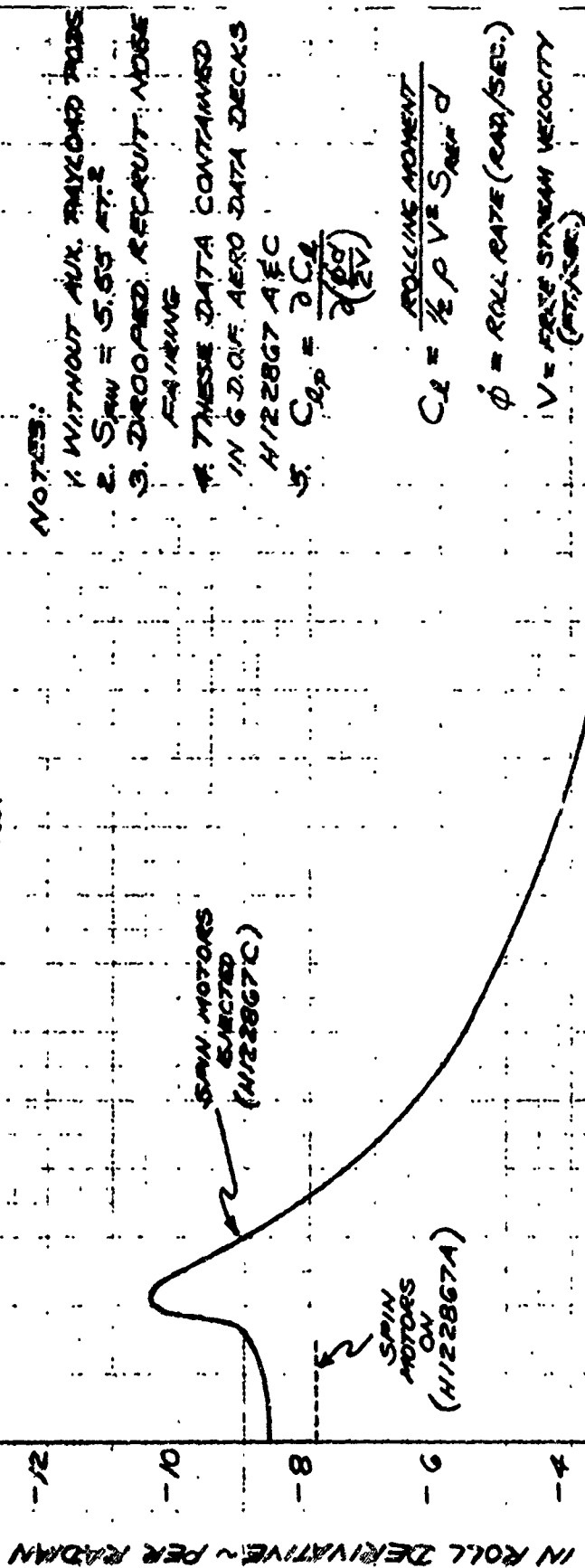
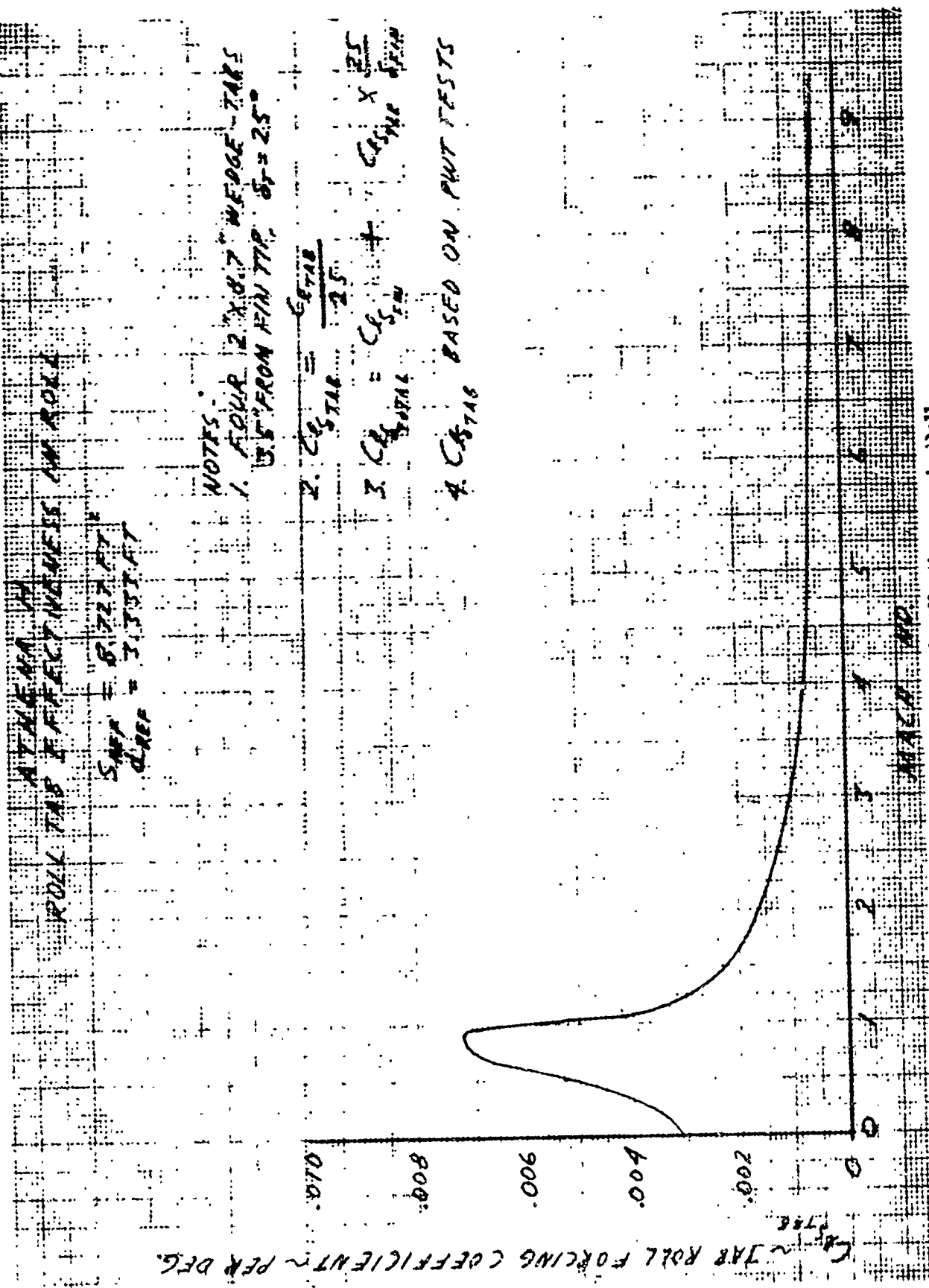


Figure 3-6. Damping in Roll Derivative



AT THE END OF
ROLL TAB EFFECTIVENESS IN ROLL

$$S_{REF} = 0.022 \text{ FT}^2$$

$$d_{REF} = 3.333 \text{ FT}$$

- NOTES:
1. FOUR 2" X 8.7" WEDGE TABS
0.5" FROM FIN TIP, $\delta = 25^\circ$
 2. $C_{R\ TAB} = \frac{C_{R\ TAB}}{25}$
 3. $C_{R\ TOTAL} = C_{R\ TAB} + C_{R\ FIN}$
 4. $C_{R\ TAB}$ BASED ON PNT TESTS

Figure 3-7. Roll Tab Effectiveness in Roll

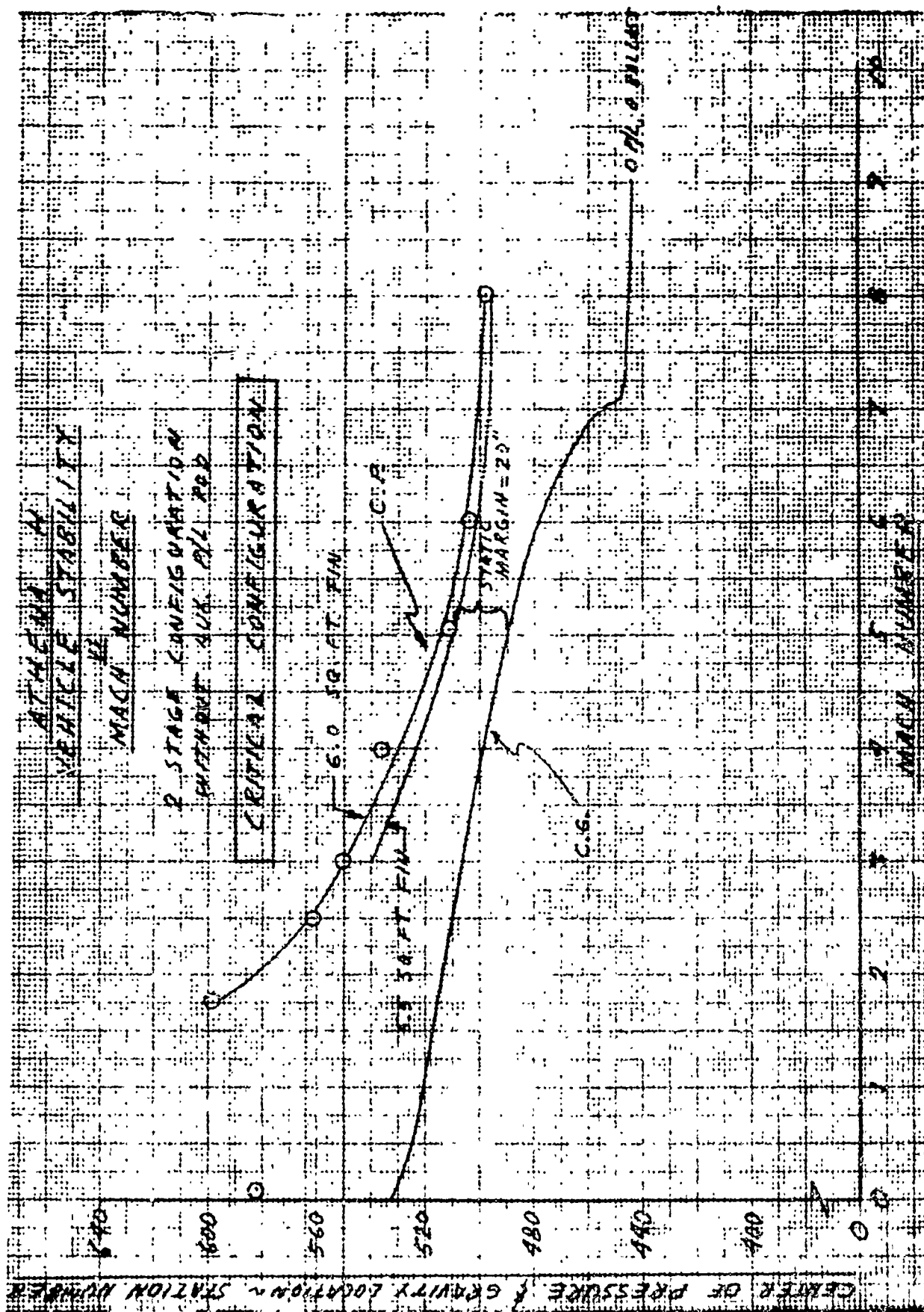


Figure 3-8. Vehicle Stability versus Mach Numbers



Figure 3-9. Zero Lift Drag Coefficient

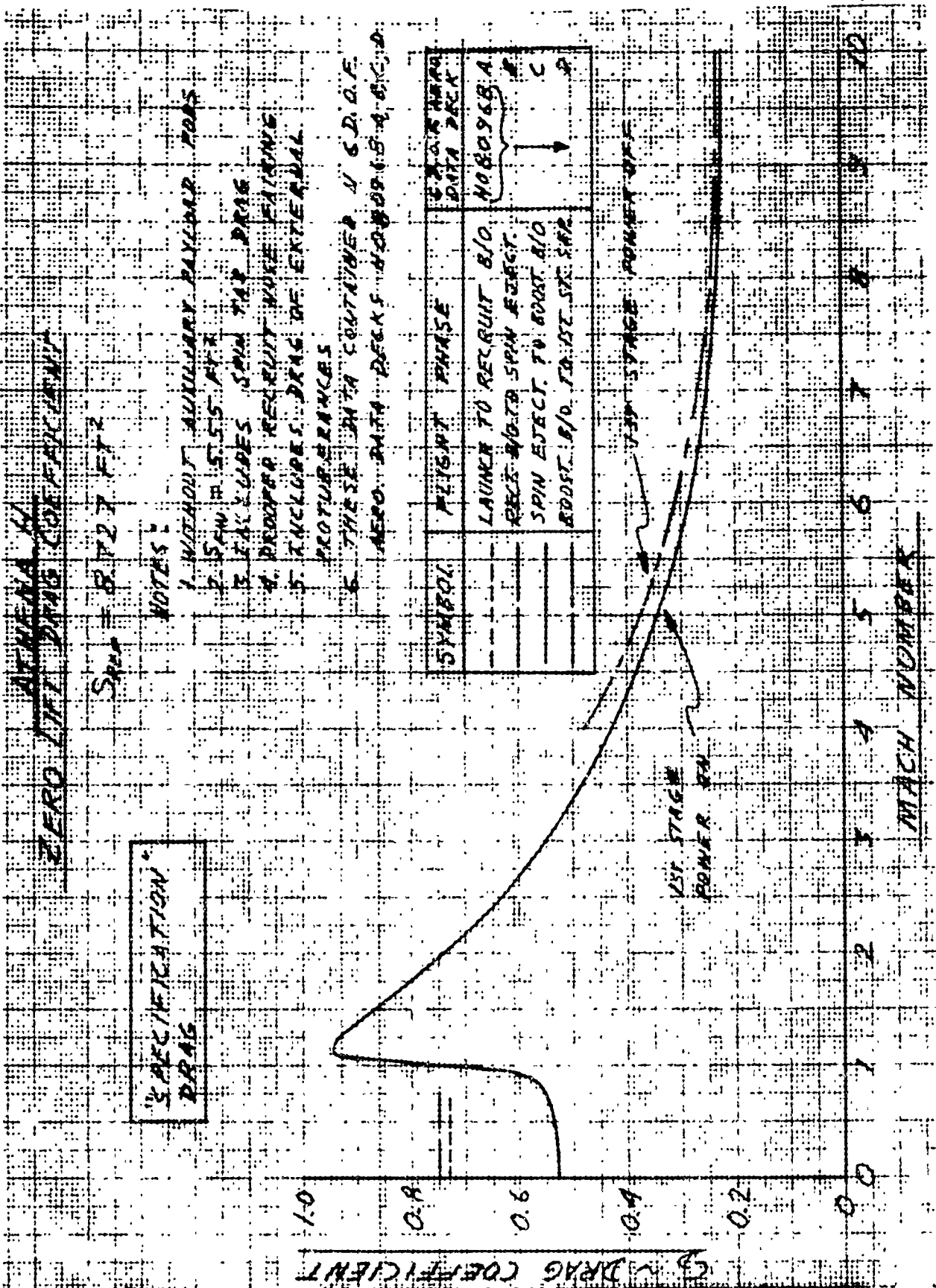


Figure 3-10. Zero Lift Drag Coefficient ("Specification" Drag)

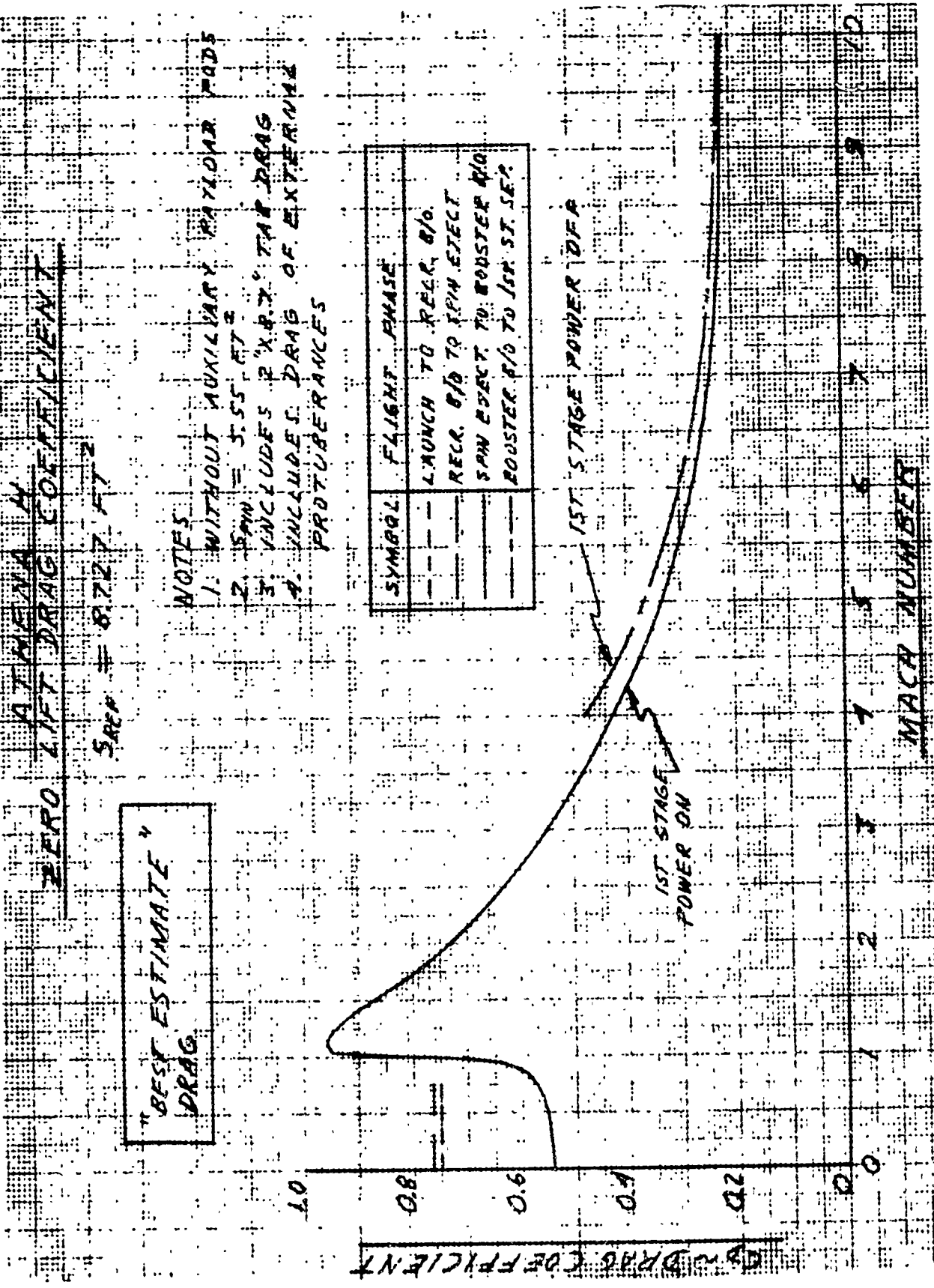


Figure 3-11. Zero Lift Drag Coefficient ("Best Estimate" Drag)

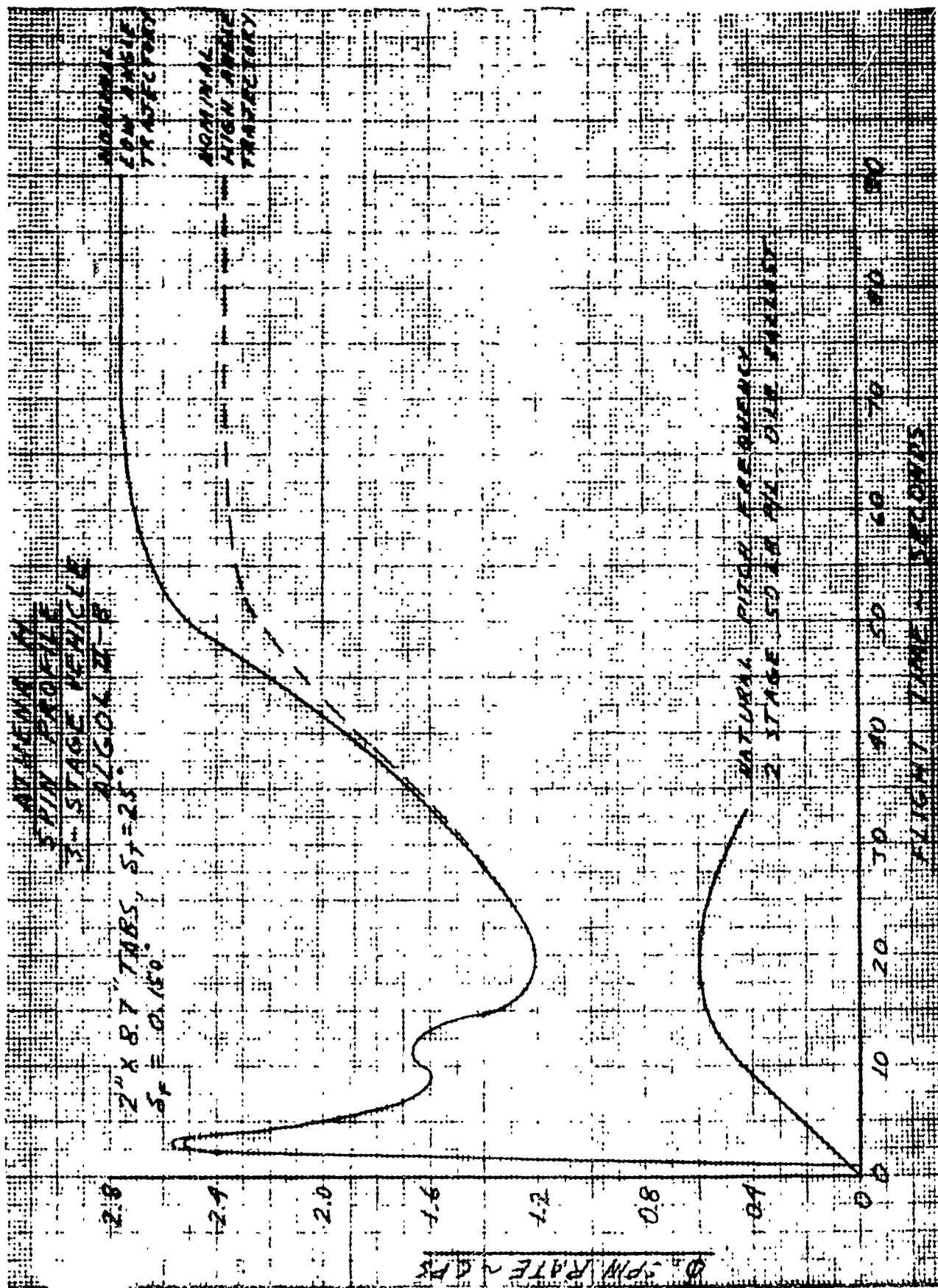


Figure 3-12. Spin Profile, 3-Stage Vehicle (Algol II-B)

ATHENA H.
SPIN PROFILE
3-STAGE VEHICLE
CASTOR IV (TPMF)

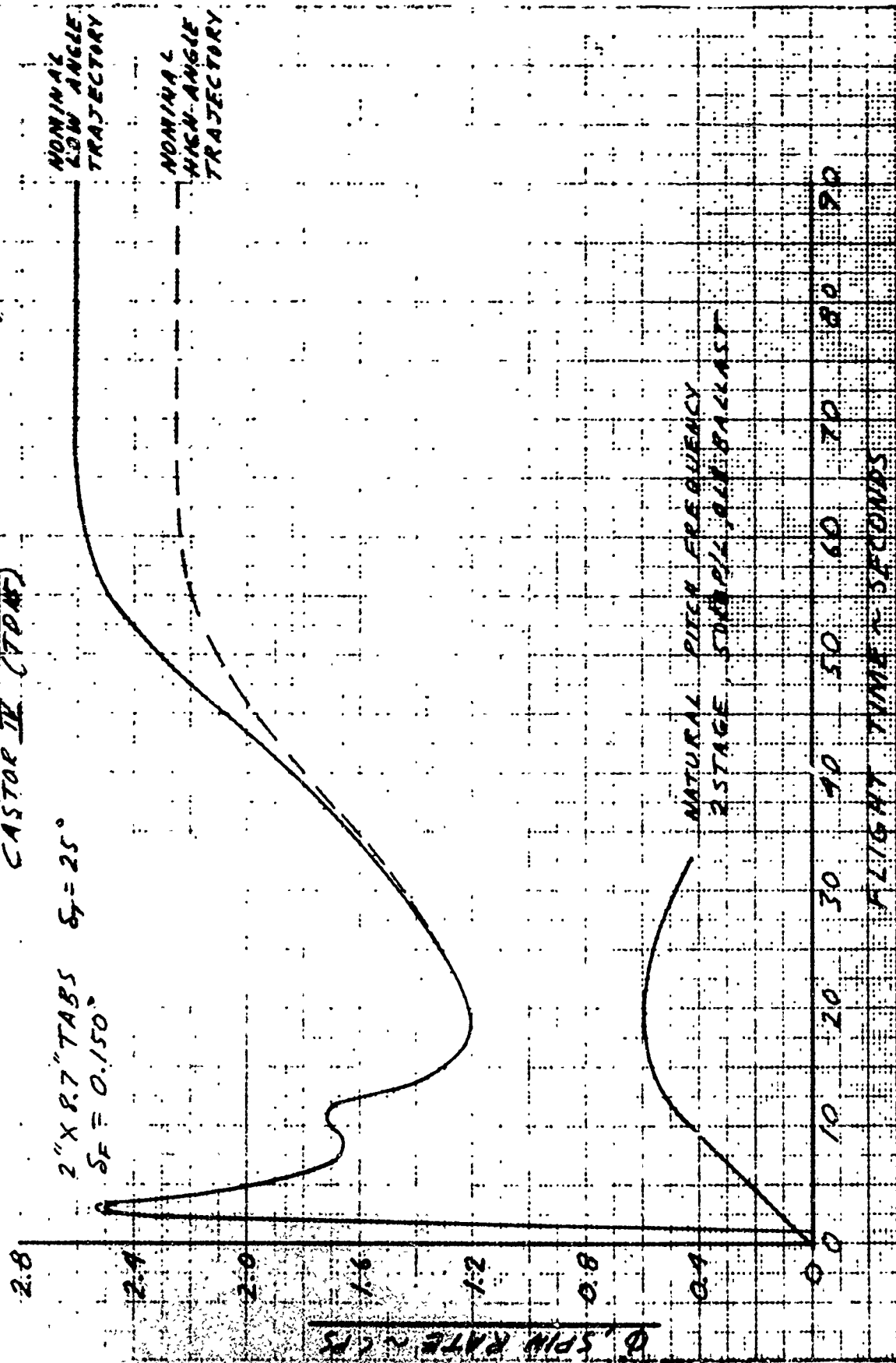


Figure 3-13. Spin Profile, 3-Stage Vehicle (Castor IV)

ATHENA H VELOCITY PACKAGE DRAG

$S_{REF} = 8.727 \text{ FT}^2$

$\alpha = 0^\circ$

ZERO LIFT DRAG COEFFICIENT

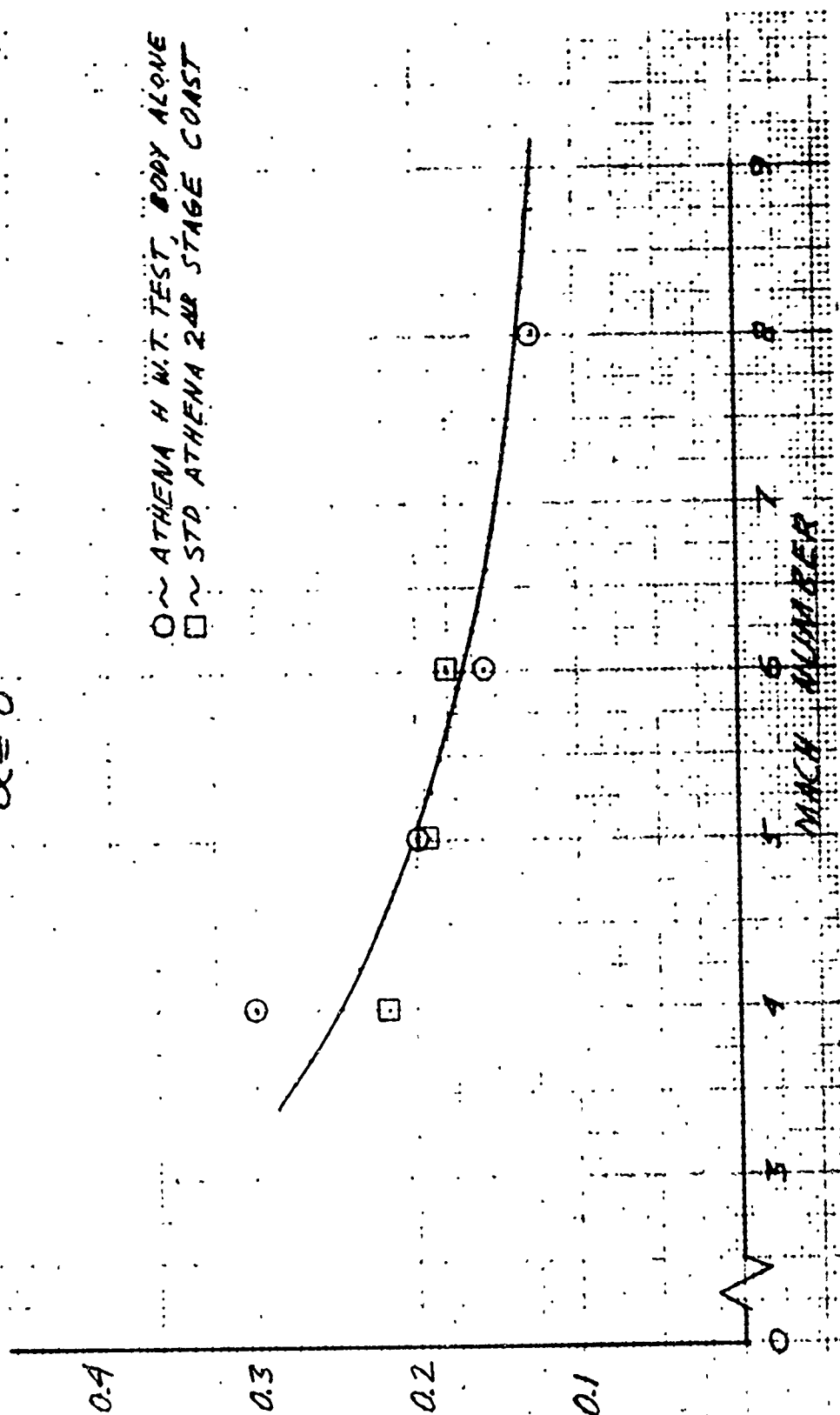


Figure 3-14. Velocity Package Drag

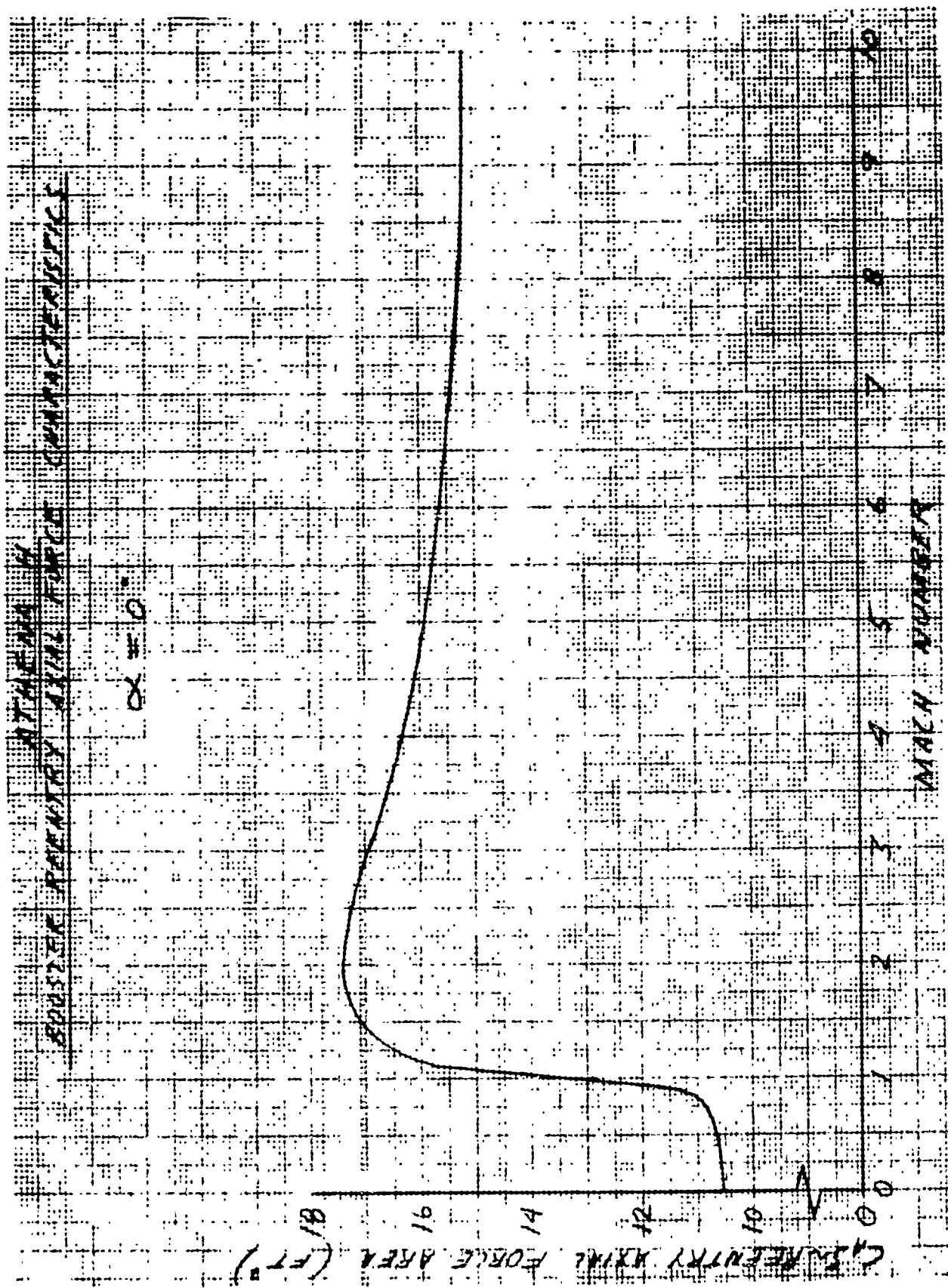


Figure 3-15. Booster Reentry Axial Force Characteristics

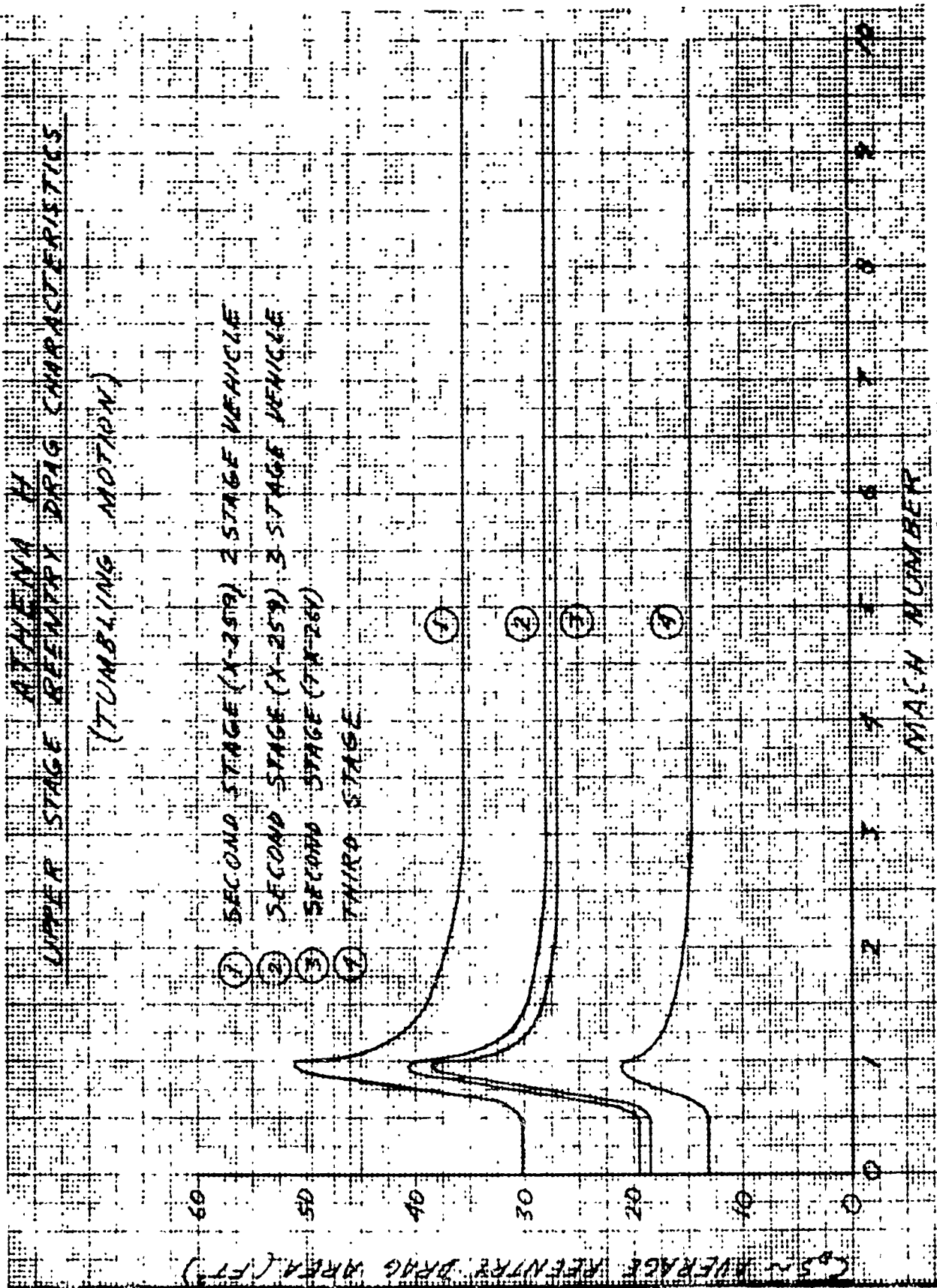


Figure 3-16. Upper Stage Reentry Drag Characteristics

ATHENA H VELOCITY PACKAGE REENTRY DRAG CHARACTERISTICS (TUMBLING MOTION)

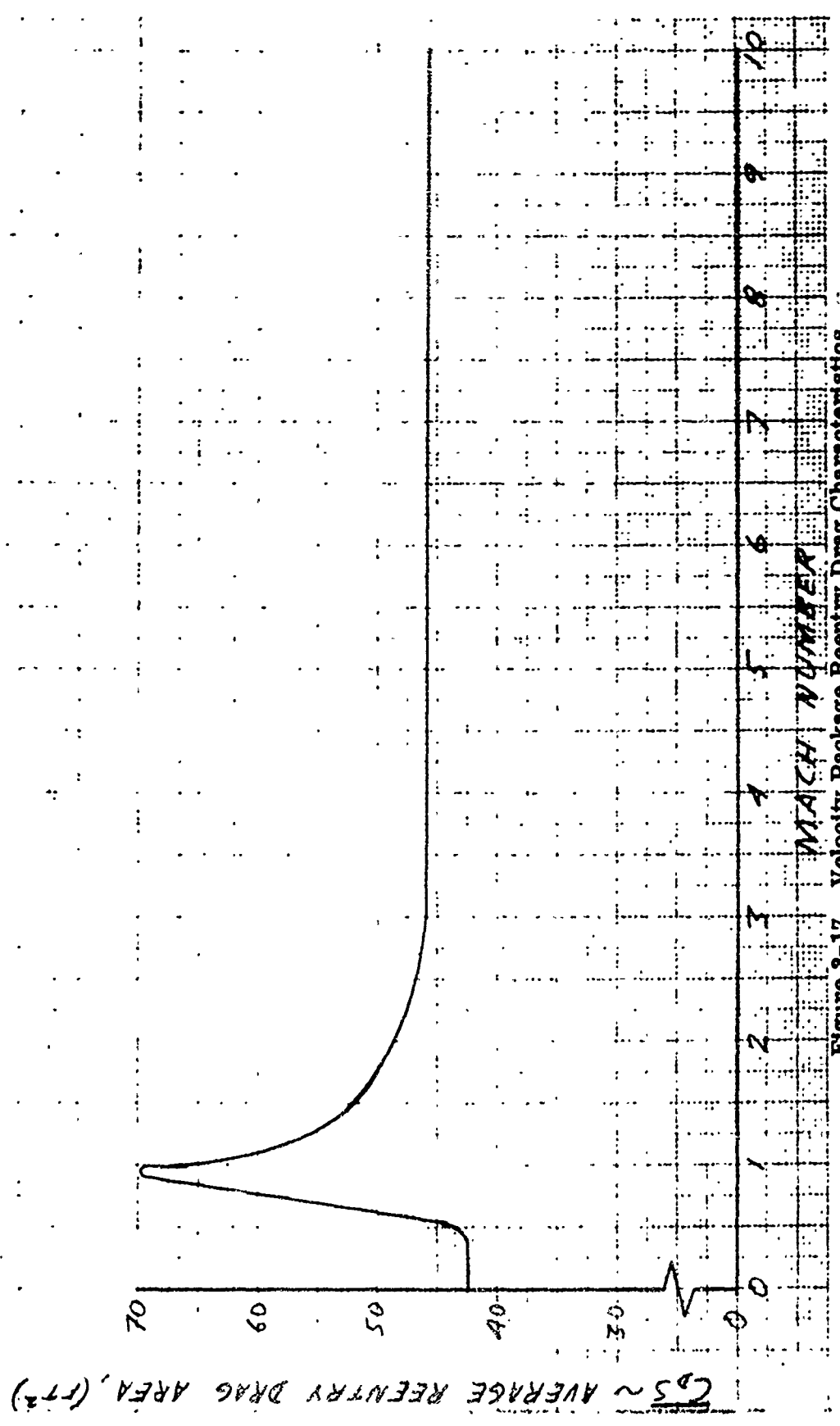


Figure 3-17. Velocity Package Reentry Drag Characteristics

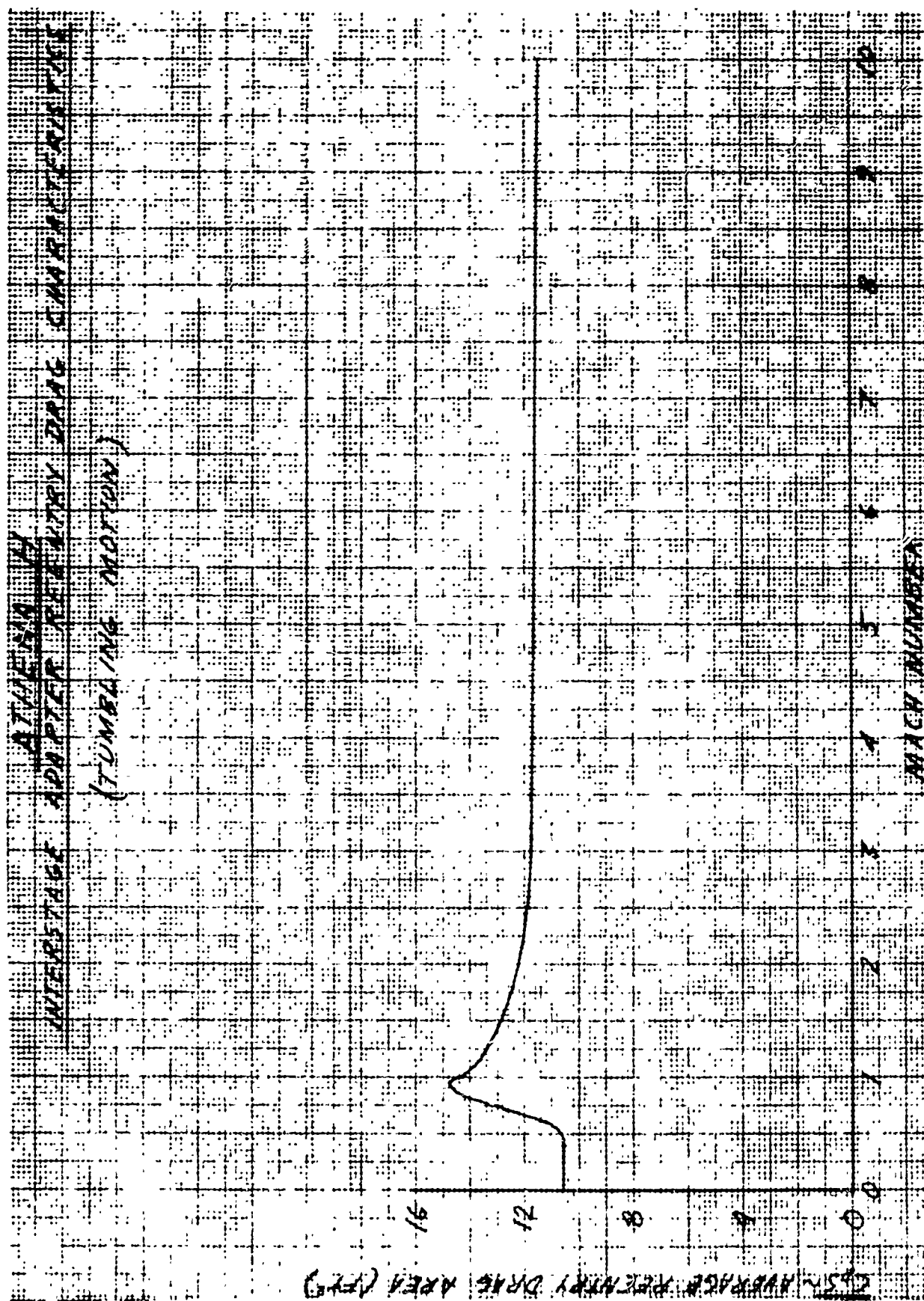


Figure 3-18. Interstage Adapter Reentry Drag Characteristics

HEAT SHIELD HALF REENTRY DRAG CHARACTERISTICS

REENTRY ATTITUDE: SPINNING ABOUT LONGITUDINAL AXIS

COEFFICIENT OF DRAG AREA (FT²)

MACH NUMBER

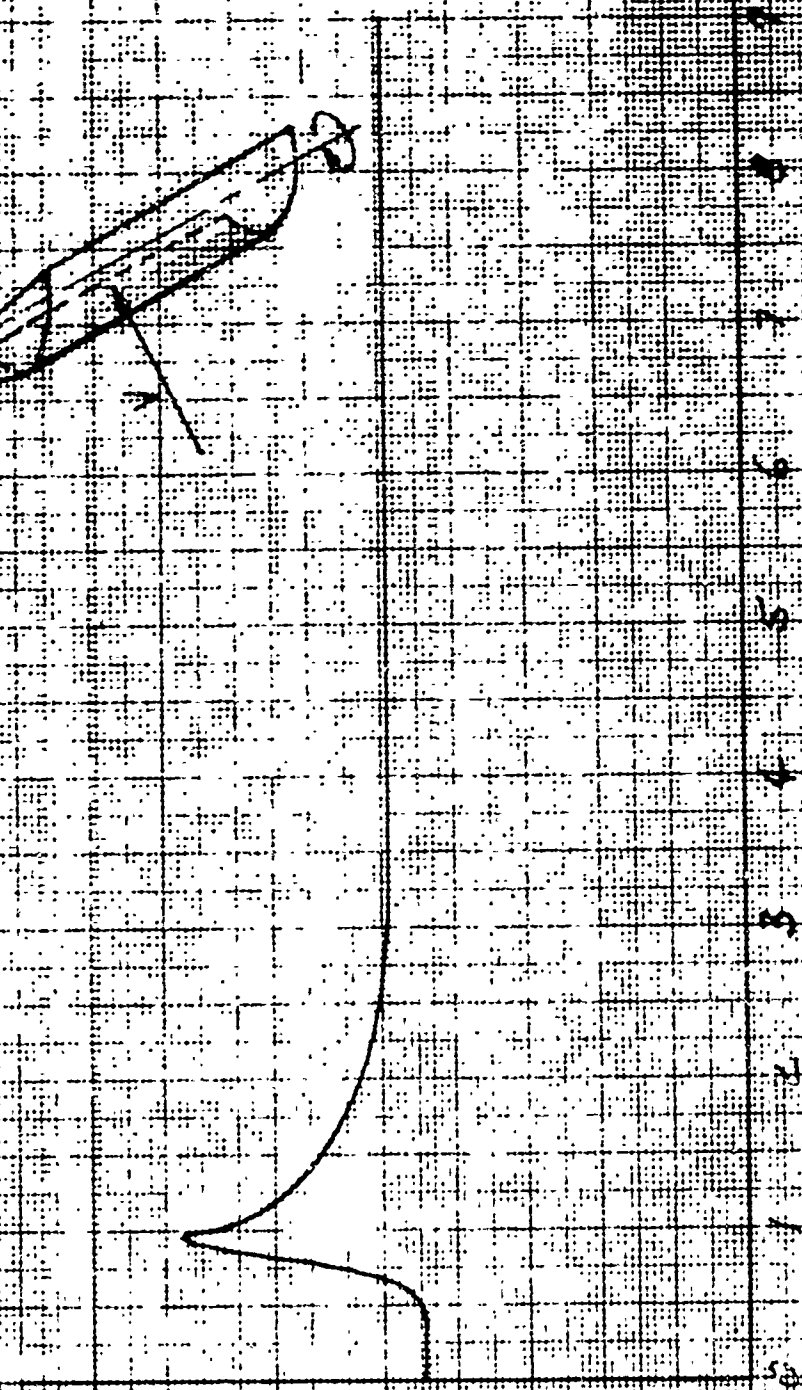
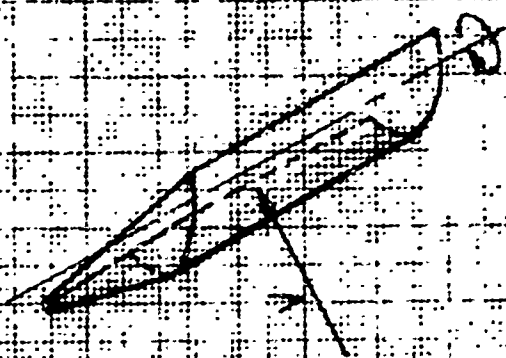


Figure 3-19. Heat Shield Half Reentry Drag Characteristics

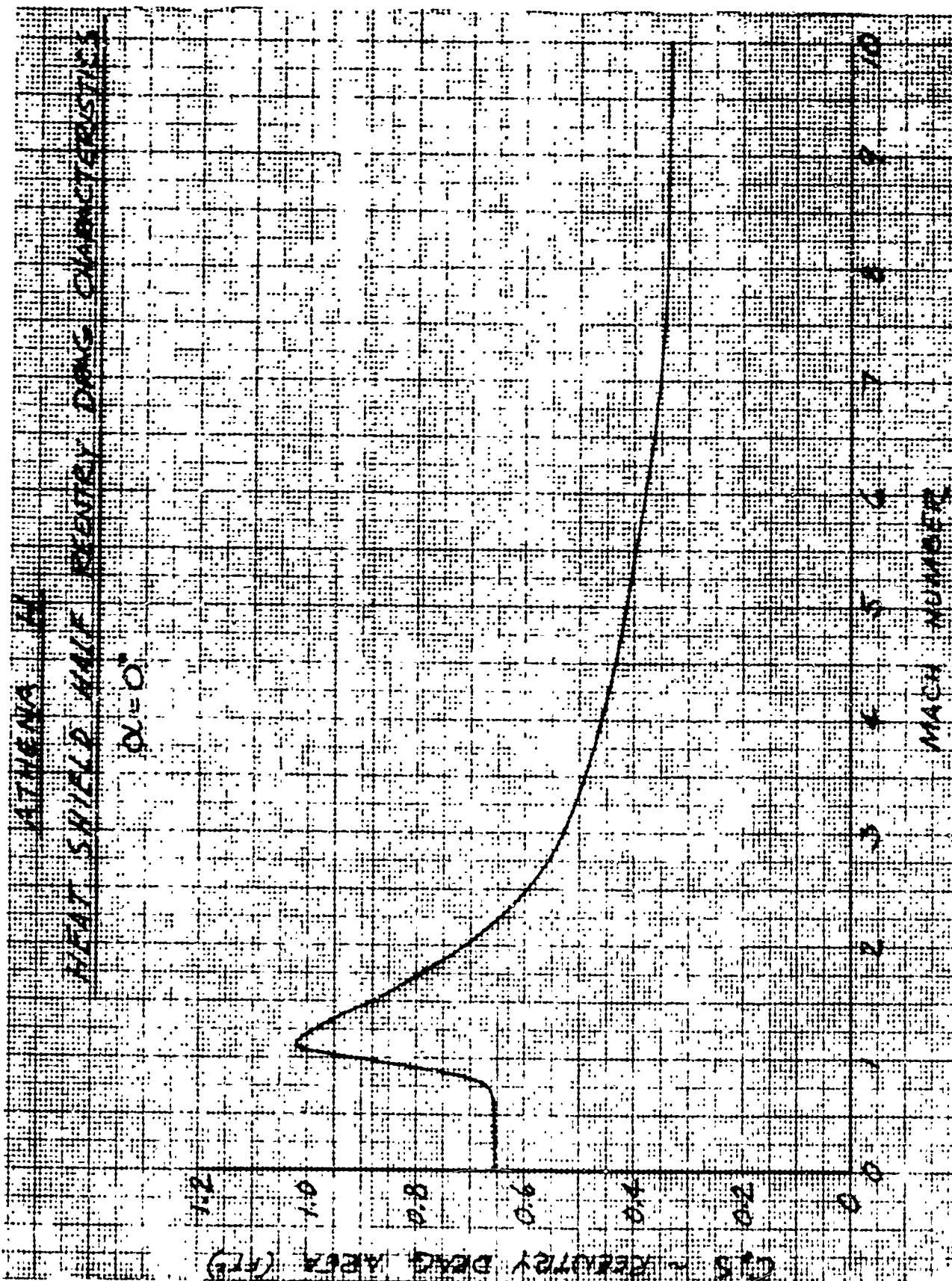


Figure 3-20. Heat Shield Half Reentry Drag Characteristics, $\alpha = 0^\circ$

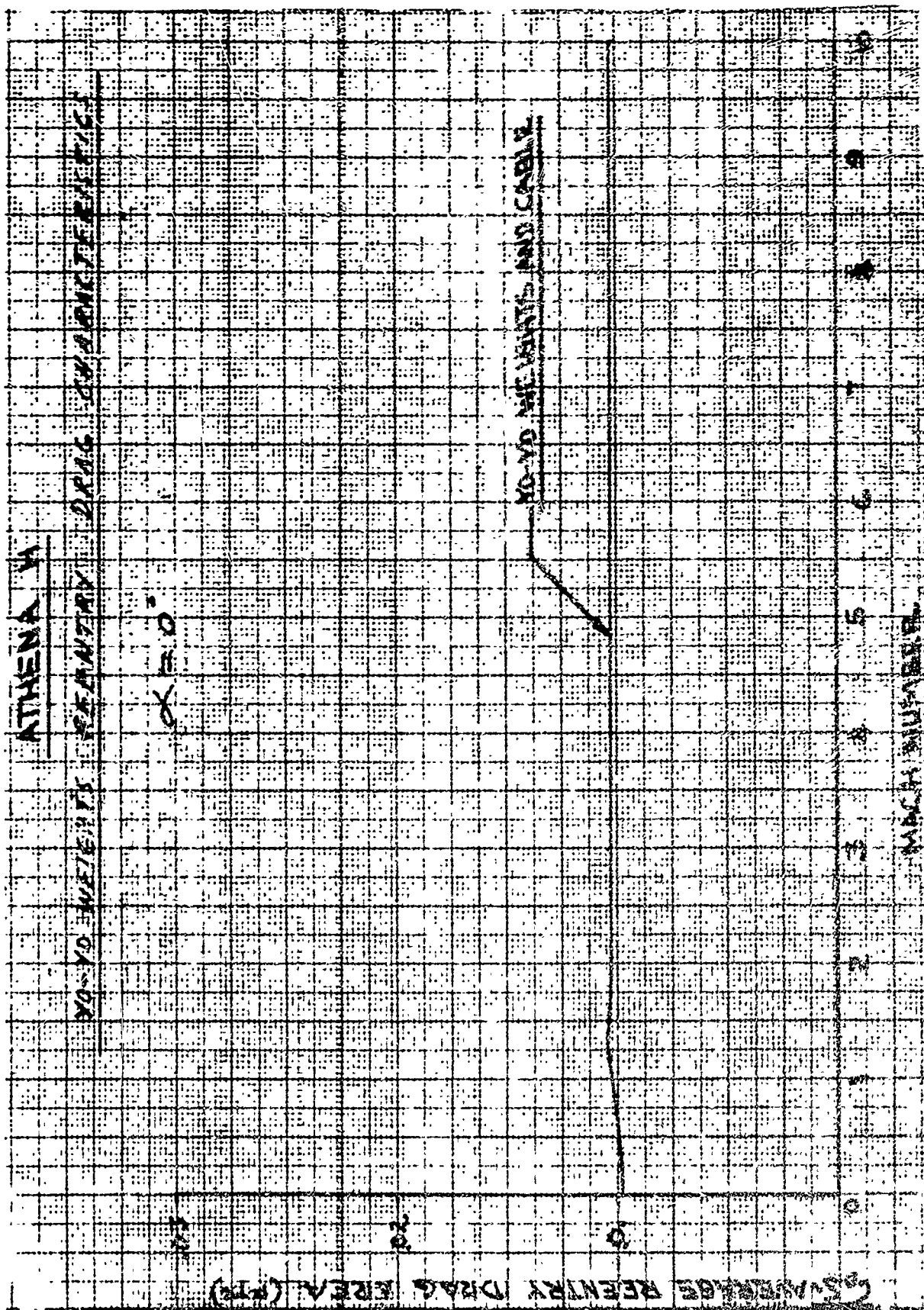


Figure 3-21. Yo-Yo Weights Reentry Drag Characteristics

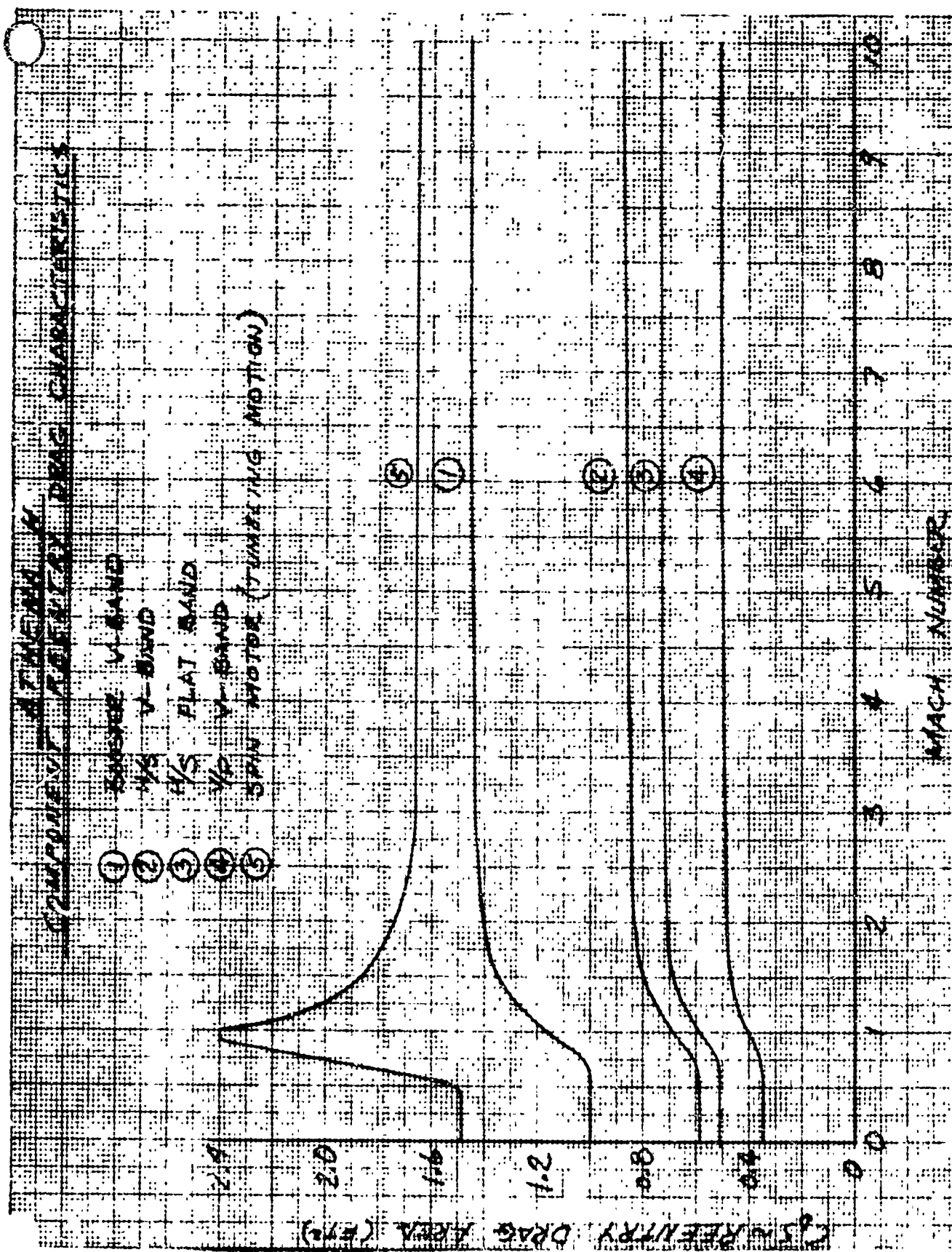


Figure 3-22. Component Reentry Drag Characteristics

0

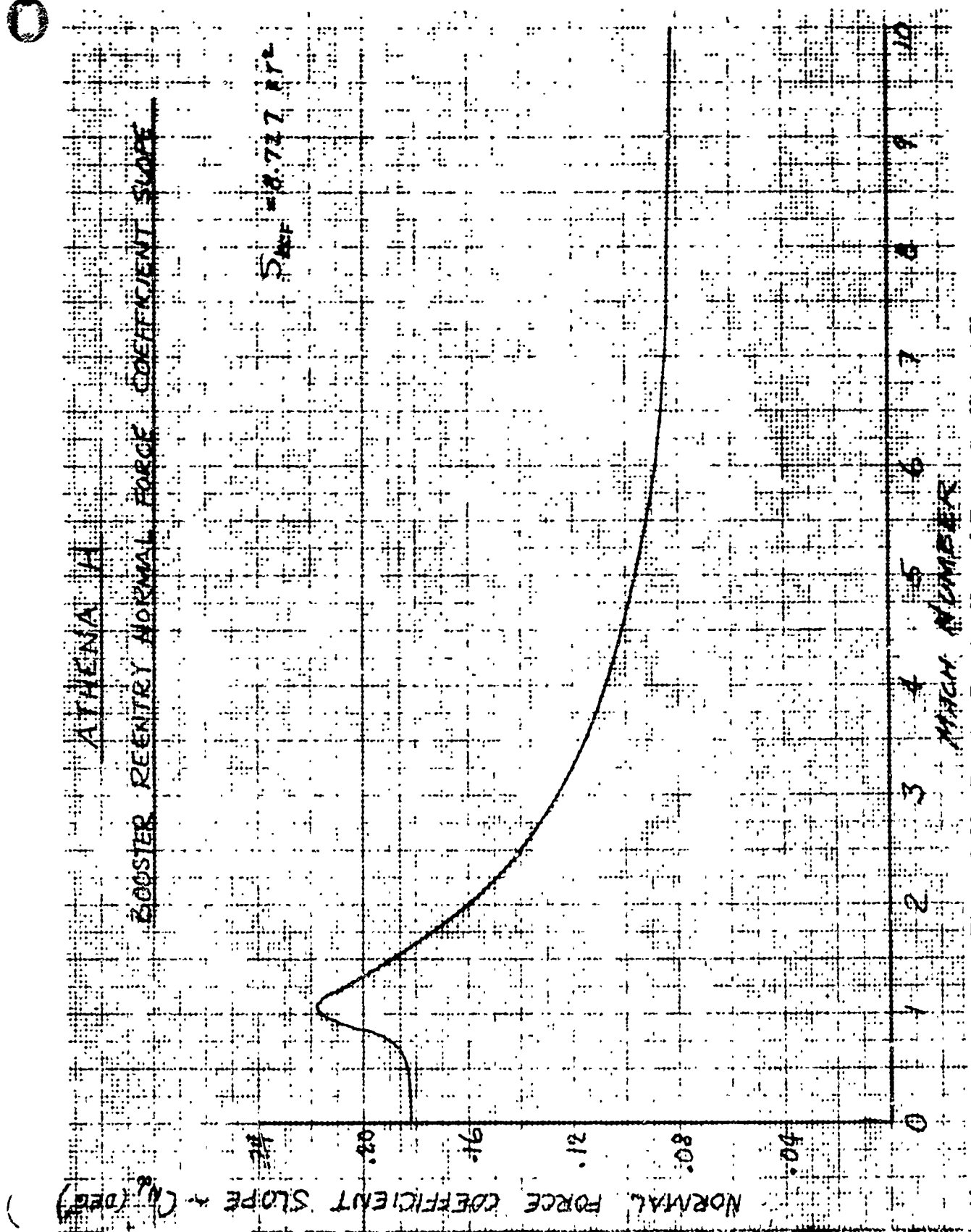


Figure 3-23. Booster Reentry Normal Force Coefficient Slope

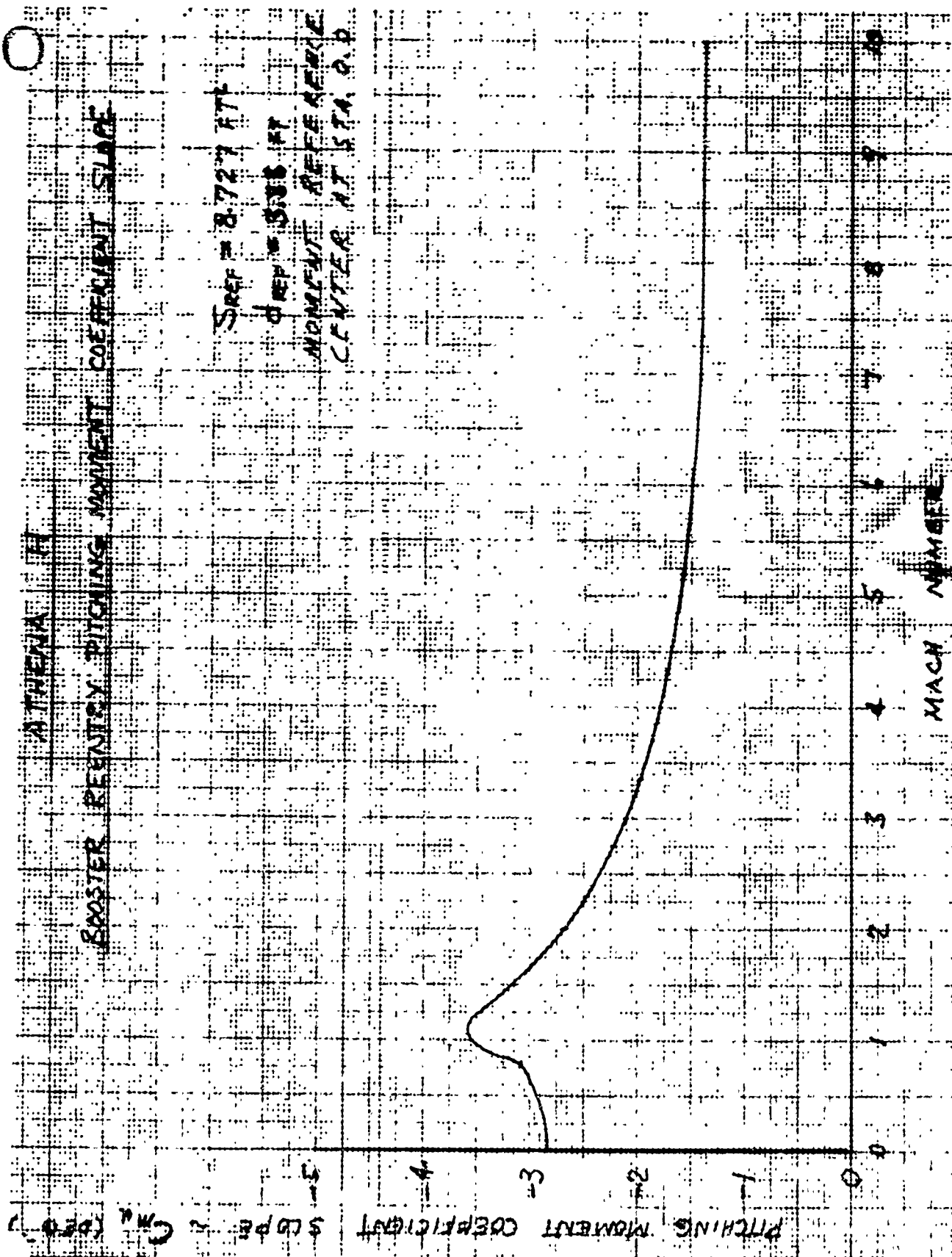


Figure 3-24. Booster Reentry Pitching Moment Coefficient Slope

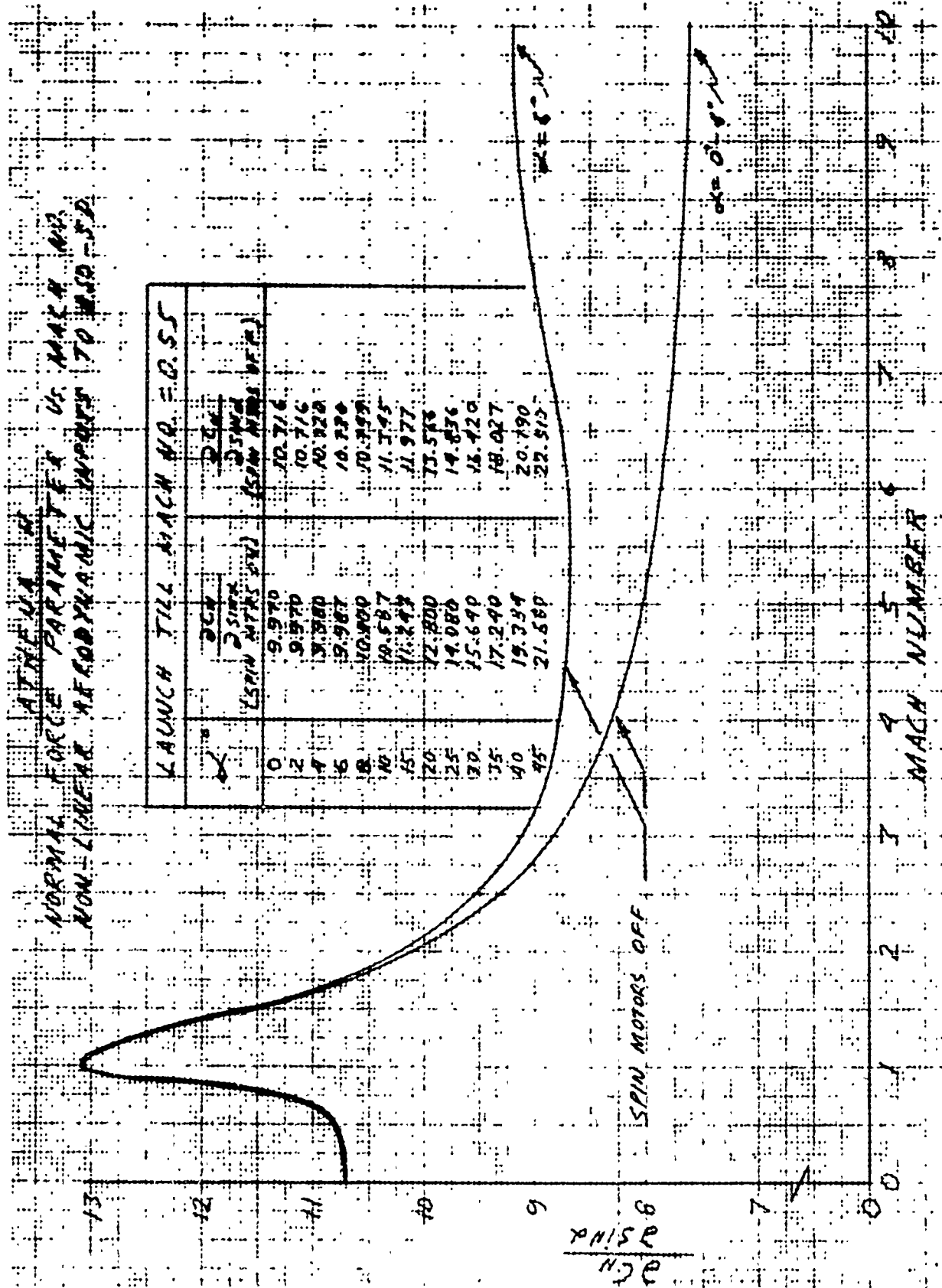


Figure 3-25. Normal Force Parameter versus Mach Number, Non-Linear Aerodynamic Inputs to ASD-5D

ATMOSPHERIC
CENTER OF PRESSURE VS. MACH NO.
NON-LINEAR AERODYNAMIC INPUTS TO ASD-5D

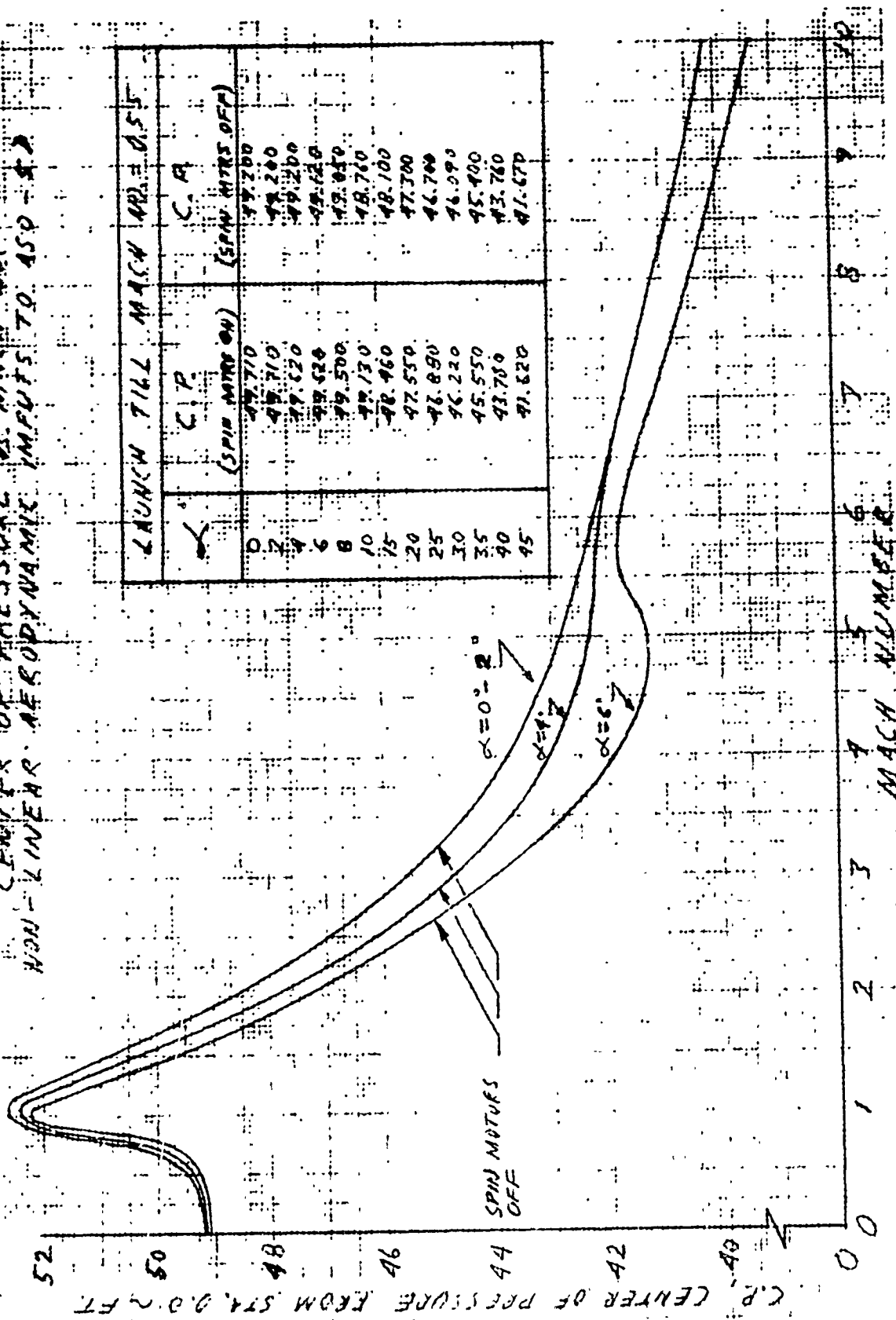


Figure 3-26. Center of Pressure versus Mach Number, Non-Linear Aerodynamic Inputs to ASD-5D

IV

AERODYNAMIC LOAD DISTRIBUTIONS

4.1 GENERAL

Aerodynamic loads for the ATHENA H are presented in Figures 4-1 through 4-9 and Table 4-1. Component data are presented for Mach numbers from 0 to 10 in Figures 4-1 through 4-4. Table 4-1 depicts appendages and components lift and drag characteristics for several Mach numbers. Figures 4-5 and 4-6 depict the variation of the normal force and axial force for the fin. Figure 4-7 shows the axial and normal force variation with Mach number for one tab. Figure 4-8 depicts the difference in aerodynamic pressure between the lower and upper fin surface along the fin chord, for several Mach numbers, while Figure 4-9 shows how this pressure difference decays along the span. The data herein was based on theoretical methods, and in most cases supported by the ATHENA H wind tunnel tests. These aerodynamic loads are presented to support structural analyses.

4.2 COMPONENT NORMAL FORCE SLOPE AND CENTER OF PRESSURE

Figures 4-1 through 4-4 include body component and fin component normal force coefficient slopes and centers of pressure. The components are the nose, nose afterbody, frustum, frustum afterbody, and the fins. It should be noted that the fin normal force coefficient slopes contain the fin/booster interference effects. The sum of these component normal force coefficients equal the total vehicle normal force coefficient slopes which had been based on wind tunnel test results from Reference 1.

4.3 APPENDAGE AERODYNAMIC LOADS

Table 4-1 tabulates normal force and drag characteristics for various vehicle appendages and protuberances. With the exception of the spin motor, which is ejected at Mach number of 0.5, these characteristics are shown for Mach numbers of 1.0 and 3.0, the critical loading conditions. The normal force characteristics some components are intentionally not shown in Table 4-1 since they are described in Section 4.2. The data in Table 4-1 were based upon wind tunnel data of Reference 1 with the exception of the data for the launch lugs, blade antenna, and payload pod, which were based on theoretical methods.

Figure 4-5 depicts the spanwise distribution of normal force coefficient slope over the fin for several Mach numbers. The distributions include body effects. When integrated, these distributions are compatible with the normal force coefficient slopes for the fins of Figure 4-2. Figure 4-6 presents the axial force as a function of Mach number for one fin, based on test results of Reference 1. Figure 4-7 depicts both the axial force and normal force as a function of Mach number for one roll tab. The axial and normal force directions are parallel and perpendicular to the vehicle longitudinal axes, respectively. These force characteristics were based upon the wind tunnel test data of Reference 2.

Figures 4-8 and 4-9 show the chordwise normal loading over the fin in terms of difference in aerodynamic pressure between the lower and upper surface. Figure 4-8 shows this chordwise pressure difference variation for Mach numbers of 1.0, 1.6, 3.0 and 7.0 at the fin root, semi-span station equal to 29 inches. Figure 4-9 shows how, due to the finite span, this loading decays along the increasing semi-span distance. The data in Figures 4-8 and 4-9 were computed analytically.

TABLE 4-1

APPENDAGES AND COMPONENT LIFT AND DRAG CHARACTERISTICS

COMPONENT	MACH NUMBER					
	0.5		1.0		3.0	
	$1/q \frac{dN}{d\alpha}$	$\frac{D}{q}$	$1/q \frac{dN}{d\alpha}$	$\frac{D}{q}$	$1/q \frac{dN}{d\alpha}$	$\frac{D}{q}$
	ft ² /deg	ft ²	ft ² /deg	ft ²	ft ² /deg	ft ²
Forward Launch Lug	--	--	0.00116	0.0461	0.000467	0.0526
Aft Launch Lug	--	--	0.00116	0.0461	0.000467	0.0526
Blade Antenna	--	--	0.00061	0.00129	0.000185	0.000735
Nose	--	--	--	0.697	--	0.639
Frustum	--	--	--	1.658	--	1.062
Spin Motor	0	2.20	--	--	--	--
One Fin	--	--	0.750	0.306	0.406	0.229
One Recruit Motor	--	--		0.500		0.370
a) Nose Fairing	--	--		0.279	--	0.206
b) Sleeve Fairing	--	--	--	0.221	--	0.164
One Payload Pod (20° Wedge-Box)	--	--	--	0.778	--	0.627

ATHENA H
COMPONENT NORMAL FORCE COEFFICIENT SLOPE
 REFERENCE AREA = 8.727 SQ FT

NORMAL FORCE COEFFICIENT SLOPE, $C_{N\alpha}$ (PER DEG)

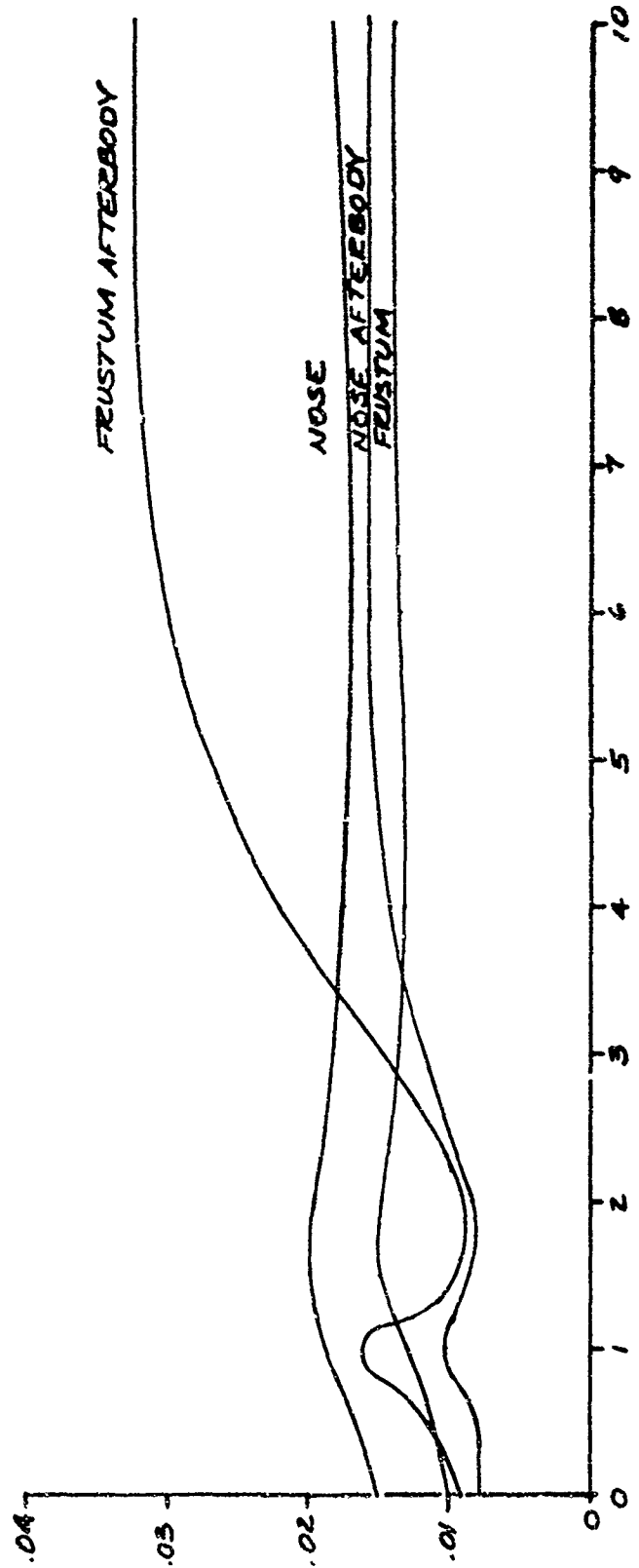
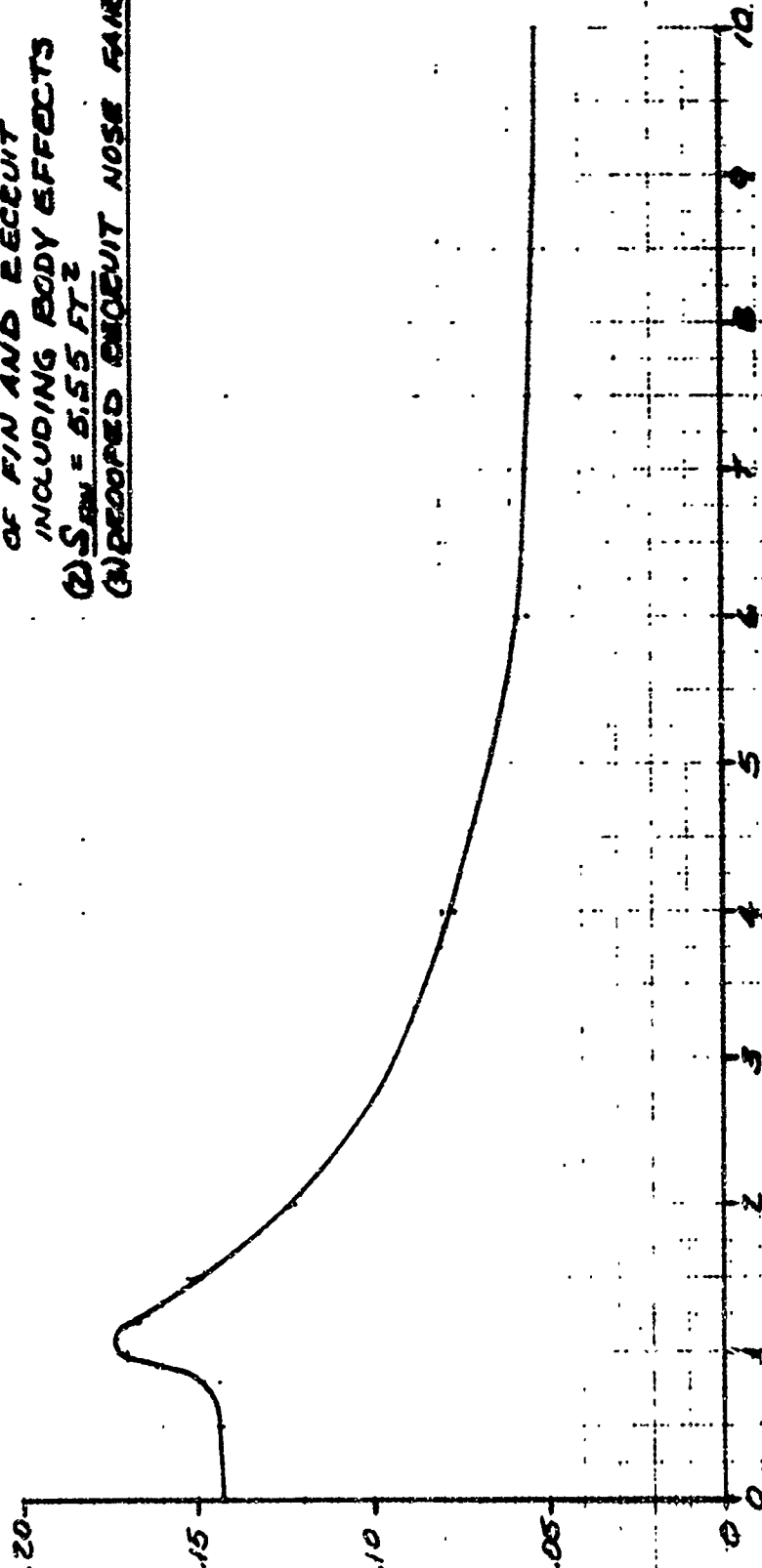


Figure 4-1. Component Normal Force Coefficient Slope

ATHENA H

FIN NORMAL FORCE COEFFICIENT SLOPE
REFERENCE AREA: 8.727 FT²

NORMAL FORCE COEFFICIENT SLOPE, $C_{N\alpha}$ (PER DEG)



NOTE: (1) NORMAL FORCE COEFFICIENT SLOPE IS THE COMBINATION OF FIN AND REEVEIT INCLUDING BODY EFFECTS
 (2) $S_{REF} = 8.55 \text{ FT}^2$
 (3) DECOUPLED REEVEIT NOSE FAIRING

MACH NUMBER, M

Figure 4-2. Fin Normal Force Coefficient Slope

ATHENA H
COMPONENT CENTER OF PRESSURE LOCATION
IN STATION NUMBERS

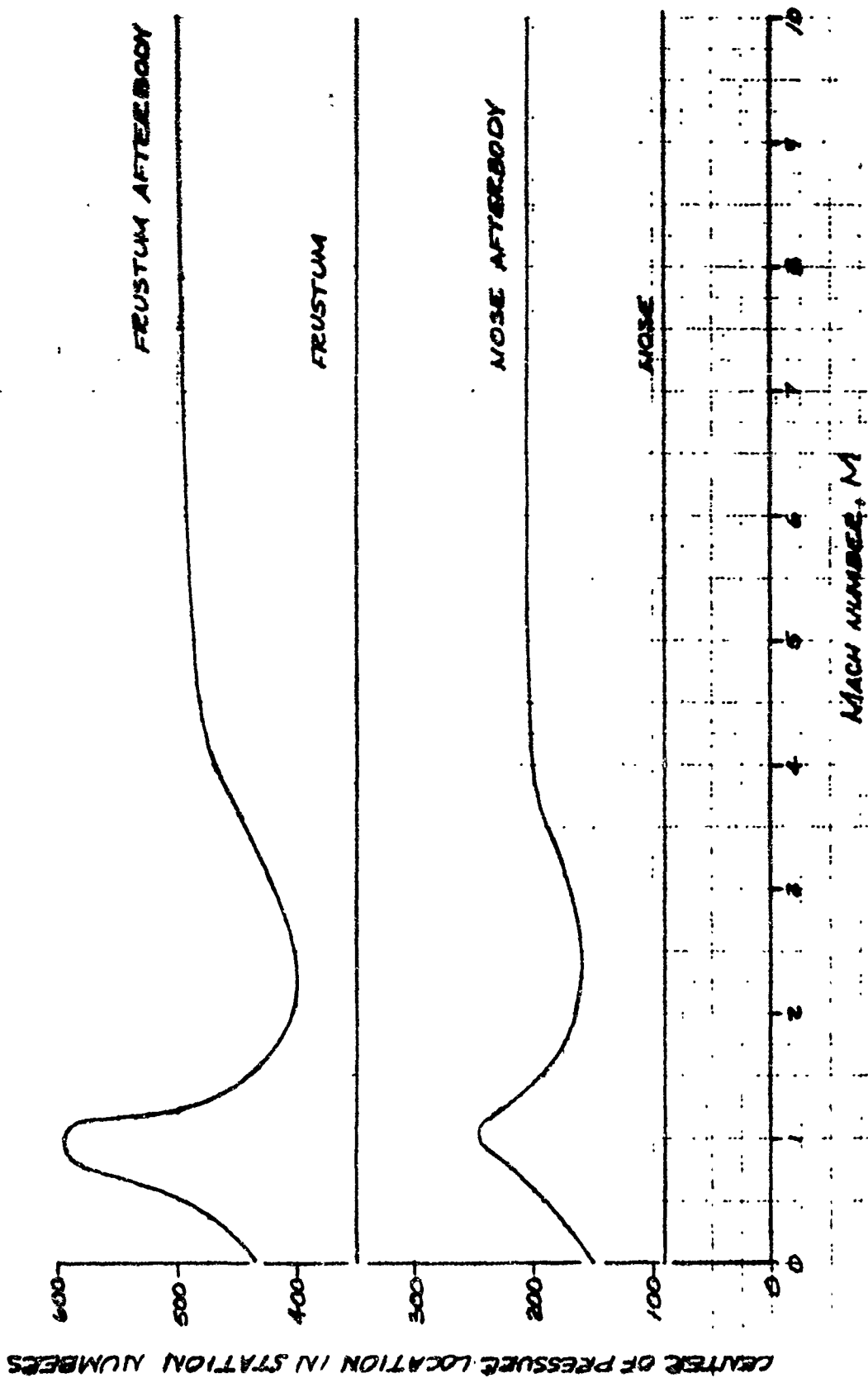


Figure 4-3. Component Center of Pressure Location in Station Numbers

ATHENA H
FIN CENTER OF PRESSURE LOCATION IN
STATION NUMBERS

NOTE: (1) CP LOCATION IS THAT OF
COMBINED FIN & RECRUIT
INCLUDING BODY EFFECTS
(2) $S_{FIN} = 5.55 \text{ FT}^2$
(3) DROOPED RECRUIT
NOSE FAIRING

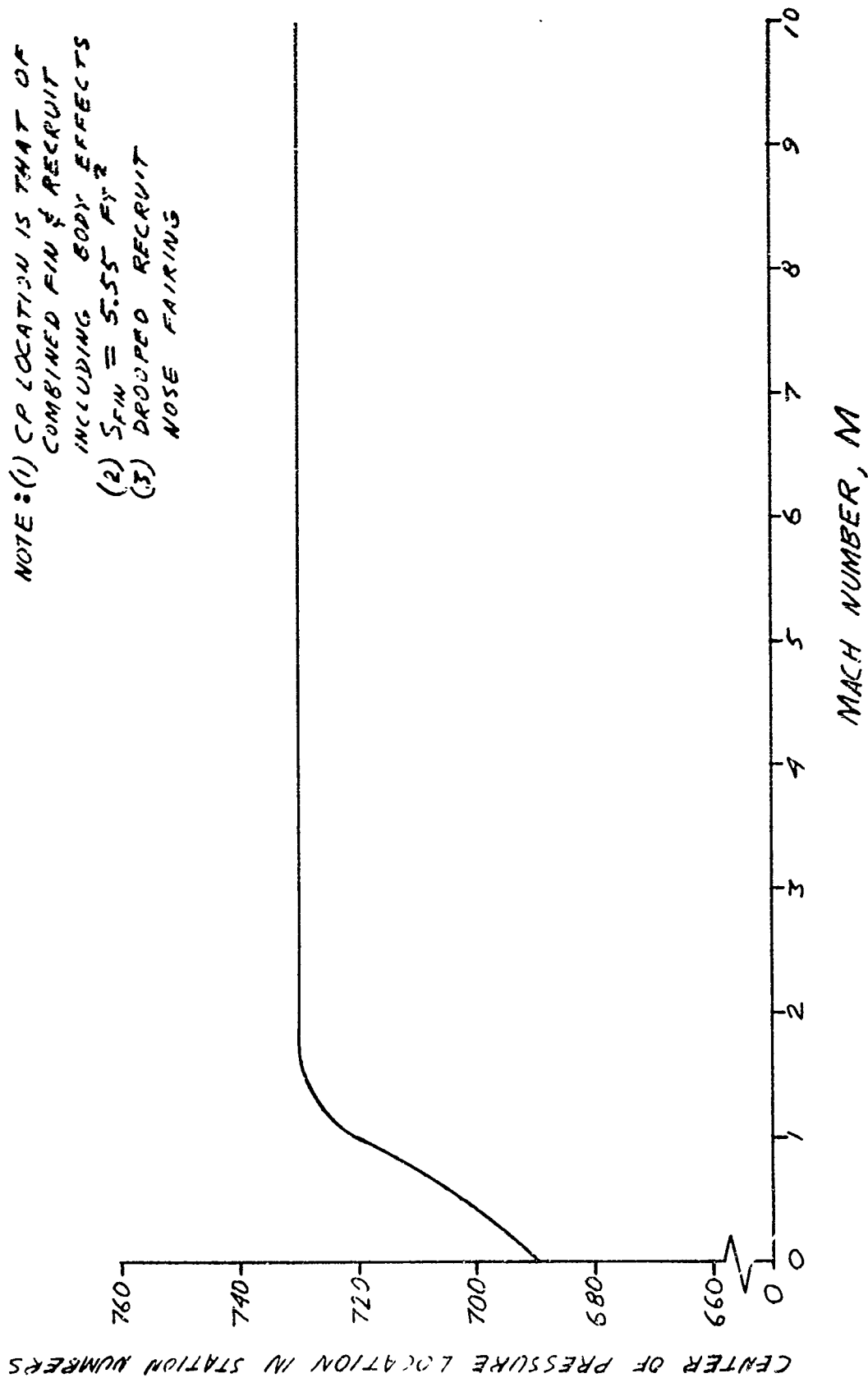


Figure 4-4. Fin Center of Pressure Location in Station Numbers

ATHENA H
FIN SPANWISE LOAD DISTRIBUTION
REFERENCE AREA = 8.727 FT²

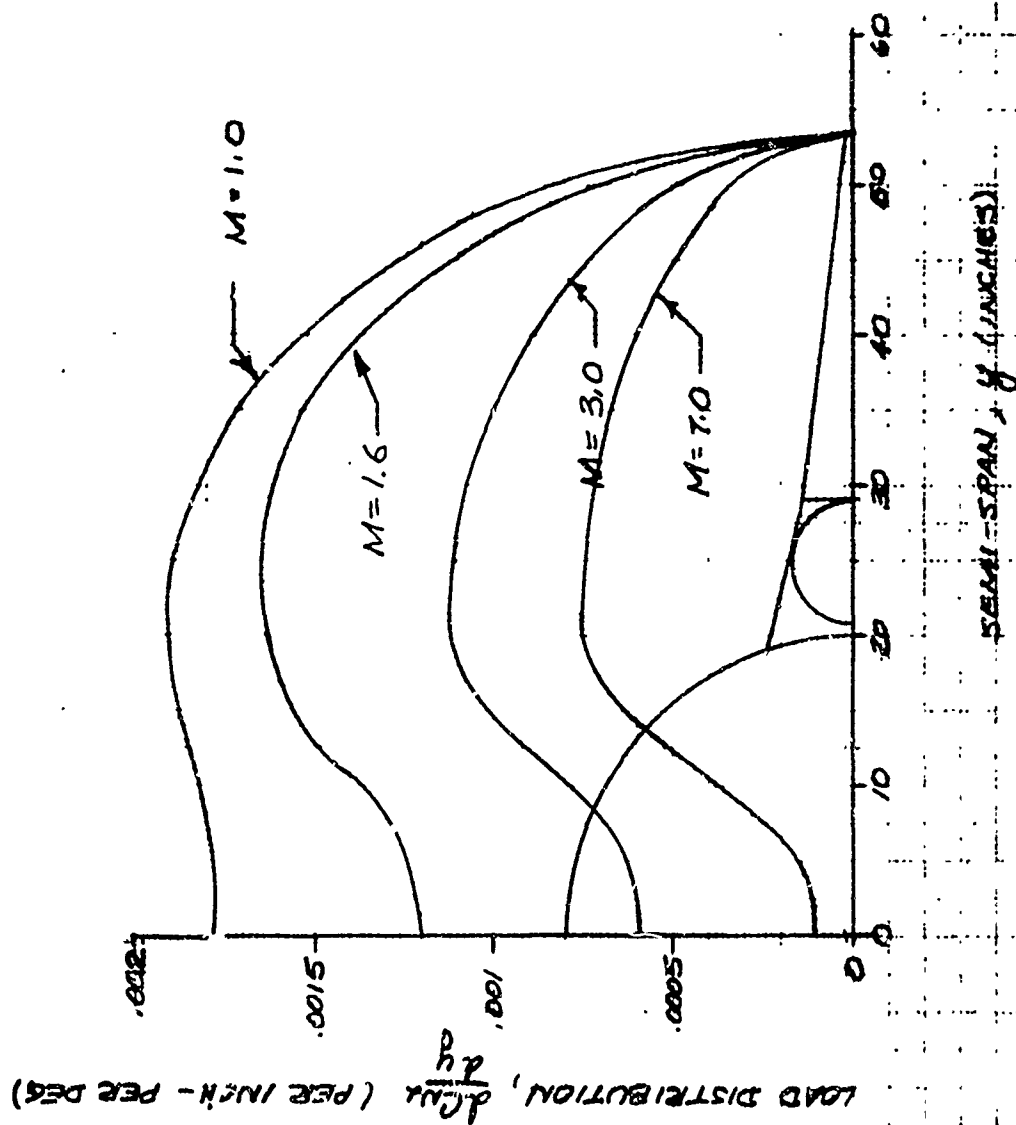


Figure 4-5. Fin Spanwise Load Distribution

II-34.36

ATHENA H

AXIAL FORCE PER UNIT DYNAMIC PRESSURE

ONE FIN W/O TAB

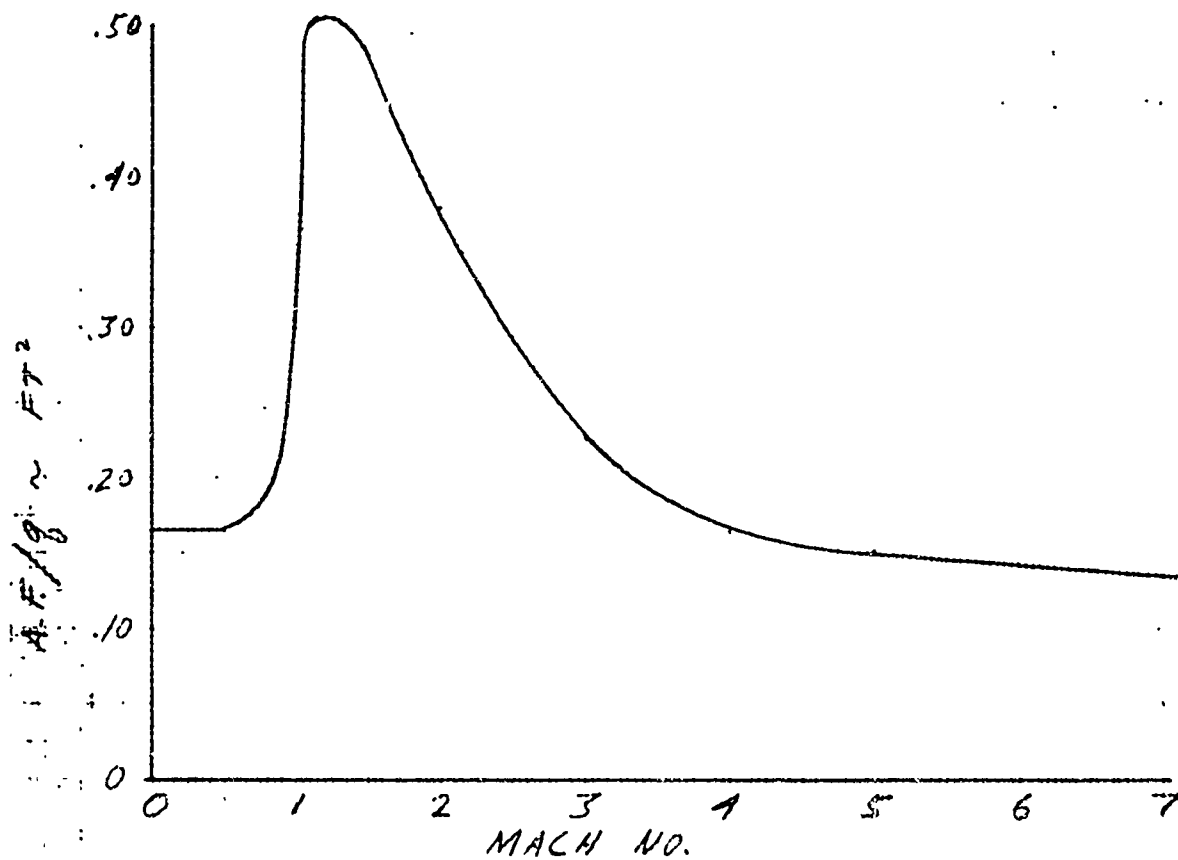


Figure 4-6. Axial Force Per Unit Dynamic Pressure, One Fin Without Tab

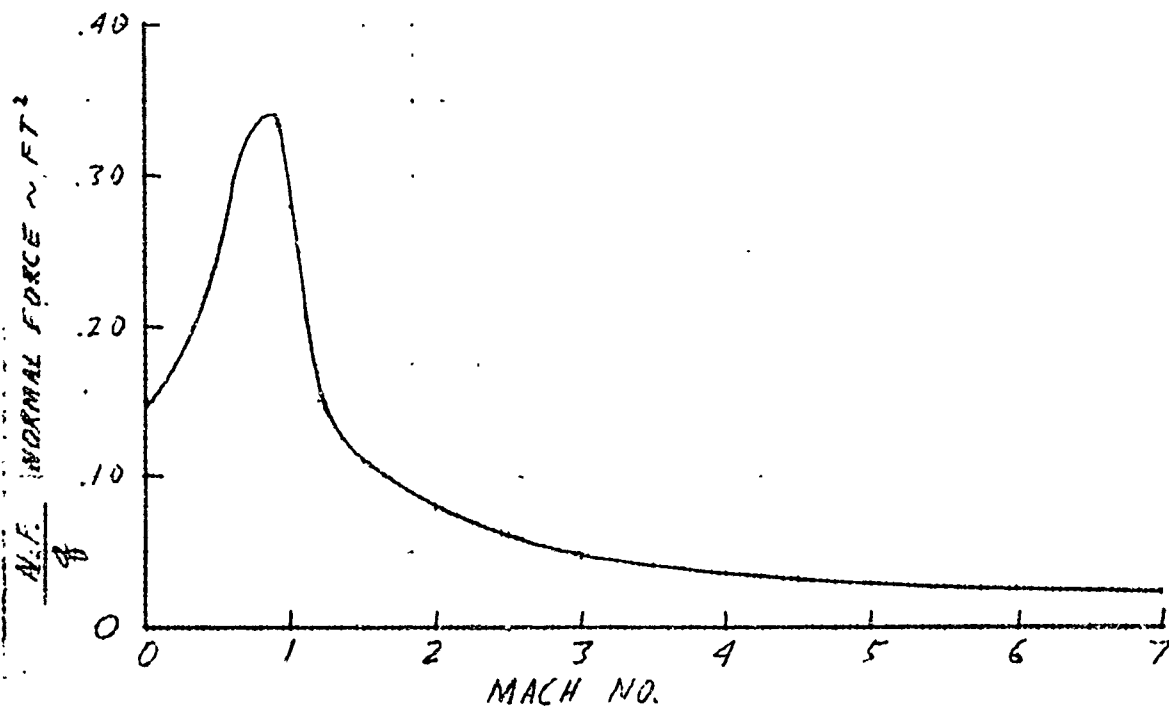
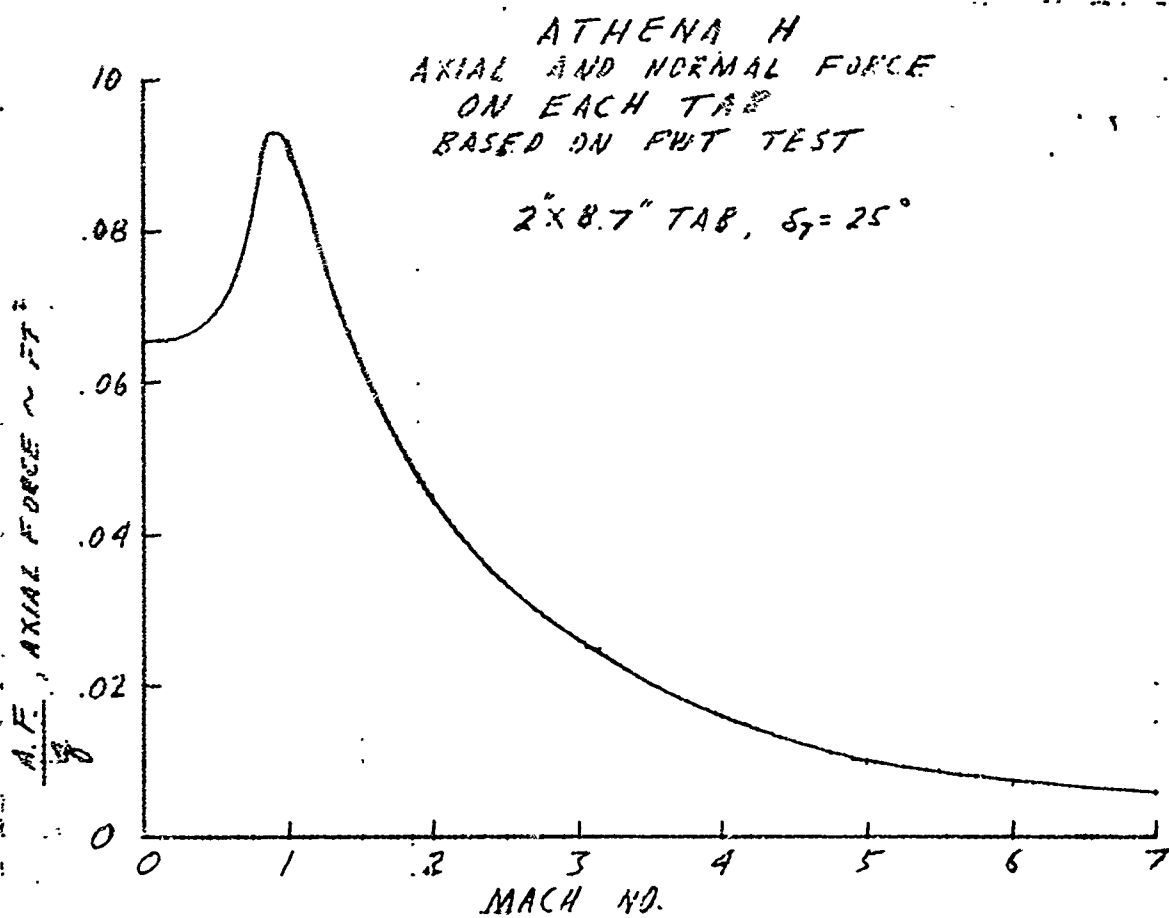


Figure 4-7. Axial and Normal Force on Each Tab Based on PWT Test

ATHENA H FIN CHORD-WISE LOADING

SEMI-SPAN STATION, $x = 29$ IN.

NOTE: TO OBTAIN LOAD MAGNITUDE AT ANY
SEMI-SPAN LOCATION, MULTIPLY THE
VALUES OF THIS PAGE BY THE SPAN-WISE
LOAD RATIO OF FIGURE 2.

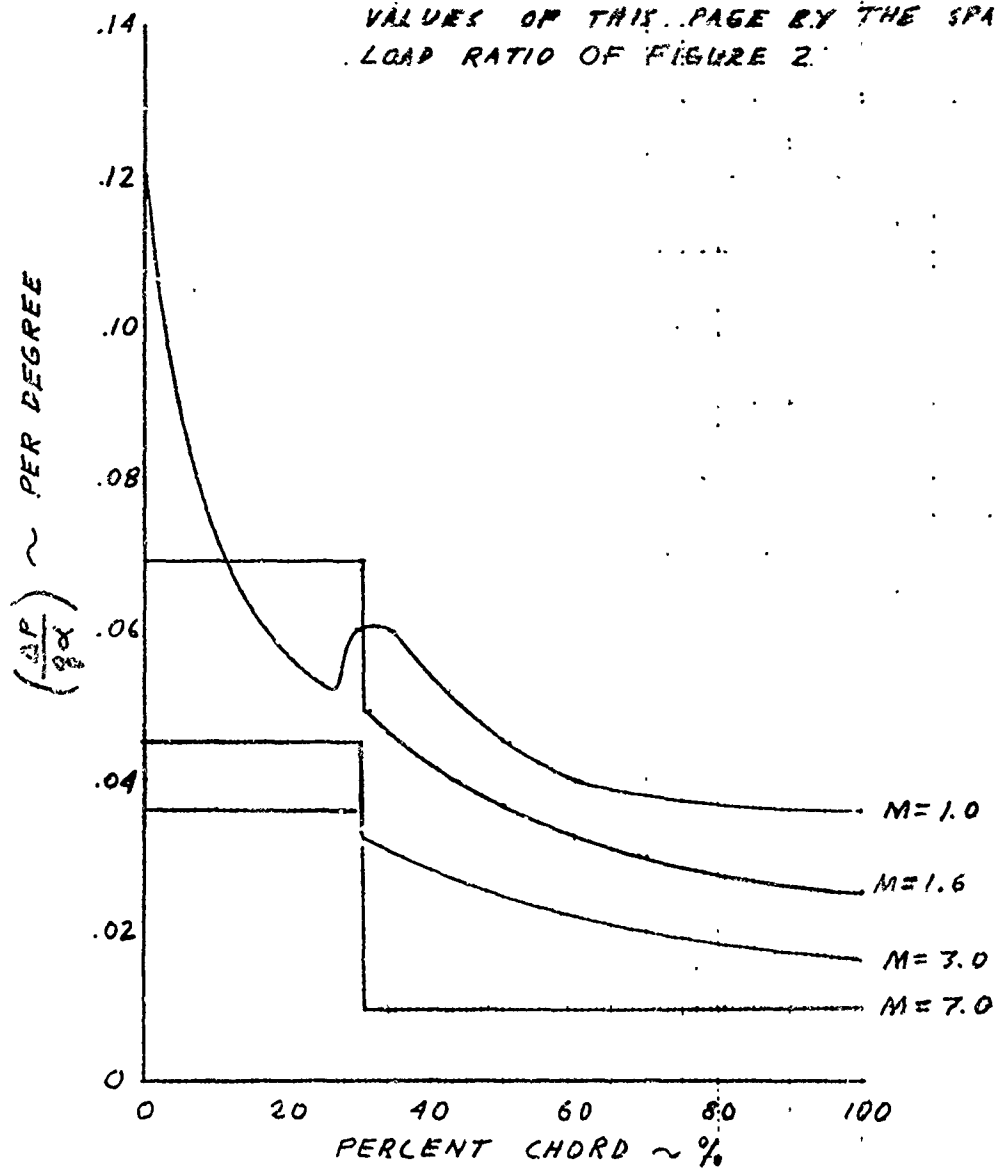


Figure 4-8. Fin Chord-Wise Loading

ATHENA H
RATIO OF SPAN-WISE TO ROOT LOADING
ON VEHICLE FIN

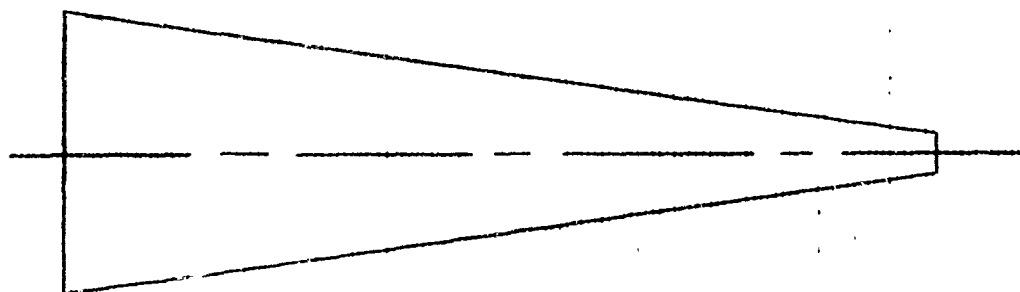
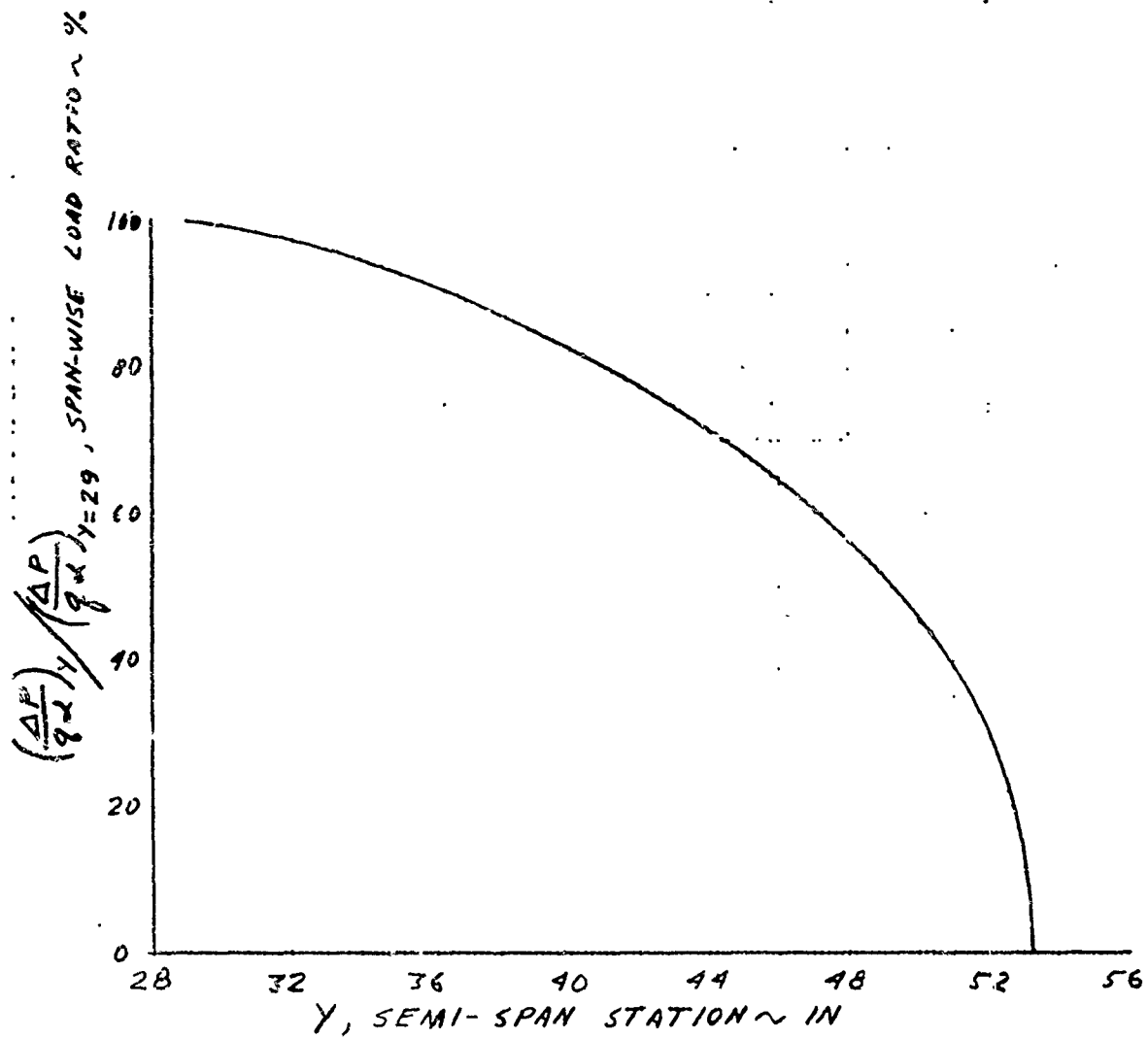


Figure 4-9. Ratio of Span-Wise to Root Loading on Vehicle Fin

V

EXTERNAL PRESSURE DISTRIBUTION

5.1 GENERAL

Figures 5-1 through 5-26 present the external pressure distribution over all the compartments to be vented during ascent flight. Figures 5-1 through 5-14 present zero angle of attack pressure coefficient distribution along the heat shield fairing, second stage shroud and interstage adapter for a wide range of Mach numbers. Figures 5-15 through 5-26 depict Mach number histories of external pressure over components to be vented. Table 5-1 describes the trajectories used to define these external pressure histories.

The external pressures for the trajectories using TD 123 motor data are slightly higher than for the trajectories using TD 115 motor data. However, since these external pressures are to be used in calculating skin differential pressures, the corresponding differences in internal pressures must also be taken into account when evaluating the effect of difference in external pressure. In the venting analysis, Reference 5, it was found that the internal pressure history using TD 123 motor data changed in such a manner that the resulting skin differential pressures were very similar to those obtained with TD 115 motor data. Therefore, the skin differential pressures obtained from the external pressures provided herein and the internal pressures obtained from Reference 4 can be considered as applying to the trajectories using TD 123 motor data.

Presented pressures were based on theoretical methods, wind tunnel results for components of similar geometry, and wind tunnel tests on the full scale ATHENA H aft section.

5.2 VEHICLE PRESSURE DISTRIBUTION

Figures 5-1 through 5-14 present the external pressure distribution in coefficient form, for the section of the ascent configuration that is forward of the first stage. The coefficients, along the vehicle length, are presented for zero angle of attack and for a Mach number range of Mach = 0.169 through 6.0. These pressure coefficients have been computed by theoretical methods as well as using results of pressure measurements on numerous similar shaped missile configurations available in literature.

It is not expected that an angle of attack greater than three degrees will be experienced during flight. Through the investigation of numerous test results, it was observed that a variation in angle of attack of three degrees did not affect the windward or leeward external pressure by more than 0.5 pounds per square inch. Therefore, to derive the external minimum of maximum external pressures for the shown pressure coefficient, C_p , a known dynamic pressure q_∞ and ambient pressure, P_∞ , it is recommended to use the following expressions:

$$P_{\min} = \frac{C_p q_\infty}{144} + P_\infty - 0.5 \sim \text{psia}$$

$$P_{\max} = \frac{C_p q_\infty}{144} + P_\infty + 0.5 \sim \text{psia}$$

The dynamic pressure and ambient pressure are trajectory-dependent.

5.3 COMPONENT PRESSURE DISTRIBUTION

The component pressures shown in Figures 5-15 through 5-27 are absolute pressures and reflect the Castor IV design trajectories, since these were critical for the venting analyses of Reference 4. These trajectories are described in Table 5-1. Each figure identifies whether the external pressures are to be used for collapsing or bursting differential skin pressures which will be referred to as either collapsing or bursting ΔP 's in this document.

5.3.1 Raceway

Figure 5-15 presents the external pressure variation on the raceway nose. The pressure is shown for several angles along the nose as a function of Mach number. The solid line curves are for collapsing ΔP 's; the dashed line curve is for bursting ΔP since it represents the minimum pressure on the raceway nose section. These pressures are for the Castor IV trajectories.

Minimum and maximum external pressure over the flat center portion of the raceway is shown in Figure 5-16. They are for computing collapsing and bursting pressures.

Figure 5-17 depicts external pressure over the last six inches of the flat raceway portion. This pressure corresponds to the plateau pressure due to shock stand-off in front of the second stage shroud. Six inches corresponds to the maximum calculated shock stand-off.

5.3.2 Recruit Nose

Figure 5-18 presents external pressure for the droop-nose recruit. The pressure is to be used for collapsing ΔP 's and applies to Castor IV low angle trajectory. For bursting ΔP 's, assume the external pressure to be zero.

5.3.3 Aft Recruit Fairing

The aft Recruit fairing pressures over the semi-circular segment of the fairing are shown in Figure 5-19. This segment is the most forward portion of the Recruit fairing and lies directly beneath the Recruit motor. It is oriented so that the semi-circular side faces into the flight direction and sees ram air. Figure 5-19 presented the external pressure versus Mach number. The pressure is shown for several angles, ψ , where $\psi = 0$ degrees corresponds to the maximum incidence and $\psi = 90$ degrees corresponds to zero incidence angle. These pressures are to be used for collapsing ΔP .

In addition to the semi-circular segment, another relatively high pressure section on the aft Recruit fairing exists. This section approximates a semi-conical surface where the cone semi-vertex angle is 11 degrees. This section was assumed to be at an angle of attack of 3° and the resulting external pressure was then to be applied over the aft Recruit fairing, excluding the circular section. Figure 5-20 shows the external pressure variation over the non-circular segment of the aft Recruit fairing. The curve is based on analytical methods, including estimates of pressure effects due to presence of certain auxiliary payload shapes. The pressure values in this figure exceed the maximum pressures measured with a 25 degree wedge-box auxiliary pod in Reference 2. These pressures should be used for computing collapsing ΔP .

5.3.4 Shroud and Pylons

Figure 5-21 depicts the Mach number history of the external pressure on the booster shroud in the high pressure area of the launch lugs. This area extends a few inches around the lugs. Figure 5-21 also shows the pressure variation on the pylons. Both curves were based on theoretical predictions which were conservative and show higher pressures than test values of Reference 2. These pressures are to be used to compute collapsing ΔP .

Figure 5-22 depicts the Mach number history of the external pressure on the booster shroud behind the high pressure region of the launch lugs. This region experiences lower pressure and extends from just aft of the launch lug up to the shroud aft plane. This data was based on test data of Reference 2 and represent the maximum pressures measured with either payload pod or launch lugs attached. This pressure is to be used for computing collapsing ΔP .

5.3.5 Booster Shroud Aft Seal

A conservative estimate of the maximum external pressure acting on the shroud seal ring was made by calculating the pressure at the plume boundary, taking into account the effect of the external stream on the plume, and assuming that this pressure acts on the ring. The procedure was as follows:

- (1) The initial turning angle of the plume was calculated as a function of the plume boundary pressure, over a range of chamber pressures.
- (2) The pressure at the surface of a cone (with a semi-vertex angle equivalent to the plume turning angle) impinged upon by the external stream was calculated over a range of Mach numbers.
- (3) The pressure at the plume boundary, for a given chamber pressure and free-stream Mach number was then obtained from a cross plot of (1) and (2). This plot is shown in Figure 5-23 and is to be used for computing collapsing P .

5.3.6 Minimum Pressure on Booster Shroud Structure

Figure 5-24 presents the minimum external pressure over the aft Recruit fairing shroud, and pylons. It is to be used for computing the bursting ΔP . It represents a base pressure coefficient reduced by 25 percent.

5.3.7 Fin

Figure 5-25 depicts the fin leading edge external pressure. It represents the theoretical prediction on the windward side, at 3 degrees angle of attack, of the leading edge. It is to be used for computing the collapsing ΔP .

The external pressures on the fin forward and aft side panels are presented in Figure 5-26 and account for the presence of a 20 degree wedge-box auxiliary payload pod. The pressures for these panels were evaluated to support a considerable amount of venting analysis of Reference 3 on those parts of the fin. The forward side panel is located near the leading edge, along the fin root section and is of rectangular shape 7.5 inches by 14.85 inches in size. The aft side panel is near the trailing edge of the fin, is 7.5 inches outboard of the fin root, and is of rectangular shape, 8.4 inches by 12.4 inches in size. The pressures in Figure 5-26 represent the maximum pressure

data of Reference 2, of tests with a 25 degree wedge-box payload pod attached. This data was reduced to reflect a 20 degree wedge-box payload pod since the 20° angle has been selected because of its lower induced pressure on surrounding structure. This pressure is to be used for computing collapsing ΔP .

Figure 5-27 also shows external pressure on the fin side panels, but here the pressures were based on test measurements of Reference 2 without the auxiliary payload pod. Instead of pods launch lugs were attached to the model. The resulting pressures are lower than in the preceding figure. These pressures are to be used to compute collapsing ΔP .

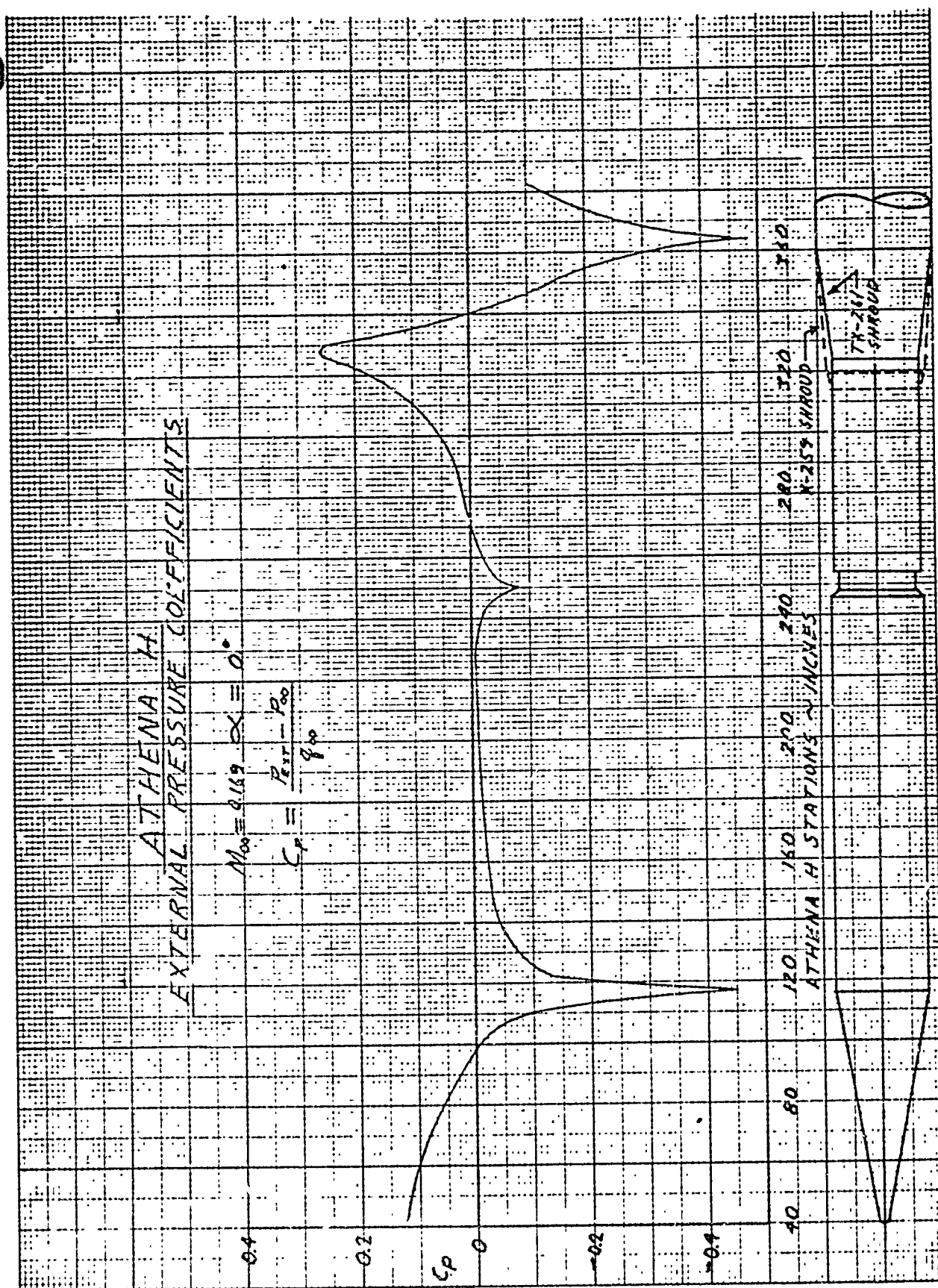


Figure 5-1. External Pressure Coefficient Distribution, $M_{\infty} = 0.169$, $\alpha = 0$

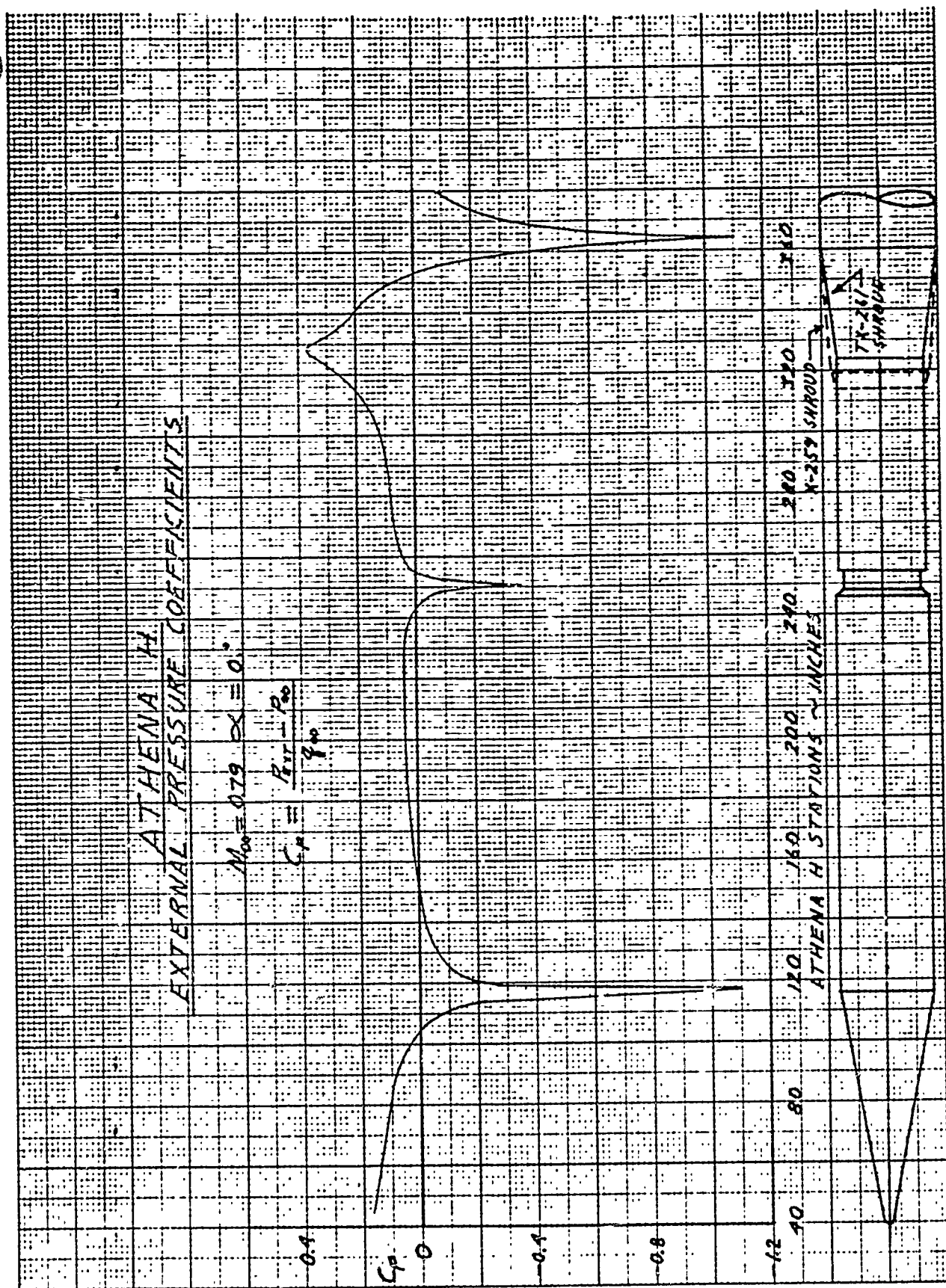


Figure 5-2. External Pressure Coefficient Distribution, $M_{\infty} = 0.79 \alpha = 0$

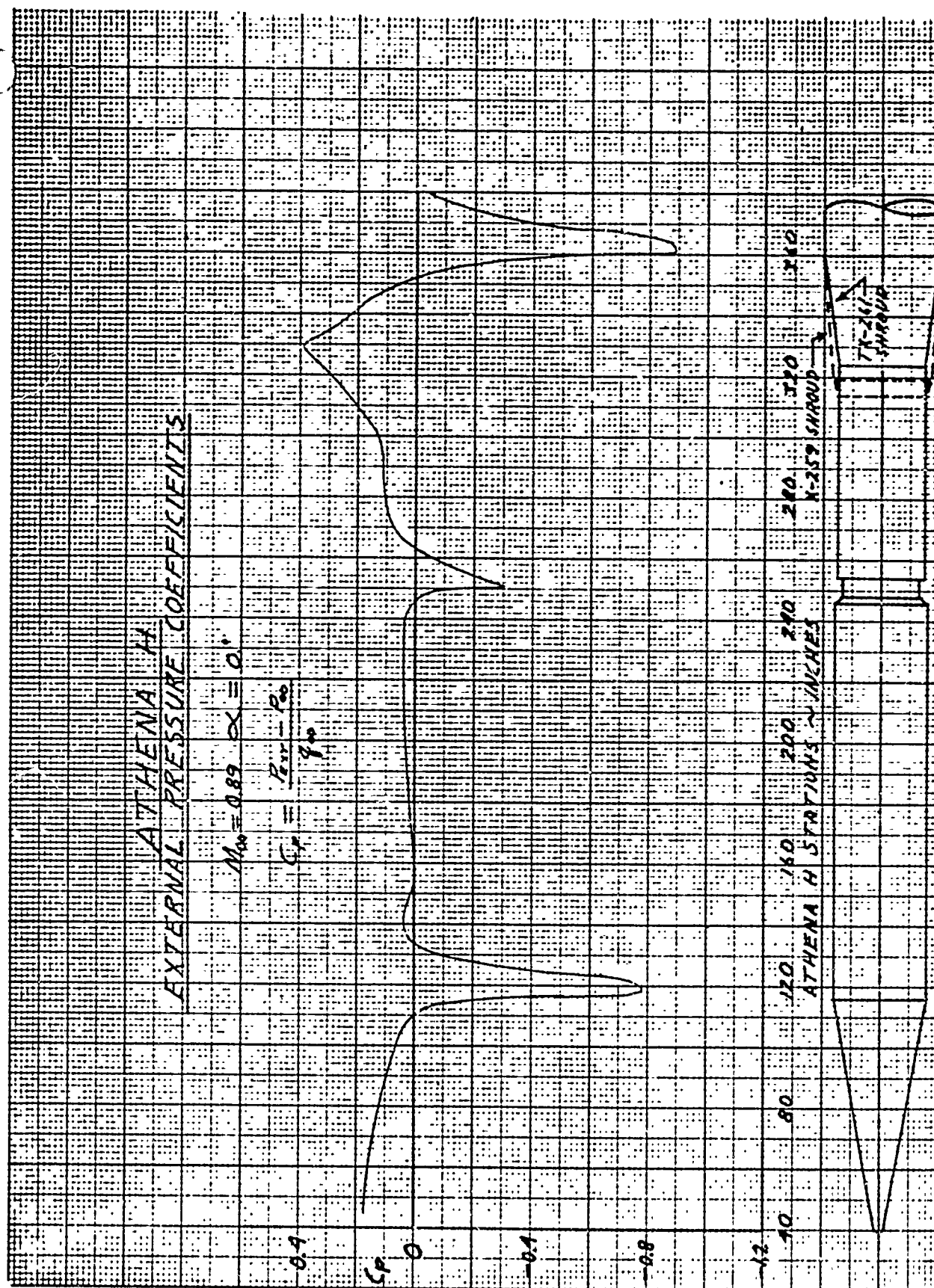


Figure 5-3. External Pressure Coefficient Distribution, $M_\infty = 0.89 \quad \alpha = 0$

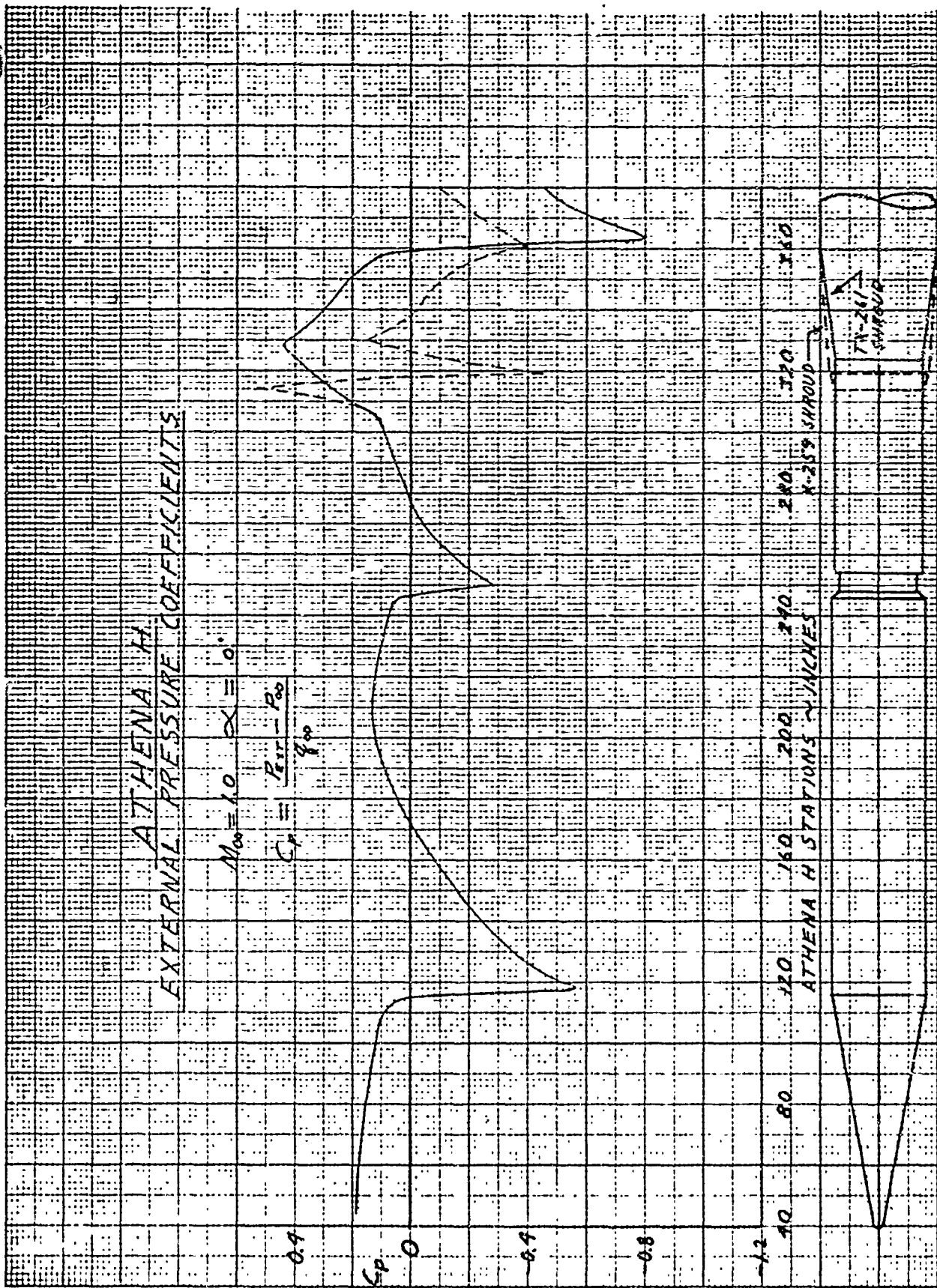


Figure 5-4. External Pressure Coefficient Distribution, $M_\infty = 1.0 \alpha = 0$

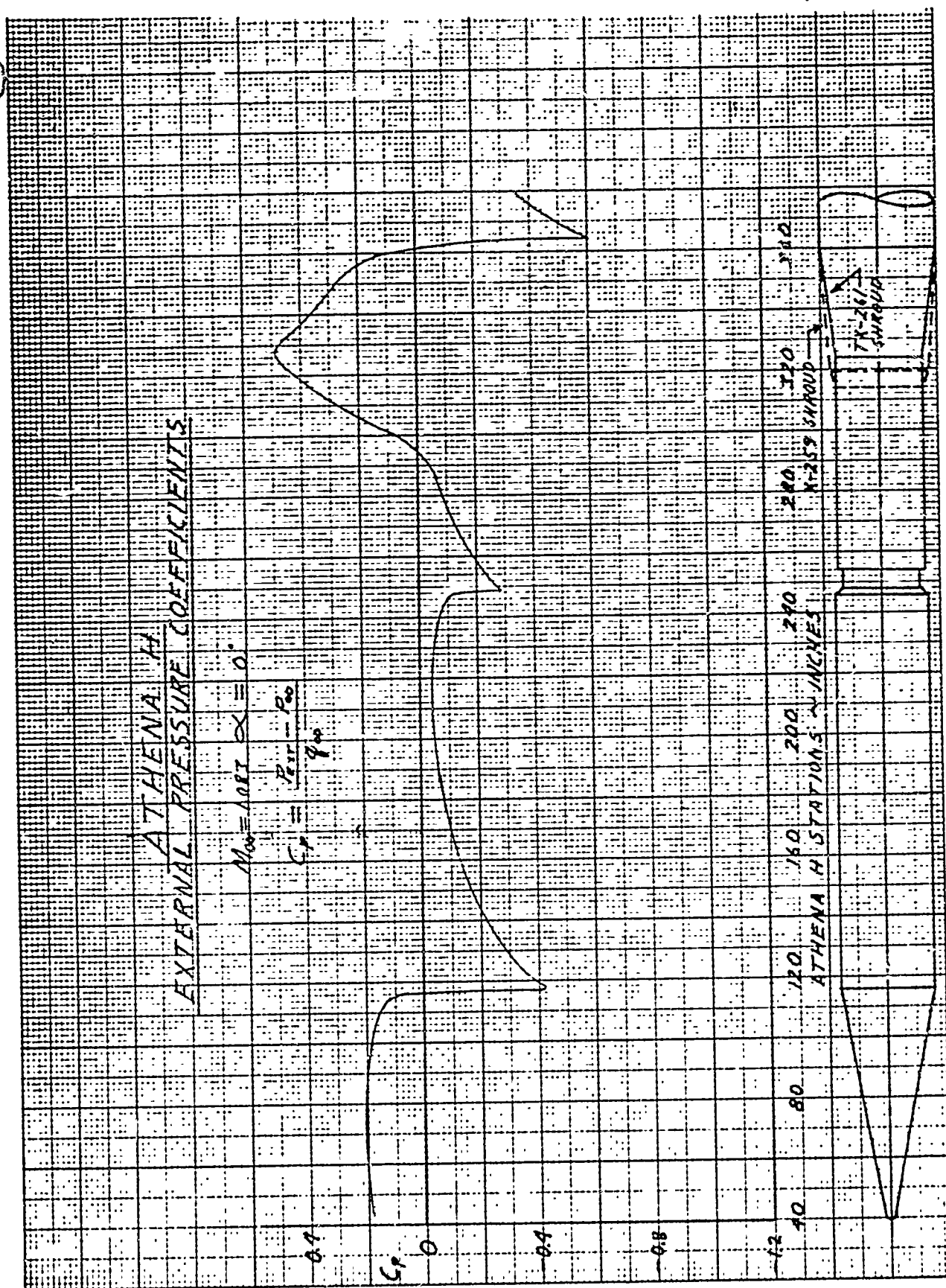


Figure 5-5. External Pressure Coefficient Distribution, $M_{\infty} = 1.083 \quad \alpha = 0$

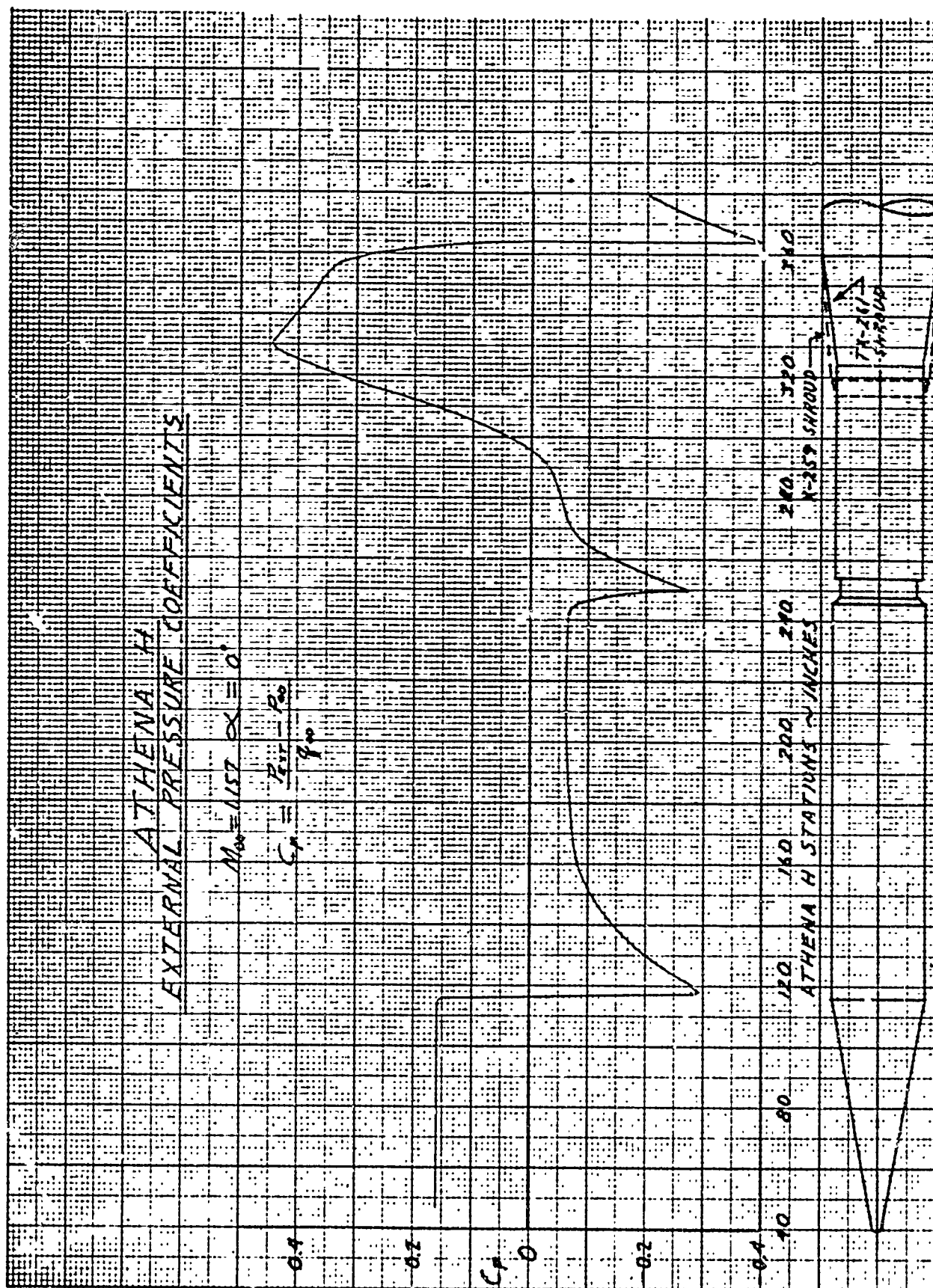


Figure 5-6. External Pressure Coefficient Distribution, $M_{\infty} = 1.157 \alpha = 0$

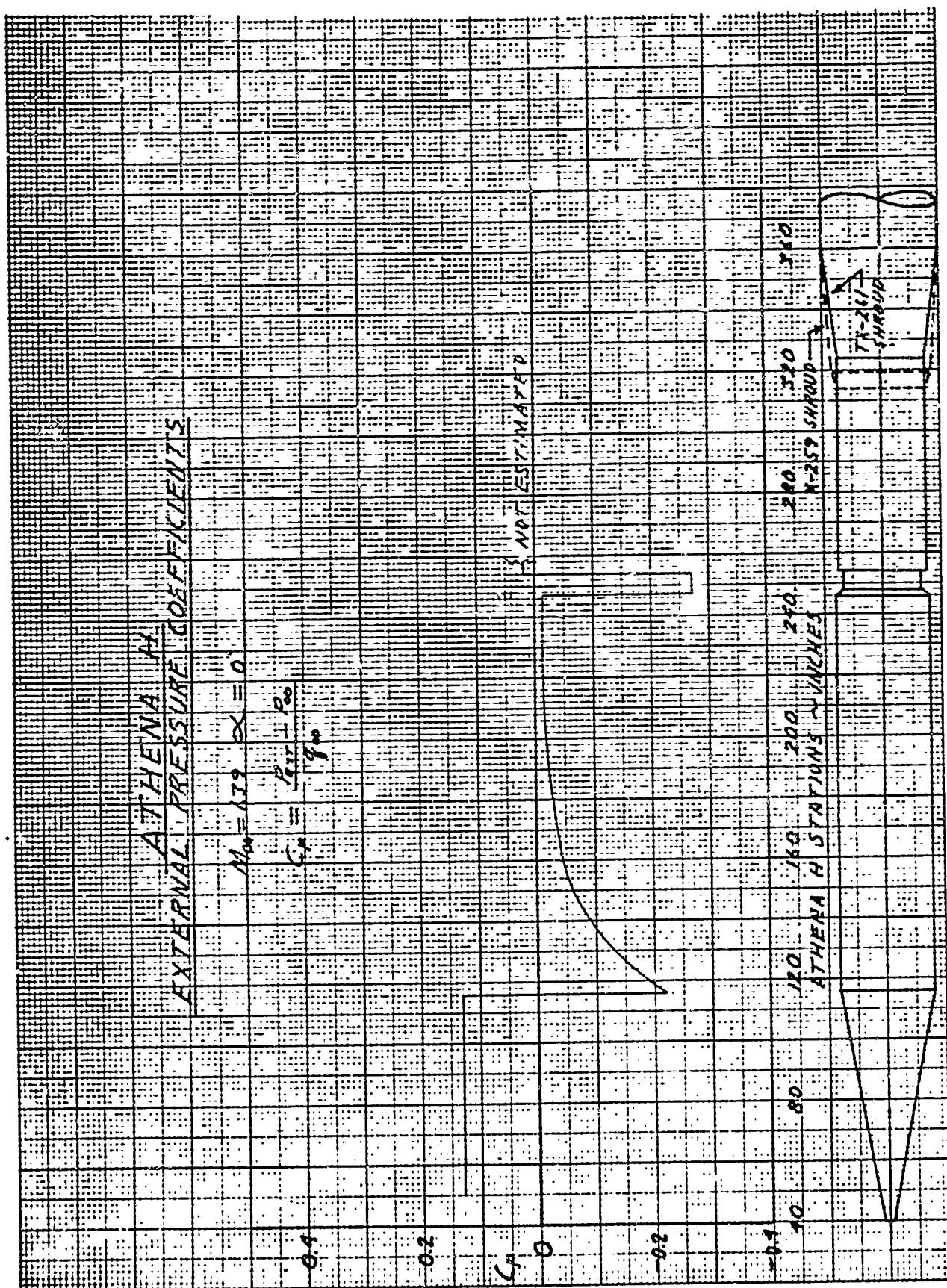


Figure 5-7. External Pressure Coefficient Distribution, $M_\infty = 1.39 \alpha = 0$

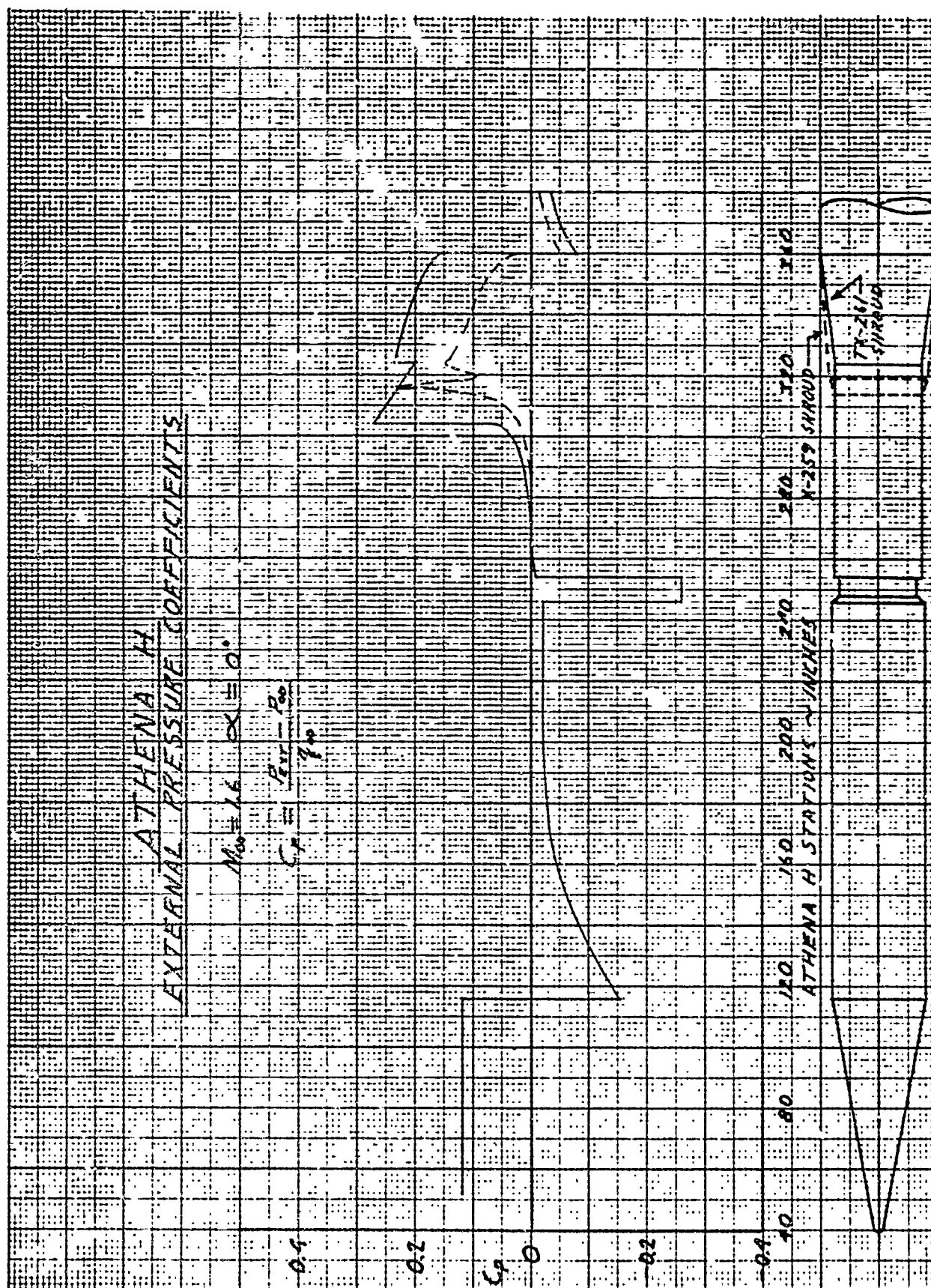


Figure 5-8. External Pressure Coefficient Distribution, $M_{\infty} = 1.6$ $\alpha = 0$

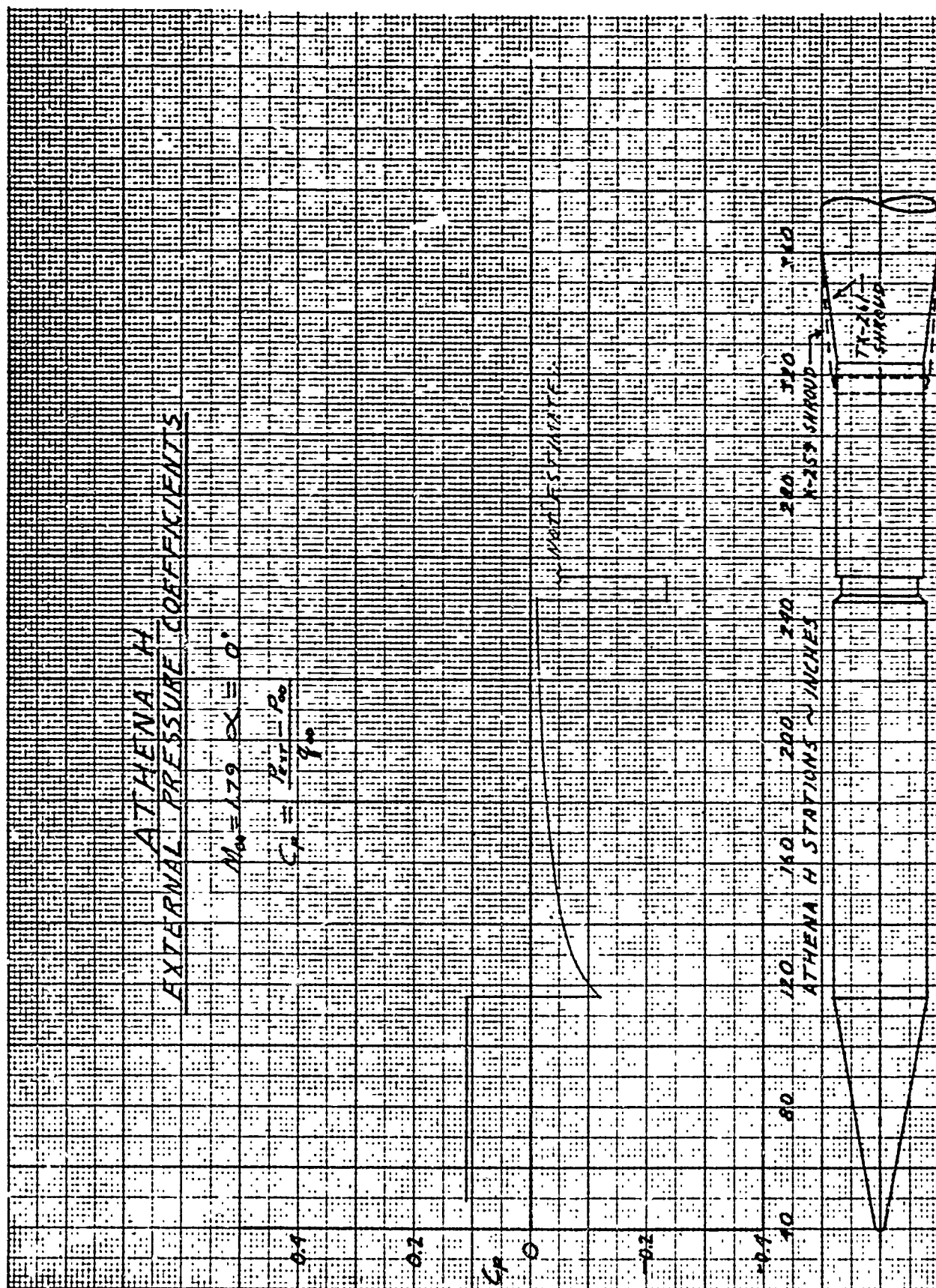


Figure 5-9. External Pressure Coefficient Distribution, $M_\infty = 1.79 \alpha = 0$

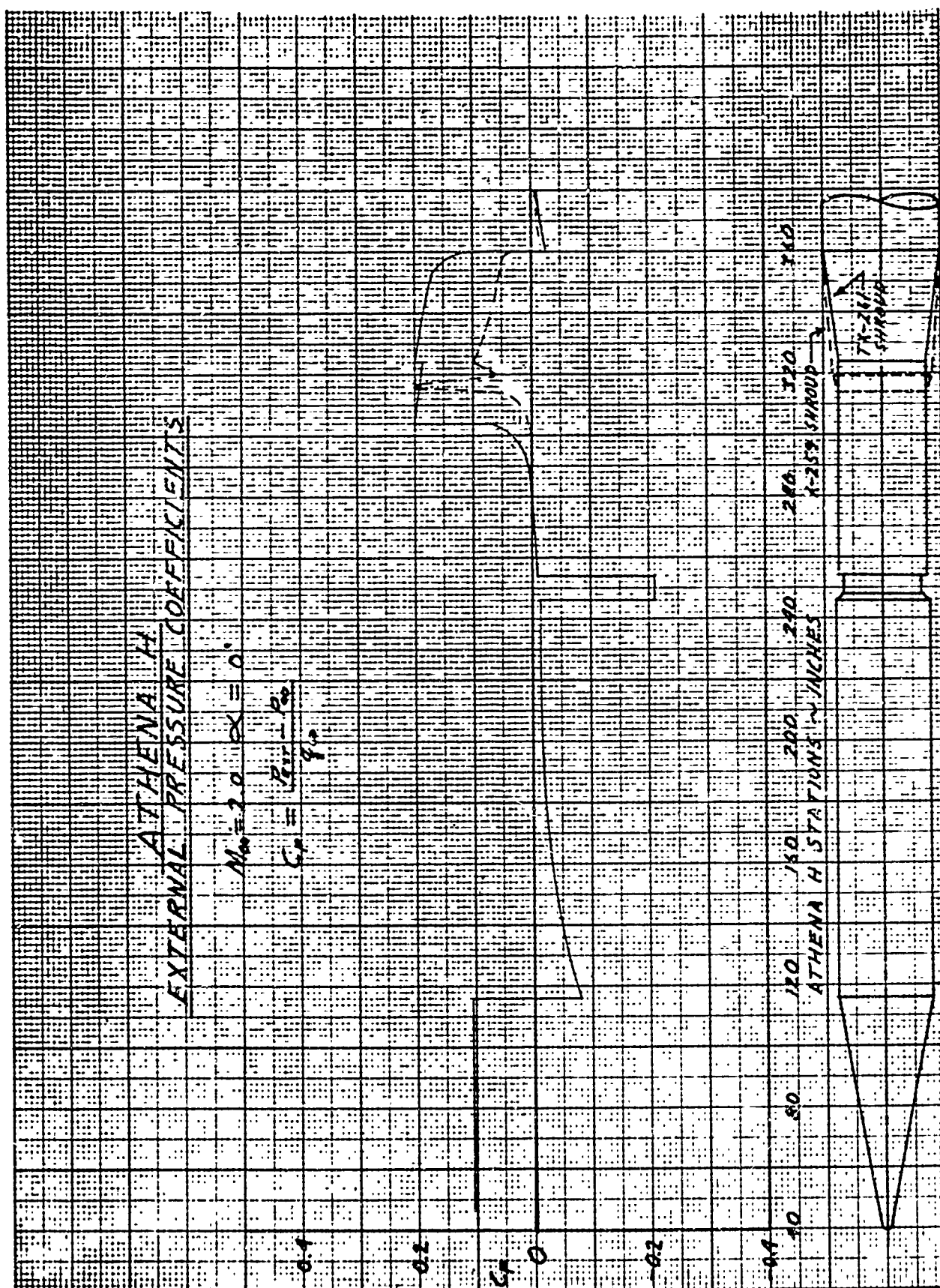


Figure 5-10. External Pressure Coefficient Distribution, $M_\infty = 2.0 \quad \alpha = 0$

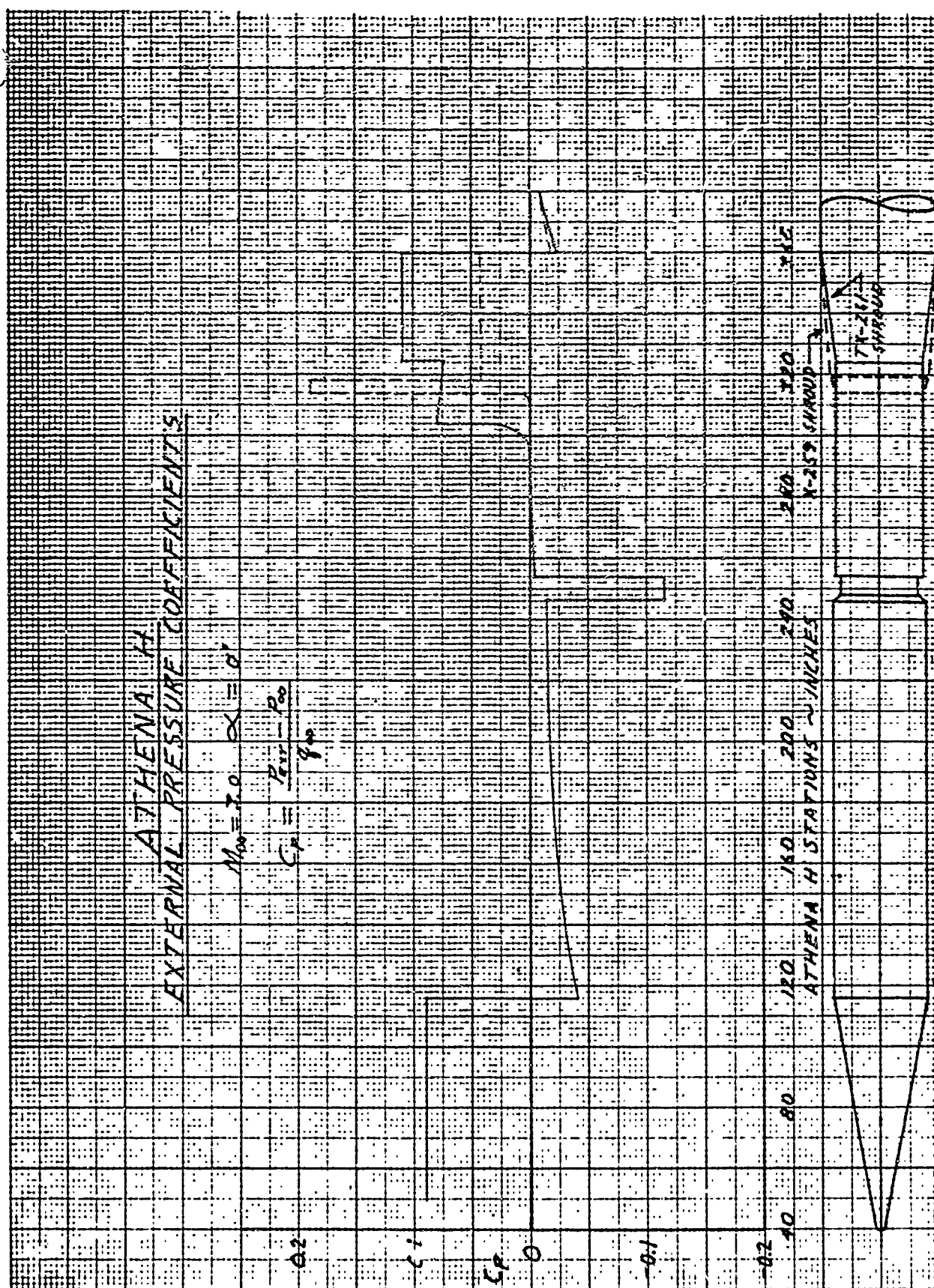


Figure 5-11. External Pressure Coefficient Distribution, $M_\infty = 3.0 \quad \alpha = 0^\circ$

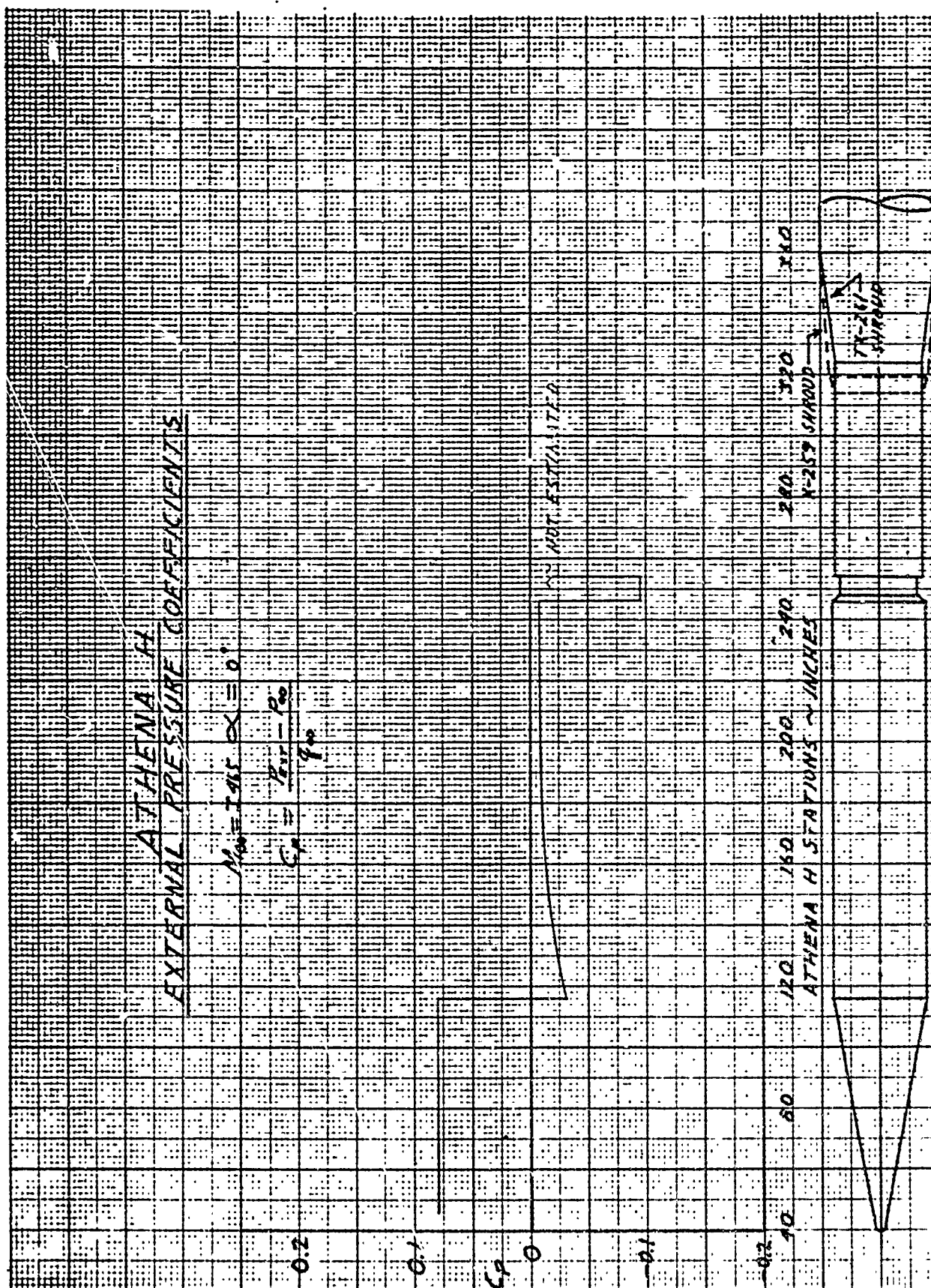


Figure 5-12. External Pressure Coefficient Distribution, $M_{\infty} = 3.465 \alpha = 0$

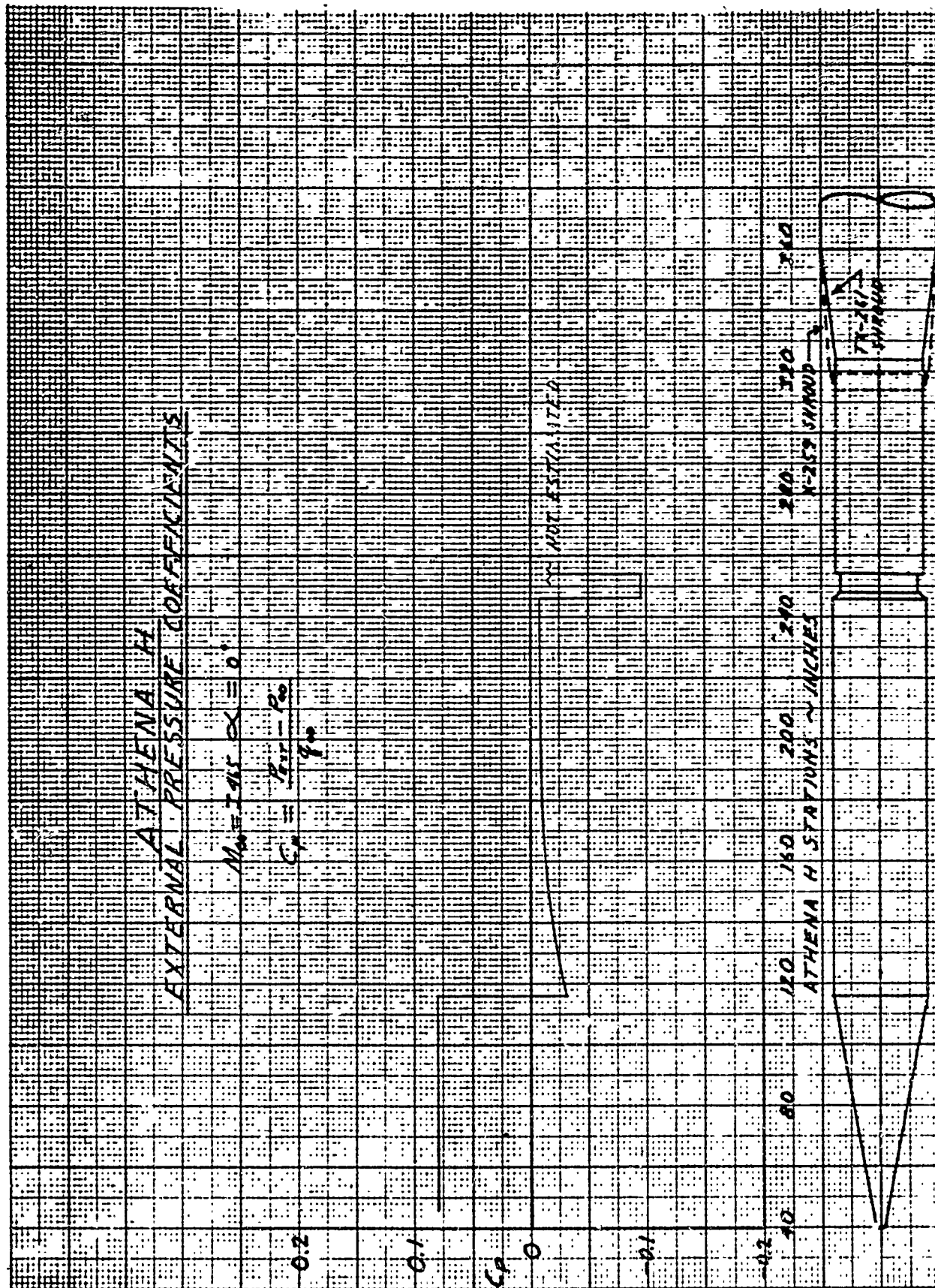


Figure 5-12. External Pressure Coefficient Distribution, $M_\infty = 3.465 \alpha = 0$

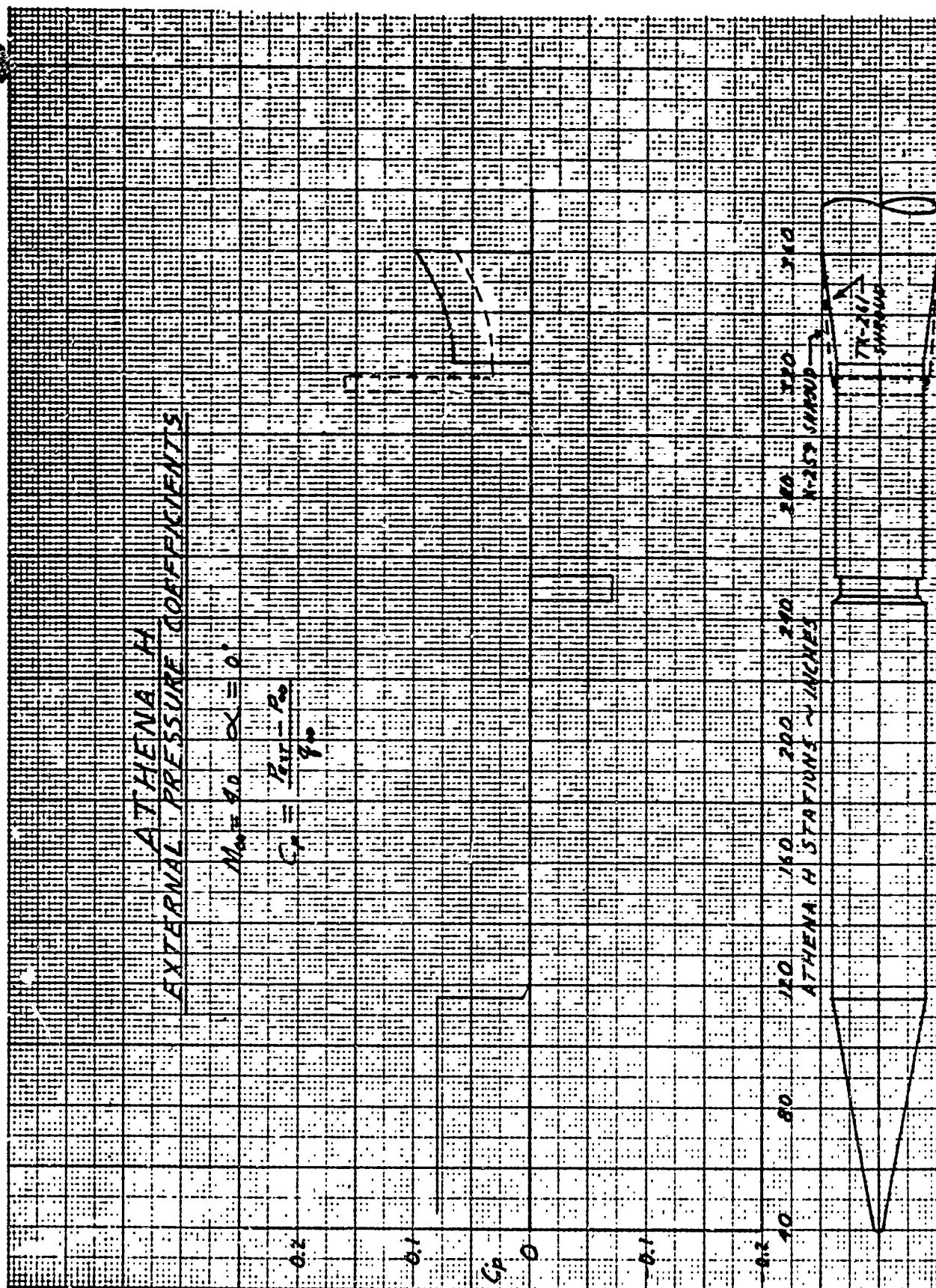


Figure 5-13. External Pressure Coefficient Distribution, $M_\infty = 4.0 \alpha = 0$

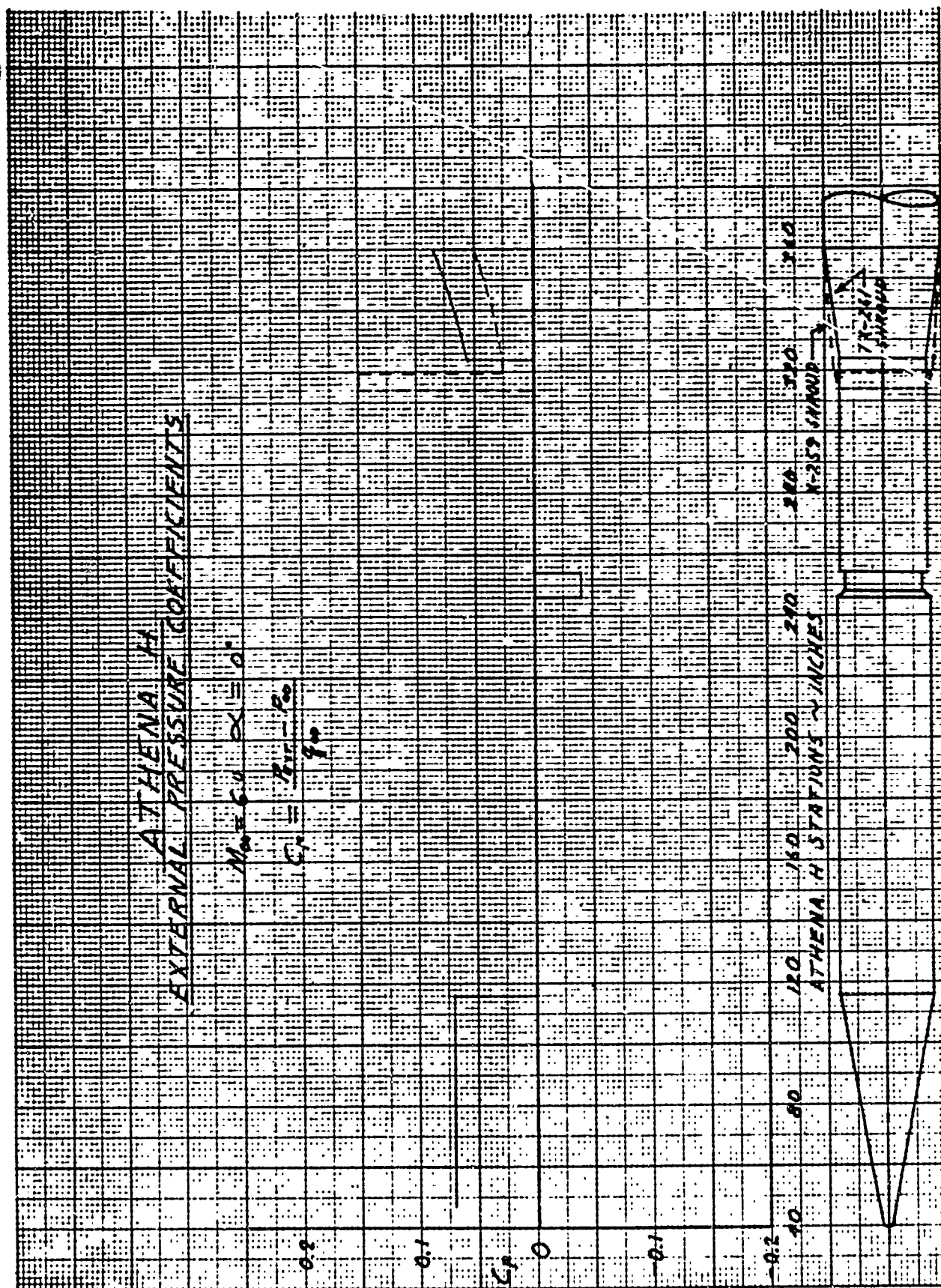


Figure 5-14. External Pressure Coefficient Distribution, $M_{\alpha} = 6.0 \alpha = 0.0$

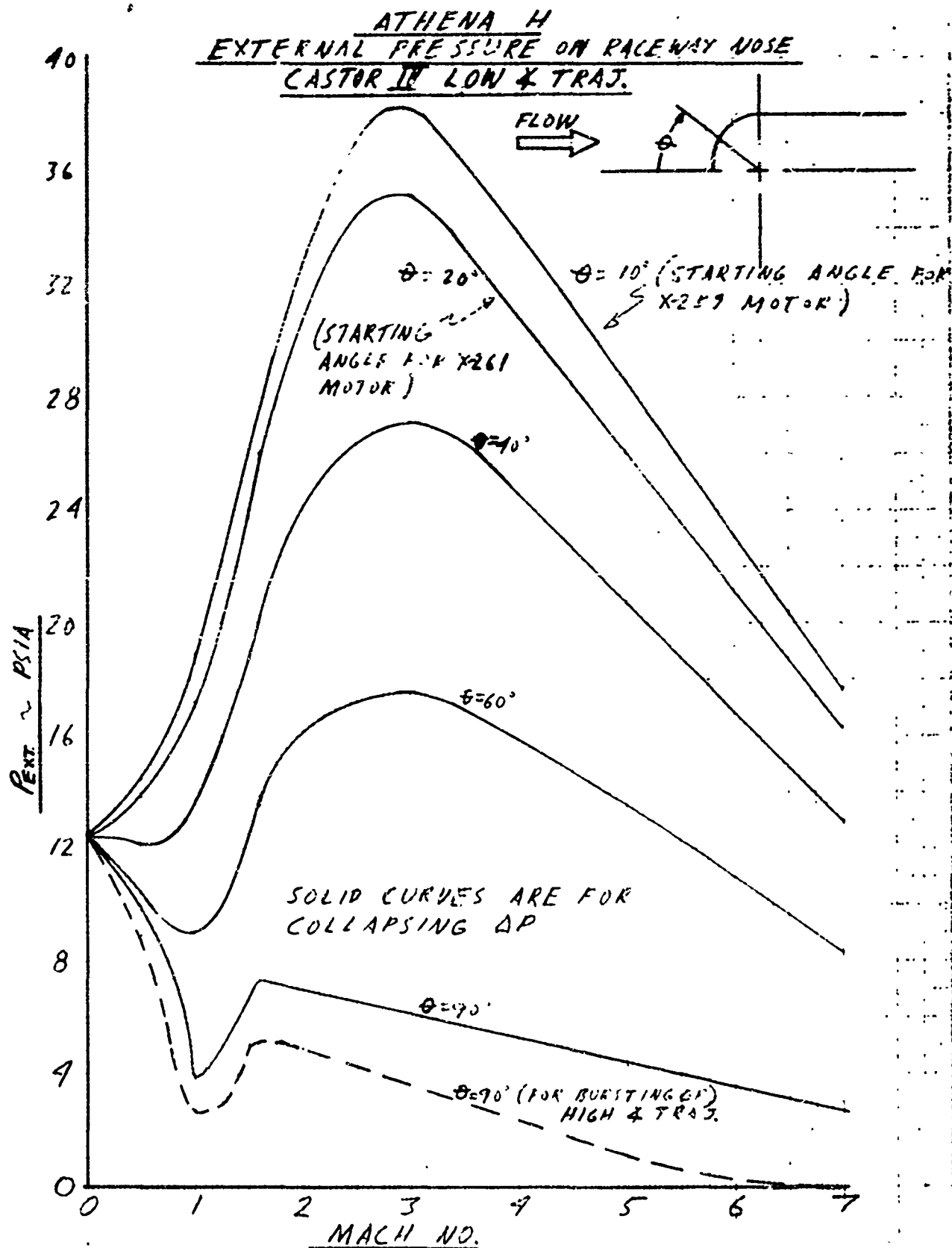


Figure 5-15. External Pressure on Raceway Nose Castor IV Low & Trajectories

ATHENA H
EXTERNAL PRESSURE ON RACEWAY MID-SECTION
CASTOR IV

NOTE. APPLY TO:

STA 259 - STA 259 FOR 259 MOTOR;

STA 261 - STA 261 FOR 261 MOTOR

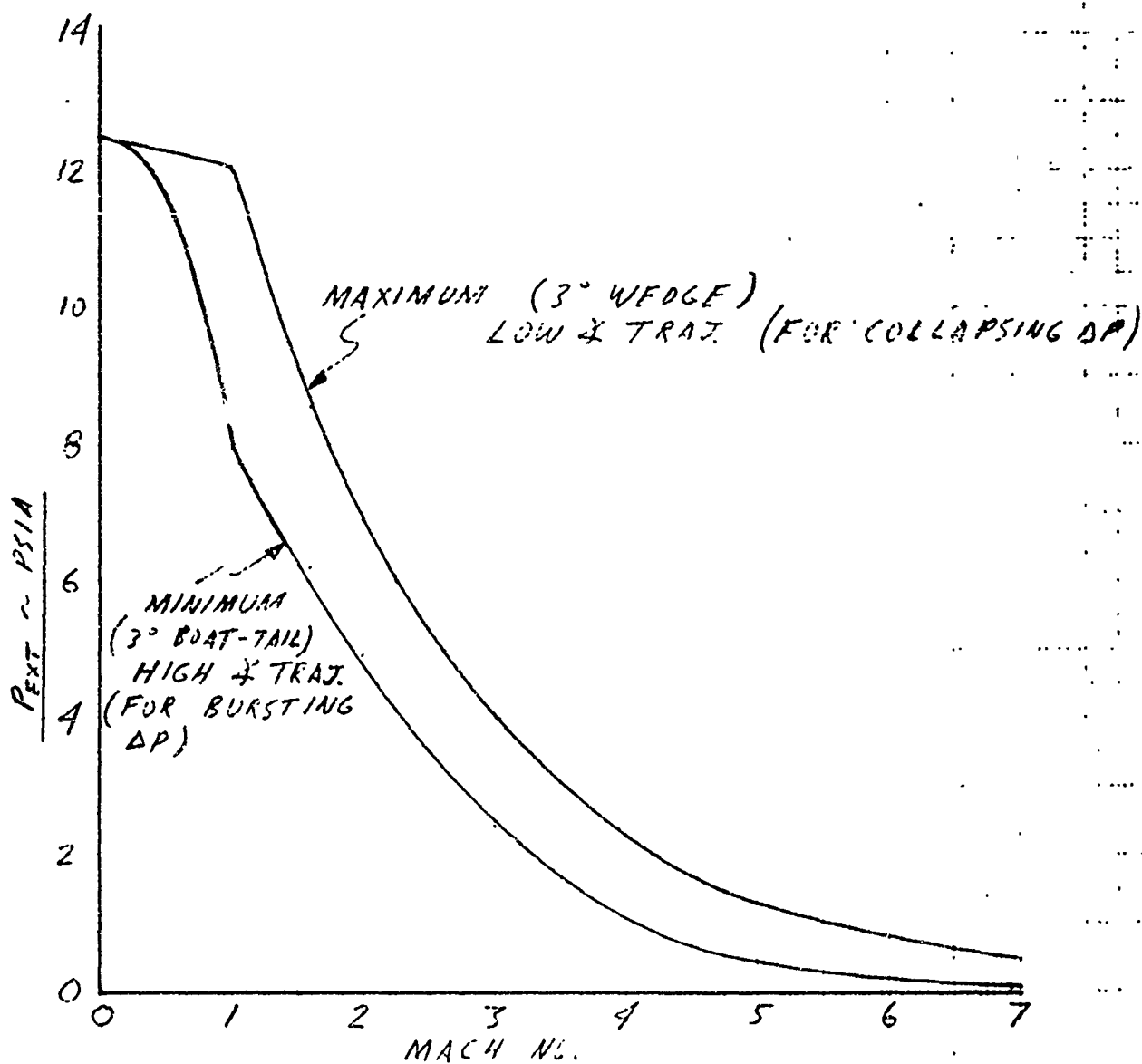


Figure 5-16. External Pressure on Raceway Mid-Section Castor IV

ATHENA H
EXTERNAL PRESSURE ON LAST SIX INCHES
OF RACEWAY IN SEPARATED REGION AHEAD
OF 2ND STAGE SHROUD
CASTOR IV LOW & TRAJ.

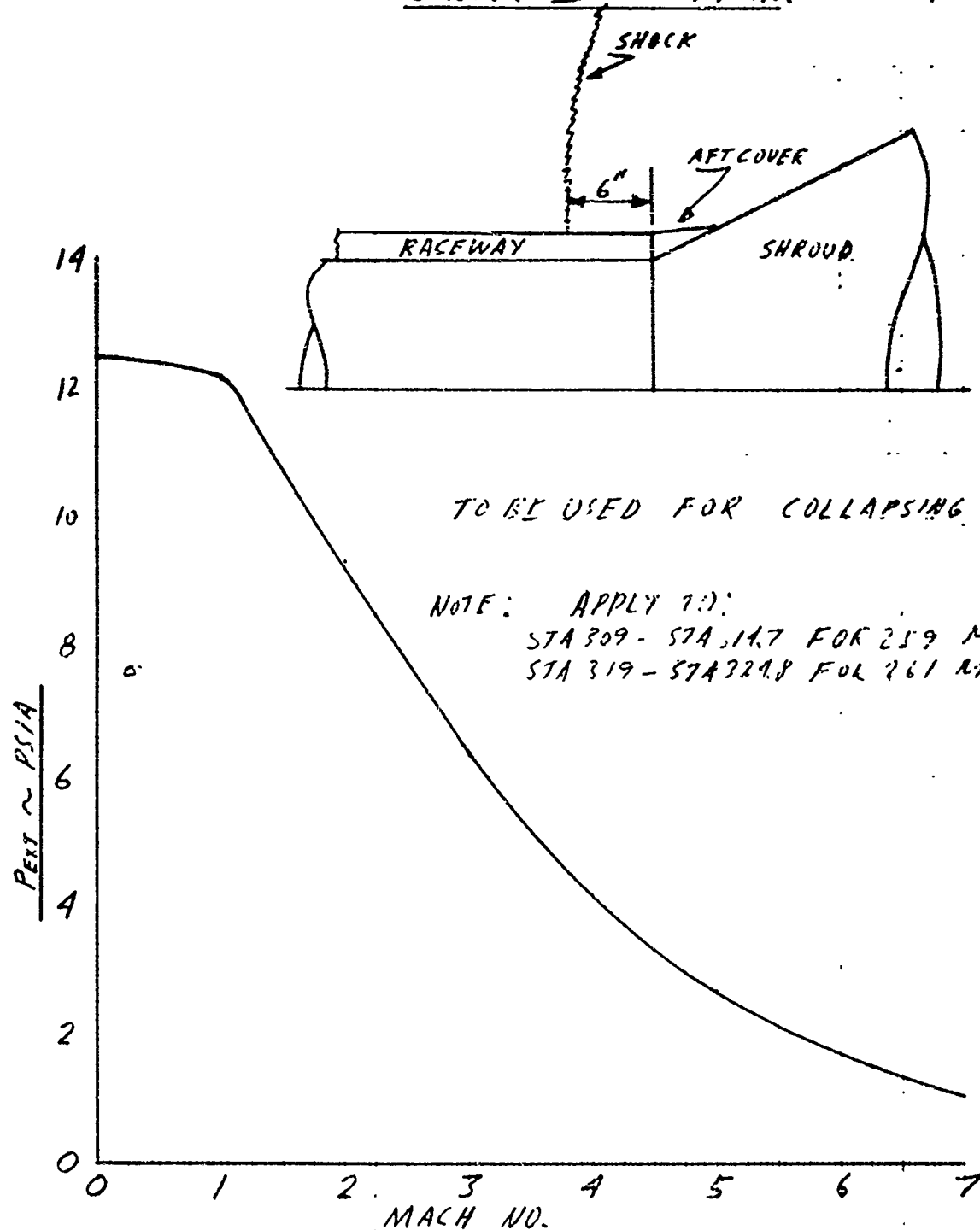


Figure 5-17. External Pressure on Last Six Inches of Raceway in Separated Region Ahead of 2nd Stage Shroud, Castor IV, Low & Trajectory

ATHENA H
EXTERNAL PRESSURE ON
RECRUIT NOSE
CASTOR IV

LOW α TRAJ

NOTE: FOR BURSTING, $P_{EXT} = 0$ FOR $M \geq 1.0$

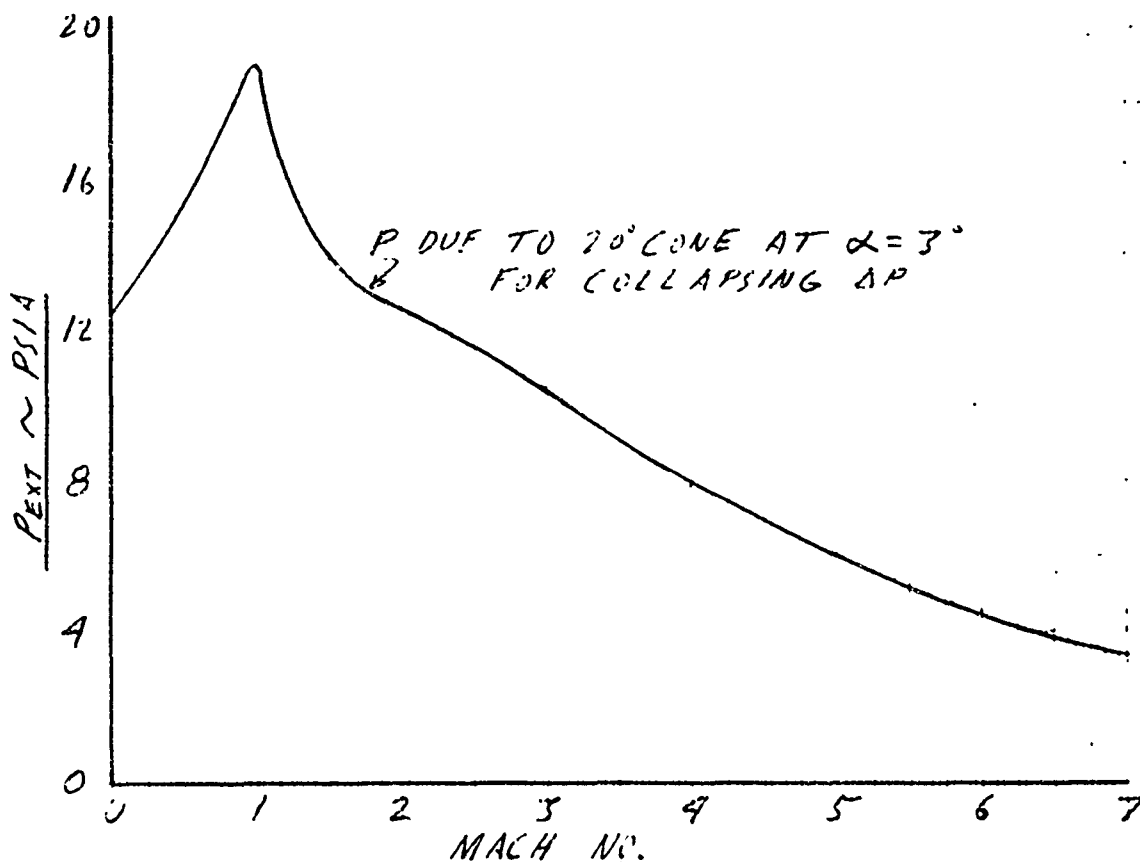


Figure 5-18. External Pressure on Recruit Nose, Castor IV

ATHENA H
EXTERNAL PRESSURE ON RECT. FAIRING
CIRCULAR SEGMENT
CASTOR IV

LOW α TRAJ.

TO BE USED FOR COLLAPSING ΔP .

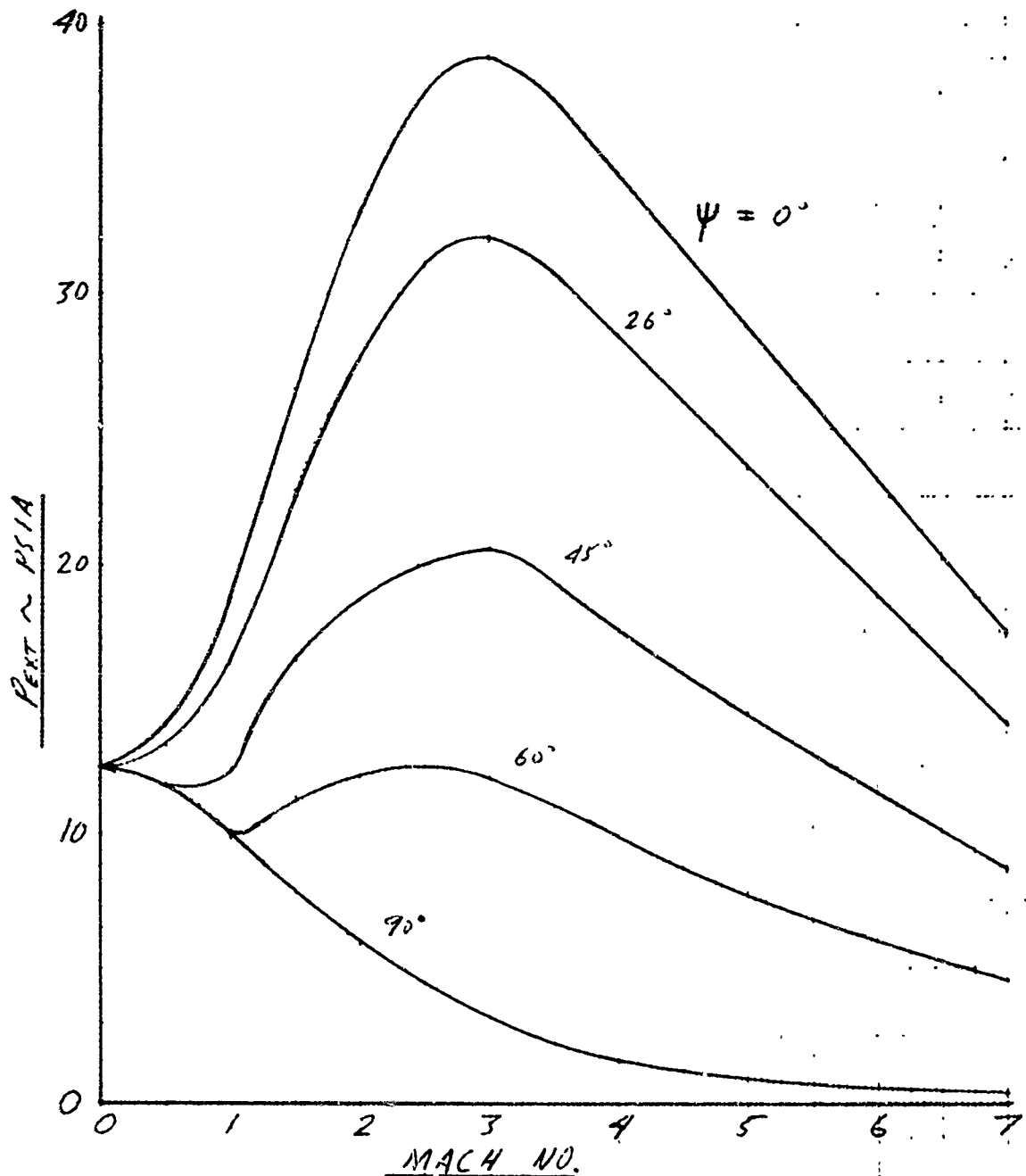


Figure 5-19. External Pressure on Recruit Fairing Circular Segment, Castor IV

ATHENA H
EXTERNAL PRESSURE ON AFT FAIRING
EXCLUDING CIRCULAR SEGMENT
CASTOR IV

LOW & TRAJ.

TO BE USED FOR COLLAPSING ΔP

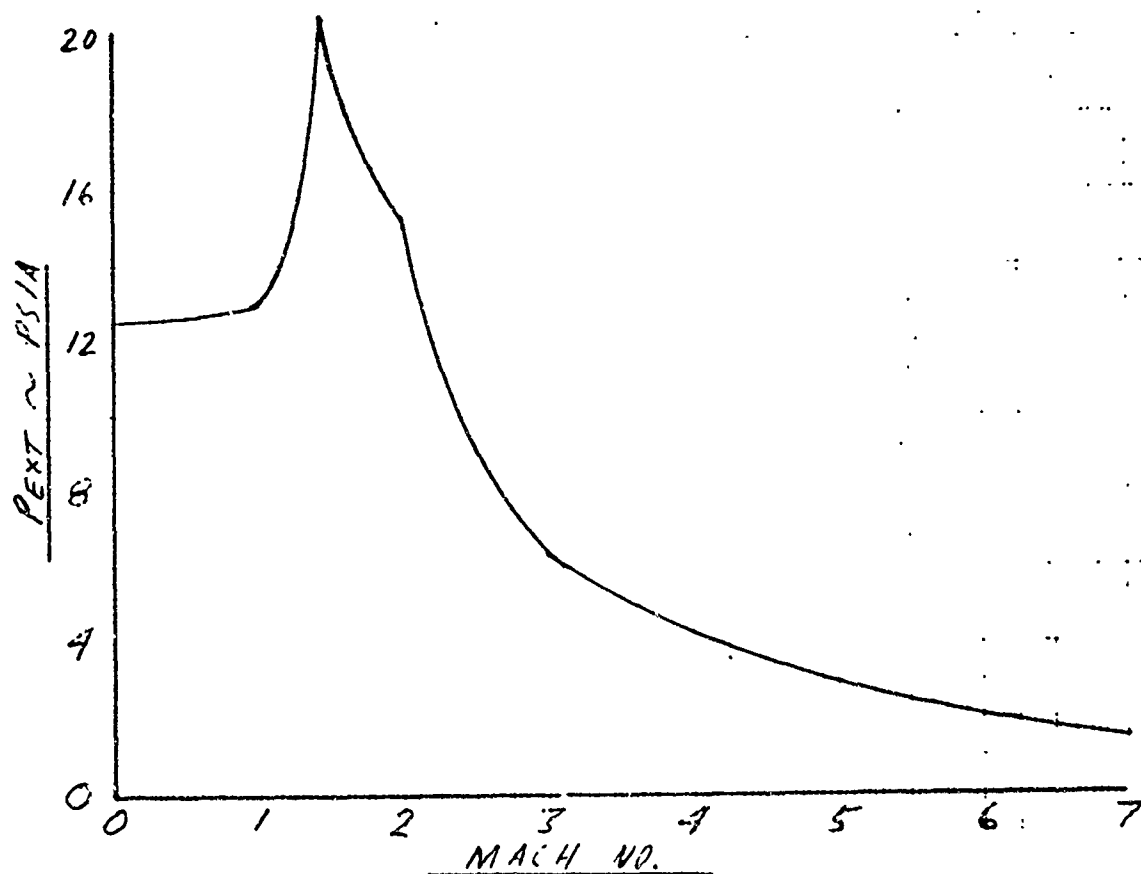


Figure 5-20. External Pressure on Aft Fairing Excluding Circular Segment, Castor IV

ATHENA H
EXTERNAL PRESSURE ON PYLONS
AND 1ST STAGE SHROUD

CASTOR IV LOW & TRAJ.

TO BE USED FOR COLLAPSING AP

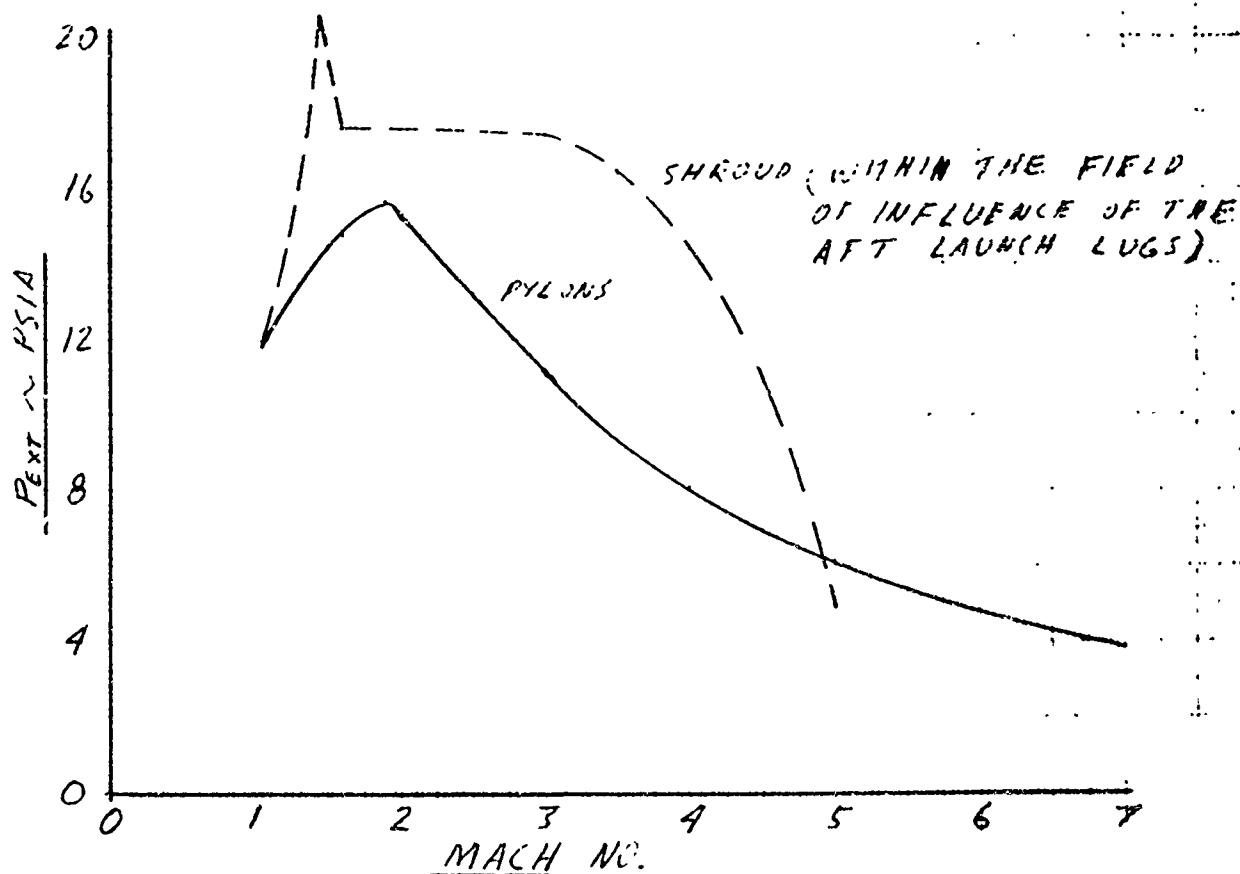


Figure 5-21. External Pressure on Payloads and 1st Stage Shroud, Castor IV

ATHENA H
EXTERNAL PRESSURE ON 1ST STAGE SHROUD

CASTOR IV
LOW & TRAX

NOTE: THIS P_{EXT} APPLIES TO THE AREA ON SHROUD BEHIND THE LAUNCH LUG PRESSURE FIELD AND IS BASED ON MAX. PRESSURE MEASUREMENTS WITH LAUNCH LUGS OR PAYLOAD FOD ON, WHICHEVER WAS HIGHER.

TO BE USED FOR COLLAPSING ΔP

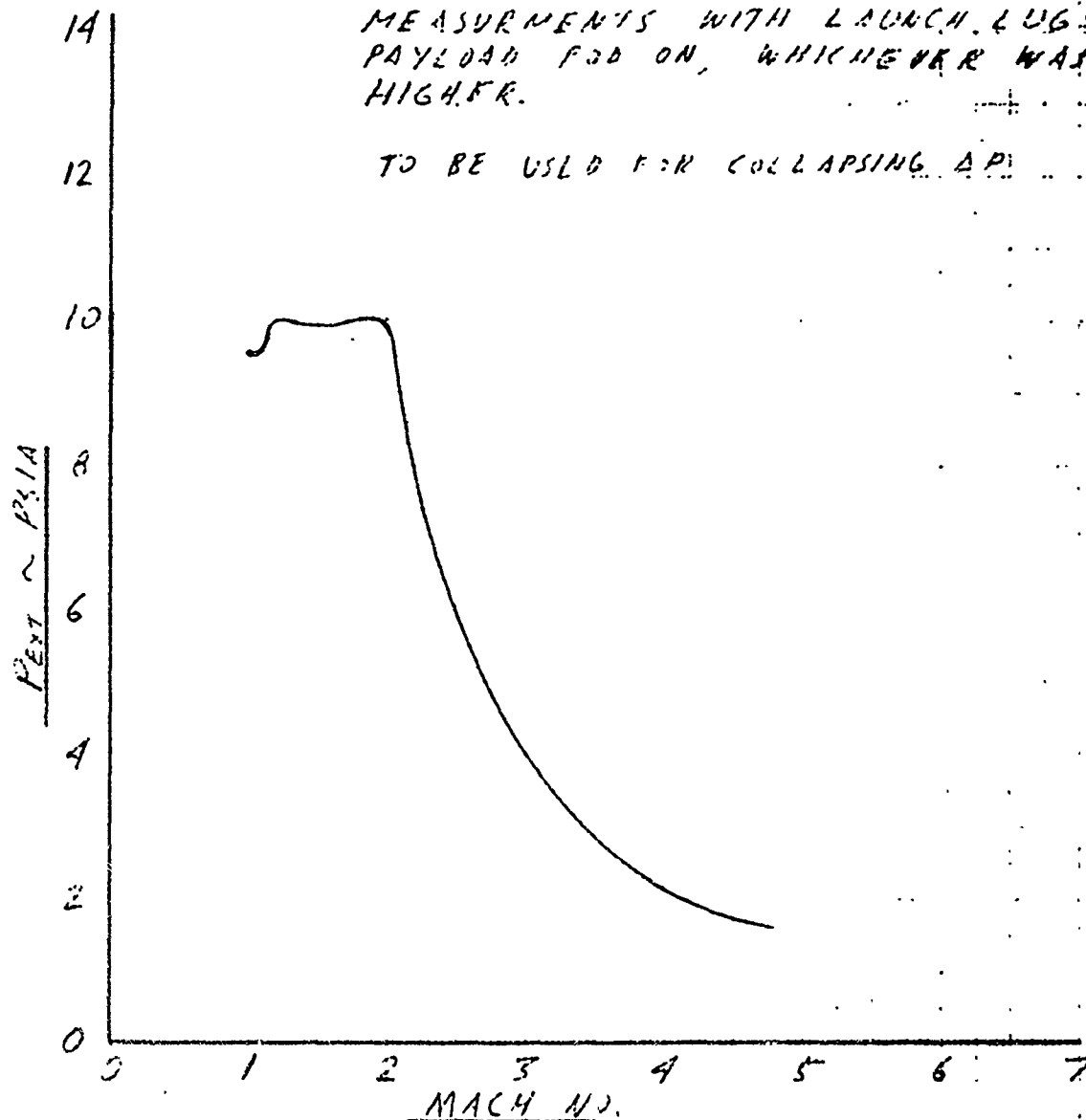


Figure 5-22. External Pressure on 1st Stage Shroud, Castor IV

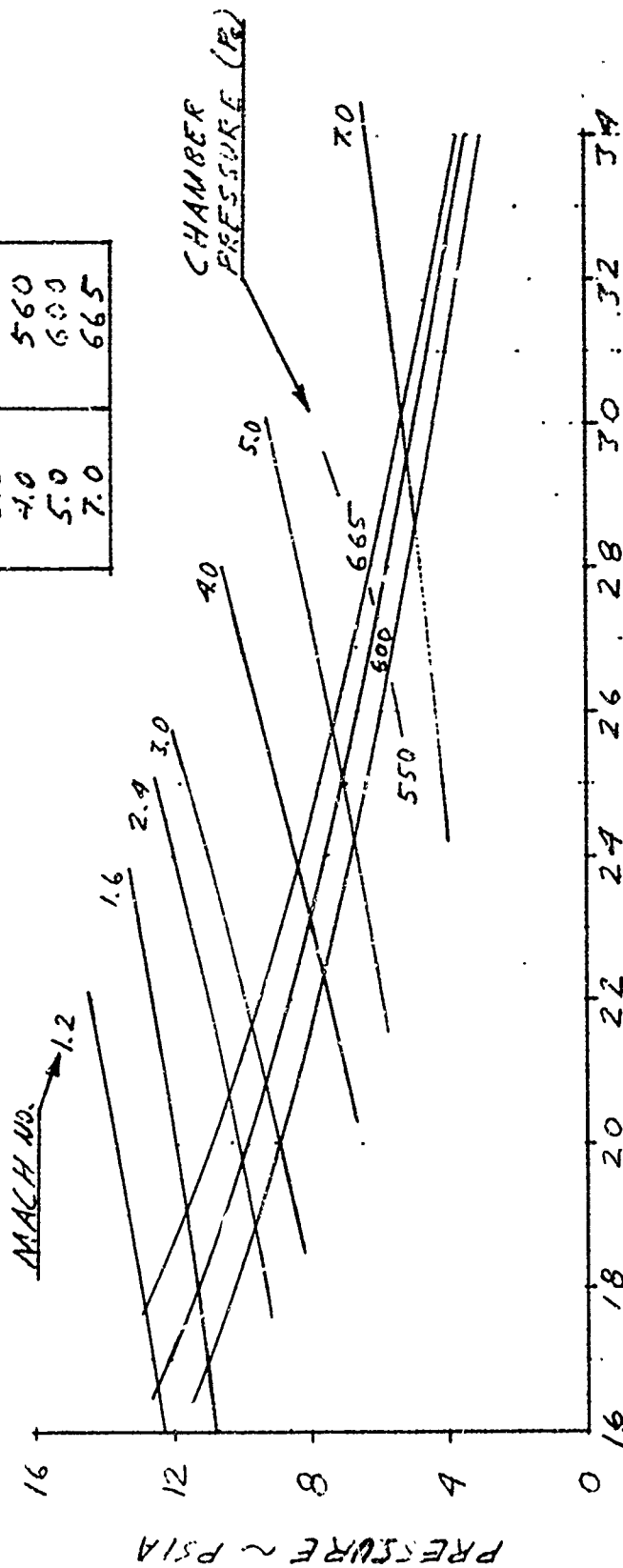
ATHENA H

PLUME BOUNDARY - FREE STREAM INTERACTION PRESSURE
AS A FUNCTION OF INITIAL TURNING ANGLE

CASTOR IV

MACH	Pc
1.2	610
1.6	590
2.4	570
3.0	560
4.0	560
5.0	600
7.0	665

TO BE USED FOR COLLATING CP



Θ , INITIAL TURNING ANGLE ~ DEGREES

Figure 5-23. Plume Boundary - Free Stream Interaction Pressure as a Function of Initial Turning Angle, Castor IV

ATHENA H
EXTERNAL PRESSURE ON PYLONS
AFT RCT FAIRING AND SHROUD

CASTOR IV
LOW α TRAJ.

BASED ON THEORETICAL 2-D BASE
PRESSURE COEFFICIENTS REDUCED BY
25%

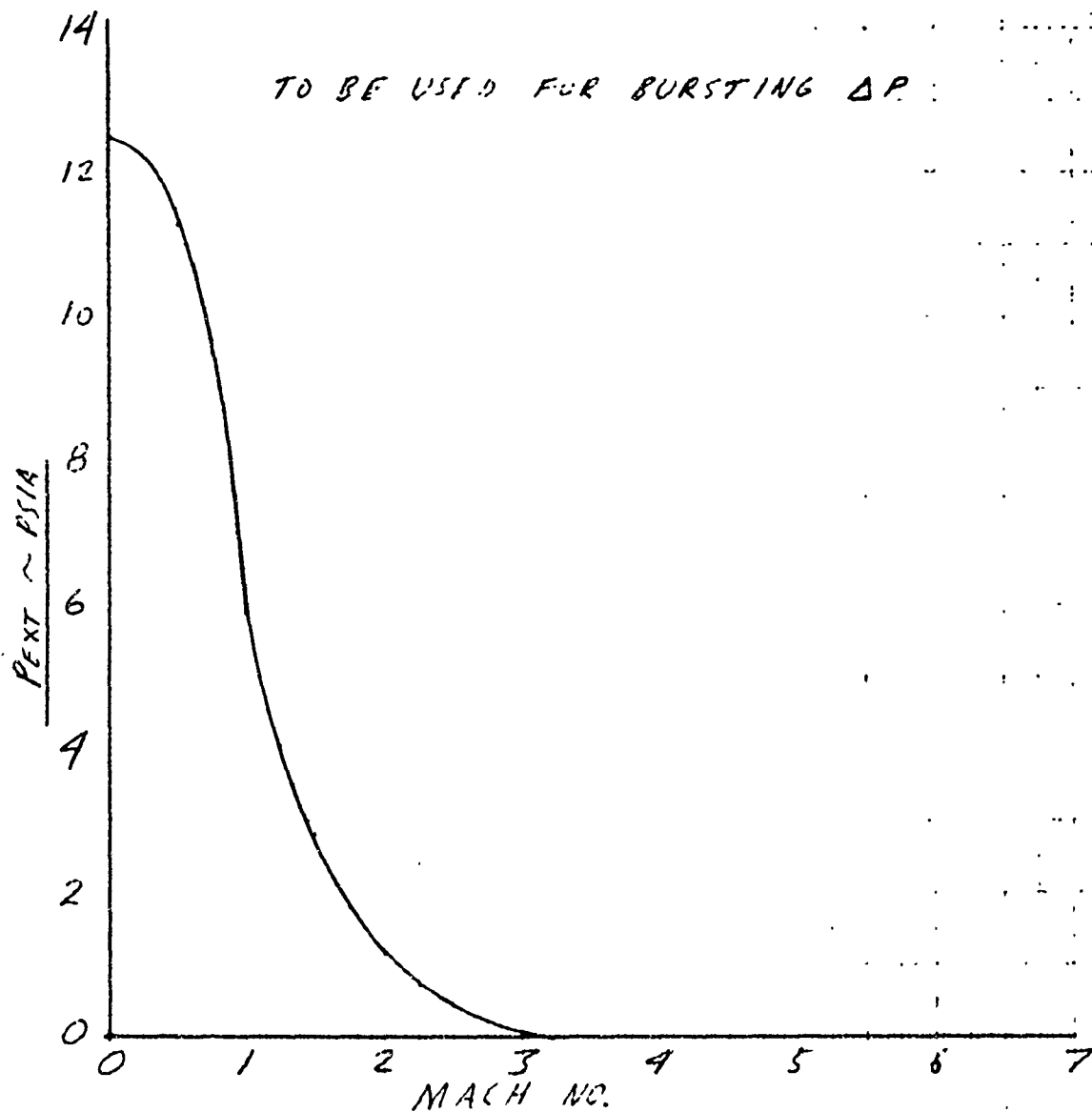


Figure 5-24. External Pressure on Pylons, Aft Recruit Fairing and Shroud

ATHENA H
FIN LEADING EDGE EXTERNAL
PRESSURE

CASTOR IV
LOW & TRAJ.

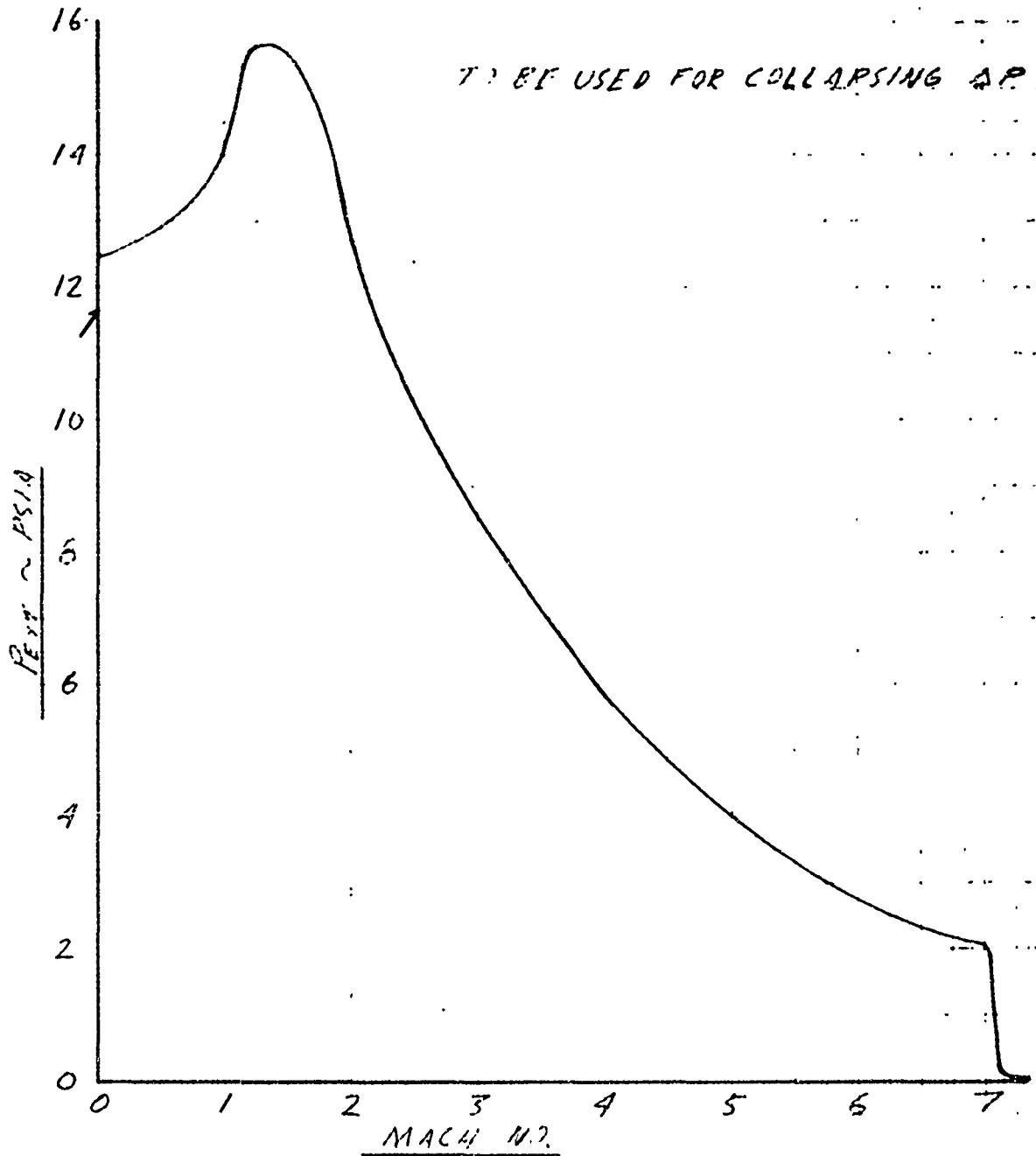


Figure 5-25. Fin Leading Edge External Pressure, Castor IV

ATHENA H
FIN SIDE PANEL EXTERNAL PRESSURE
AUXILIARY PAYLOAD POD ON

CASTOR IV
 LOW & TRAJ

NOTE: PRESSURES BASED ON MAXIMUM PWT
 PRESSURE DATA AND REPRESENTS
 PRESENCE OF 20° WEDGE BOX POD

TO BE USED FOR COLLAPSING AP

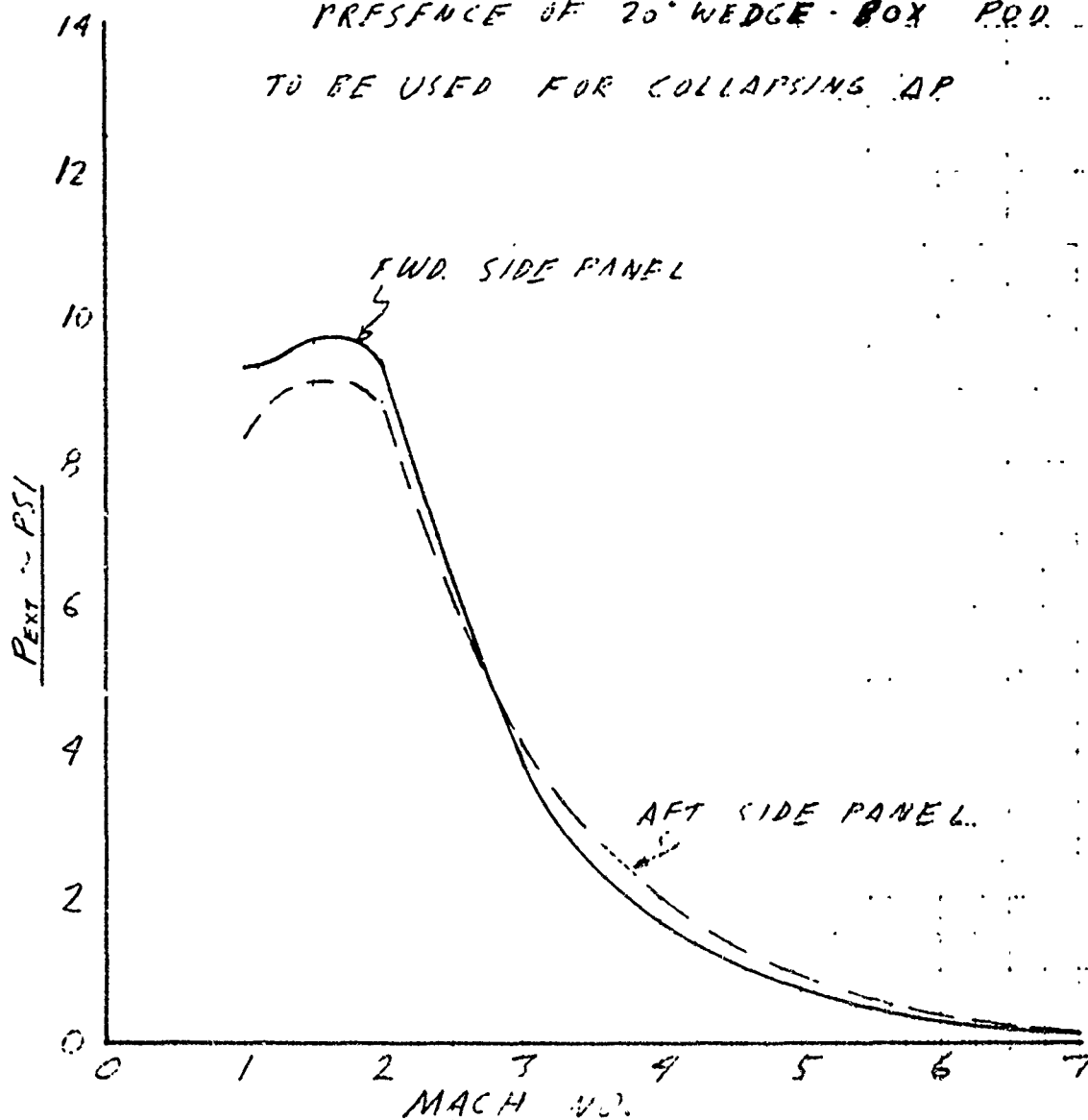


Figure 5-26. Fin Side Panel External Pressure, Auxiliary Payload Pod On, Castor IV

ATHENA H
FIN SIDE PANEL EXTERNAL PRESSURE
LAUNCH LUGS ON

CASTOR IV
LOW & TRAJ.

NOTE: PRESSURE BASED ON MAXIMUM PWT
PRESSURE DATA FOR POD-OFF,
LAUNCH LUGS - ON CASE.

TO BE USED FOR COLLAPSING AP

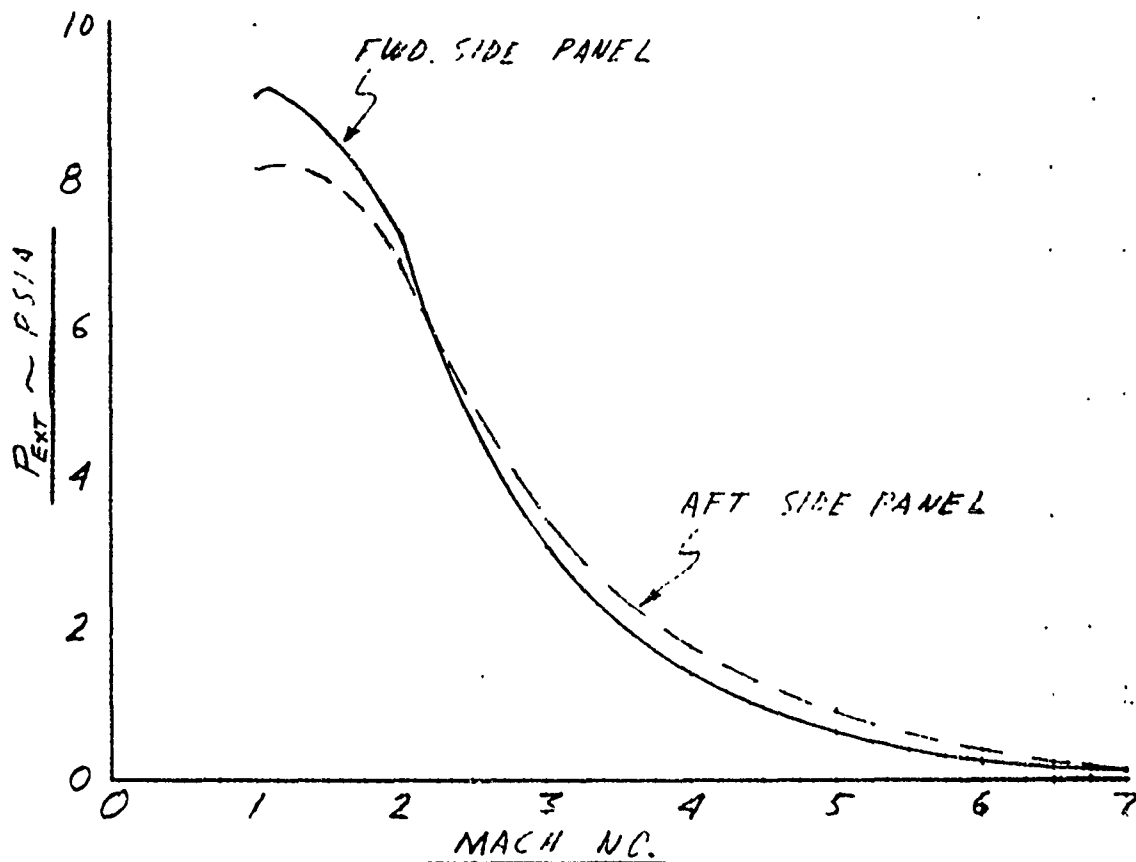


Figure 5-27. Fin Side Panel External Pressure, Launch Lugs On, Castor IV

TABLE 5-1. Castor IV Trajectories (T.D. 115)

	Low Angle Case 4077 Standard Stage		High Angle Case 4155 Alternate 3-Stage	
Time Seconds	Altitude Feet	Mach No.	Altitude Feet	Mach No.
0.0	4504.0	0.000	4504.0	0.000
2.1	4950.0	0.366	4978.0	0.365
4.3	5888.0	0.513	5984.0	0.509
7.0	7424.0	0.708	7663.0	0.700
11.0	10464.0	1.010	11073.0	0.993
15.0	14330.0	1.327	15543.0	1.304
19.0	18986.0	1.683	21097.0	1.659
23.0	24435.0	2.087	27805.0	2.072
27.0	30694.0	2.557	35764.0	2.570
29.0	34143.0	2.825	40255.0	2.809
31.0	37814.0	3.096	45118.0	3.061
35.0	45879.0	3.642	46062.0	3.622
39.0	55031.0	4.297	68859.0	4.296
45.0	71411.0	5.619	92533.0	5.530
53.0	100331.0	7.793	135856.0	7.365
56.7	116410.0	7.982	160444.0	7.522
66.7	158412.0	7.305	225813.0	8.370
80.0	209722.0	7.787	308089.0	
95.0	261743.0	9.018	395092.0	
115.0	305000.0		475000.0	

VI

CONCLUSIONS

The aerodynamic characteristics presented in this document are the result of analyses and numerous wind tunnel test and should be used for trajectory, stability and structural analysis. The aerodynamic load distributions are in general based upon and reflect the total vehicle aerodynamic characteristics. The external pressure distributions over the vehicle components were based on conservative predictions and full scale wind tunnel data.

The total vehicle aerodynamic characteristics can be used to accurately predict and simulate the vehicle flight qualities. The distributed aerodynamic loads can be used for realistic structural evaluation and the external vehicle and component pressures will yield conservative venting analysis results.

VII

REFERENCES

1. Petak, G. M., Benton, R. L., McClymonds, J. W., ATHENA H Wind Tunnel Test , Volumes I and II, AR/MSD Document Number 01-TR-001, December 1968.
2. Baipsys, V. J., ATHENA H Wind Tunnel Test Document, Volume III, AR/MSD Document Number 01-TR-001, January 1970
3. Cochran, Vertis C., D'Arcy, Edward M., Ramirez, Florencio, Digital Computer Program For Five-Degree-Of-Freedom Trajectory, Atmospheric Sciences Laboratory, ECOM-5036, March 1966.
4. Hoerner, S. F., Fluid-Dynamic Drag, 1958.
5. Baipsys, V. J., ATHENA H Venting Analysis, AR/MSD Document Number 01-TR-005, December 1969.

UNCLASSIFIED

Security Classification

DOCUMENT CONTROL DATA - R & D

(Security classification of title, body of abstract and indexing annotation must be entered when the overall report is classified)

1. ORIGINATING ACTIVITY (Corporate author) Atlantic Research Corporation Missile Systems Division Costa Mesa, California		2a. REPORT SECURITY CLASSIFICATION Unclassified	
		2b. GROUP None	
3. REPORT TITLE ATHENA H Aerodynamic Data Summary			
4. DESCRIPTIVE NOTES (Type of report and inclusive dates) Final December 1967 through August 1969			
5. AUTHOR(S) (First name, middle initial, last name) Vyto J. Balpsys, Richard L. Benton, Raymond J. Hauser John W. McClymonds, Gerald M. Petak			
6. REPORT DATE December 1969		7a. TOTAL NO. OF PAGES 94	7b. NO. OF REFS 3
8a. CONTRACT OR GRANT NO. F04701-68-C-0046		8a. ORIGINATOR'S REPORT NUMBER(S) 01-EN-004	
b. PROJECT NO. 627/A		9b. OTHER REPORT NO(S) (Any other numbers that may be assigned this report) None	
10. DISTRIBUTION STATEMENT This document may be further distributed by any holder only with specific prior approval of SAMSO.			
11. SUPPLEMENTARY NOTES None		12. SPONSORING MILITARY ACTIVITY Space and Missile Systems Organization Air Force Systems Command Norton Air Force Base, California	
13. ABSTRACT <p>This document presents aerodynamic characteristics for the ATHENA H reentry research vehicle. Data presented herein include longitudinal, lateral and directional stability characteristics and normal, side, and axial force characteristics as a function of Mach number, for the complete vehicle and expended stages. Also presented herein are aerodynamic loads on the vehicle appendage and external pressures on the major and minor vehicle components. This information is presented in tabular and graphical form throughout the range of vehicle flight attitude and trajectories to be experienced by ATHENA H.</p>			

DD FORM 1 NOV 65 1473

UNCLASSIFIED

Security Classification